Technische Universität München
Fakultät für Physik

Master's Thesis in Nuclear, Particle and Astrophysics

Characterisation of a 166-Pixel TRISTAN Detector Module in the KATRIN Monitor Spectrometer

Charakterisierung eines 166-Pixel TRISTAN Detektormoduls im KATRIN Monitorspektrometer

Christina Bruch

01. März 2023

Contents

List of Figures

List of Tables

Abstract

Sterile neutrinos are a minimal extension of the Standard Model of Particle Physics, which could provide answers to a multitude of open questions in neutrino physics and cosmology. Sterile neutrinos with a mass in the keV range are possible Dark Matter candidates. Due to their right-handed nature, they would interact only via a small mixing to active neutrinos. Nevertheless, due to their additional heavy mass eigenstate, they would leave a kink-like imprint in the beta-decay spectra of isotopes like tritium.

The KATRIN experiment uses a strong and stable tritium source to investigate the effective electron antineutrino mass. After the neutrino mass measurement campaigns, the KATRIN experiment aims to search for keV-scale sterile neutrinos. In contrast to the neutrino mass, which manifests itself in the endpoint region of the tritium spectrum, the kink-like signature of a sterile neutrino can be anywhere in the tritium spectrum. Therefore, the search for sterile neutrinos with KATRIN requires a new detector and readout system, which are capable of handling high count rates while providing an excellent energy resolution of less than $300\,\mathrm{eV}$ at electron energies of $20\,\mathrm{keV}$. Additionally, a precise calibration and modeling of the detector response is crucial. For this task, the TRISTAN detector and readout system is currently under development. The segmented detector system will consist of nine and 21 166-pixel silicon drift detector modules for phase 1 and a possible phase 2, respectively.

In this thesis, one of the first 166-pixel TRISTAN detector modules was characterised for the first time in a KATRIN-like MAC-E filter environment at the KATRIN Monitor Spectrometer. In a first step, an optimisation of all relevant detector voltages was performed at a dedicated laboratory test stand at the Max-Planck-Institute for Physics in Munich. A working point was found, for which the energy resolution was improved by $9.3\,\%$ for $5.9\,\mathrm{keV}$ photons compared to measurements with non-optimised voltages.

In the next step, the 166-pixel TRISTAN detector module was successfully installed in the KATRIN Monitor Spectrometer along with a calibration tool and a specially designed calibration source holder. For the first commissioning, an $^{55}\mathrm{Fe}$ source was used and a median energy resolution of $\overline{\Delta E_\mathrm{FWHM}} = 151\,\mathrm{eV}$ for $5.9\,\mathrm{keV}$

photons was achieved.

After this initial test, the 166-pixel TRISTAN detector module was for the first time exposed to electrons in a realistic MAC-E filter environment. A median energy resolution of $\overline{\Delta E_{\mathrm{FWHM}}} = 285\,\mathrm{keV}$ was achieved for $20\,\mathrm{keV}$ electrons, that originate from the walls of the spectrometer. This result is in agreement with the expectation and meets the design goal of the TRISTAN detector.

Finally, the noise performance of the 166-pixel TRISTAN detector module was investigated. In the KATRIN Monitor Spectrometer, it was comparable to the one in a dedicated laboratory test stand at the MPP. It was shown that the 166-pixel detector module can be operated in a new, realistic environment, e.g. with a $1\,\mathrm{m}$ long cable between the pre-amplifier and the DAQ, with almost no performance loss for peaking times of $t_{\mathrm{peak}} \leq 1\,\mathrm{\mu s}$. Furthermore, the behaviour of the energy resolution for photons can be well explained by electronic noise and the Fano statistics. In contrast, in the case of electrons the energy resolution is limited by the entrance window thickness.

However, the measurements with electrons performed in the scope of this thesis also revealed an unexpected inhomogeneity of the pixel performances, i.e. one region of the detector showed a degraded energy resolution for electrons. The difference in energy resolution of the two regions can not be explained by additional noise components for the different regions. With the help of detailed tests and analyses it was demonstrated that the poor performance can be best explained by an additional nm-scale layer on the surface of the detector. This feature is currently under investigation.

Chapter 1

Introduction to Neutrino Physics

Since the postulation of the neutrino by Wolfgang Pauli in 1930 [1], this particle gives rise to numerous questions concerning its nature and properties. In the Standard Model of Particle Physics (SM), neutrinos take an unique role. Since they do not carry any charge at all, they only interact via the weak interaction, making them hard to detect. Additionally, they only come left-handed, setting them apart from their lepton counterparts that come both as right- and left-handed particles. Moreover, neutrinos are assumed to be massless in the SM. However, neutrino oscillations confirmed that neutrinos have a mass, albeit small. Their absolute mass as well as whether they are Dirac or Majorana particles, i.e. their own antiparticles, is still unknown and under investigation in a wide variety of experiments [2].

To understand the current scientific knowledge of these particles, a brief introduction in neutrino physics is given in this chapter. First, in section 1.1, the SM neutrino is explained, before giving an example of physics beyond the SM. In section 1.2, a brief introduction to a hypothetical non-SM particle, the sterile neutrino, is given. While these particles are in principle not limited to a certain mass range, keV-scale sterile neutrinos are especially interesting in the scope of this thesis, as they are suitable Dark Matter candidates.

1.1 Active Neutrino Physics

1.1.1 A Brief History of Active Neutrinos

Single beta-decay is one of the most fundamental processes in which neutrinos are produced:

$$^A_Z X \rightarrow ^A_{Z+1} Y + e^- + \bar{\nu}_e. \tag{1.1}$$

Here, a mother nucleus $^A_Z X$ with mass number A and proton number Z decays into the daughter nucleus $^A_{Z+1} Y$, an electron e^- and an electron antineutrino $\bar{\nu}_e$. Before the postulation of the neutrino, however, this reaction was only described by

$$X \rightarrow X' + e^-, \tag{1.2}$$

as the atomic model only consisted of electrons bound by the electromagnetic force to a nucleus consisting of protons. According to this simple two-body decay model, a monoenergetic spectrum was expected for the beta-decay electrons [2]. However, this model failed to explain the observed continuous electron energy spectrum.

Another challenge was the "false" statistics of the $^{14}_{7}\text{N}$ nucleus. Consisting of 7 protons and 7 electrons, nitrogen should have a spin of -1/2 but was proven to have integer spin by scattering experiments [2]. These challenges inspired Wolfgang Pauli in 1930 to propose a new particle, the "neutron", with spin-1/2 and a mass around the mass of the electron [1]. After the discovery of the neutron, Enrico Fermi proposed the name "neutrino" for Paulis new particle [2].

Despite the early postulation of the neutrino, it was discovered only 23 years later in 1956 by C. L. Cowan and F. Reines via the inverse beta-decay

$$\bar{\nu}_{\text{e}} + p \rightarrow e^{+} + n. \tag{1.3}$$

In the experiment at the Savannah River Plant, reactor antineutrinos hit a hydrogenous liquid scintillator, producing a positron e^{+} and a neutron n. The reaction products were detected using a delayed coincidence signal. The first photon is emitted when the positron annihilates with another electron, while the neutron is moderated and captured in cadmium, which is dissolved in the scintillator. After the neutron capture, cadmium is in an excited state and emits a second photon when it deexcites [3].

A couple of years later, the discovery of the muon neutrino in the Brookhaven Alternating Gradient Synchrotron (AGS) [4] and the tau neutrino in the Direct Observation of Nu Tau (DONUT) experiment [5] revealed that there are three neutrino flavours corresponding to the lepton flavours e, μ and τ. In addition, it was shown in the Goldhaber experiment that neutrinos come only with left-handed helicity while antineutrinos are always right-handed [6]. This completed the lepton part of the SM, seen in figure 1.1.

Figure 1.1: Standard Model of Particles. In the SM, neutrinos are assumed to be massless and purely left-handed. Figure taken from [7].

1.1.2 Neutrino Oscillations

In 1960, neutrinos were posing yet again a new challenge to the understanding of physics: Several experiments, the first being the Homestake experiment, detected a deficit in the measured neutrinos from the Sun compared to expectations from theory, known as the solar neutrino problem [8]. This was solved by the introduction of neutrino oscillations, which were independently measured in the Super-Kamioka-Neutrino Detection Experiment (Super-Kamiokande) [9], and by the Sudbury Neutrino Observatory (SNO) [10] in 1998.

The three flavour eigenstates $|\nu_e\rangle$, $|\nu_\mu\rangle$ and $|\nu_\tau\rangle$ are a superposition of the three mass eigenstates $|\nu_1\rangle$, $|\nu_2\rangle$ and $|\nu_3\rangle$. Due to the mixing of flavour and mass eigenstates, which is described by the Pontecorvo-Maki-Nakagawa-Sakata (PMNS) matrix

$$
\underbrace{\begin{pmatrix} \nu_e \\ \nu_\mu \\ \nu_\tau \end{pmatrix}}_{\text{flavour eigenstate}} = \underbrace{\begin{pmatrix} U_{e1} & U_{e2} & U_{e3} \\ U_{\mu1} & U_{\mu2} & U_{\mu3} \\ U_{\tau1} & U_{\tau2} & U_{\tau3} \end{pmatrix}}_{\text{PMNS matrix}} \underbrace{\begin{pmatrix} \nu_1 \\ \nu_2 \\ \nu_3 \end{pmatrix}}_{\text{mass eigenstate}}
\tag{1.4}
$$

neutrinos can change their flavour during propagation [11]. The PMNS matrix contains three mixing angles θ_1, θ_2 and θ_3, which describe the mixing amplitudes, as well as the CP-violating phase δ_{CP}. If the neutrino is a Majorana particle, two additional Majorana phases are introduced in the PMNS matrix.

In the simplified case of only two flavours α and β, the probability to find a neutrino of initial flavour α and energy E in flavour β after travelling the distance L is given by

$$P_{\alpha \to \beta} = \sin^2\left(2\theta\right) \cdot \sin^2\left(\frac{\Delta m^2}{4E}L\right). \tag{1.5}$$

Because of the dependence of Δm^2, neutrino oscillations are only possible for at least two massive neutrinos. This is a clear evidence for physics beyond the SM [11].

Neutrino oscillation experiments are sensitive to the mixing angles θ_i as well as to the mass squared difference of the mass eigenstates $\Delta m_{ij}^2 = m_i^2 - m_j^2$, $i, j \in [1, 2, 3]$. However, they are not sensitive to the absolute mass of neutrinos, which is still under investigation and will be discussed in more detail in section 1.1.3.

1.1.3 Neutrino Mass

There are different approaches to investigate the absolute mass scale of neutrinos, ranging from cosmological observations, neutrinoless double beta-decay to direct neutrino mass measurements. However, those are sensitive to different neutrino mass observables. The three methods will be explained briefly in the following.

Cosmology

Although only weakly interacting and nearly massless, neutrinos play an important role in the evolution of the universe, e.g. the formation of small and large scale structures [12]. Based on cosmological models, limits on the sum of the three neutrino masses

$$m_\Sigma = \sum_i m_i \tag{1.6}$$

can be derived. Depending on the cosmological model, different results are obtained. A conservative 95 % C.L. upper limit of $m_\Sigma < 0.26\,\text{eV}$ is derived using data from large scale structures of galaxies, cosmic microwave background, type Ia supernovae, and big bang nucleosynthesis. For this, physically motivated neutrino mass models are used, where for example oscillation experiments are also considered [13].

Search for neutrinoless double beta-decay

Another method to obtain information about the neutrino mass is the search for neutrinoless double beta ($0\nu\beta\beta$) decay. In the SM-allowed two-neutrino double beta ($2\nu\beta\beta$) decay, two neutrons in an atom decay to two protons, two electrons

and two electron antineutrinos. However, if the neutrino is a Majorana particle, meaning that it is its own antiparticle, a neutrinoless double beta-decay is possible. In this decay, two neutrons are converted into two protons and two electrons are emitted.

In $0\nu\beta\beta$ experiments, the half-life $T_{1/2}^{0\nu}$ of the decay is measured. From the half-life, the effective Majorana mass

$$|m_{\beta\beta}| = \left| \sum_i m_i U_{ei}^2 \right| \tag{1.7}$$

can be calculated, which depends on the mixing parameters of the electron flavour in the PMNS matrix U_{ei}. Additionally, the nuclear matrix element is needed for the calculation of the effective Majorana mass from the half-life of the $0\nu\beta\beta$ decay. However, this is model-dependent and therefore introduces uncertainties.

While $2\nu\beta\beta$ decay conserves lepton number, in $0\nu\beta\beta$ decay the lepton number conservation is violated by two units. Therefore, besides gaining information about the neutrino mass scale, a detection of neutrinoless double beta-decay would prove the Majorana nature of the neutrino and could shed light on the matter-antimatter-asymmetry [14].

One experiment searching for this kind of decay was the GERmanium detector Array (GERDA) experiment located at the Laboratori Nazinali del Gran Sasso (LNGS) in Italy. It consisted of high-purity germanium detectors using the isotope ^{76}Ge. Liquid argon around the detectors provided shielding and cooling. GERDA obtained an upper limit on the effective Majorana neutrino mass of $m_{\beta\beta} < 79 - 180$ meV at 90 % C.L. The range is due to the uncertainty of the nuclear matrix element which is needed to calculate the effective Majorana neutrino mass from the measurement [15]. This work is now continued by the Large Enriched Germanium Experiment for Neutrinoless $0\nu\beta\beta$ Decay (LEGEND) [16].

Other experiments searching for $0\nu\beta\beta$ decay are for example the Enriched Xenon Observatory (EXO), which uses the isotope ^{136}Xe [17] and the Cryogenic Underground Laboratory for Rare Events (CUORE), which uses bolometers containing the isotope ^{130}Te [18].

Beta-decay

The most model-independent way to probe the neutrino mass is the investigation of the decay kinematics of single beta-decay or electron capture. In the single beta-decay, see equation (1.1), an electron antineutrino and an electron are emitted. The decay energy Q_{tot} is split into the recoil energy E_{rec} of the nucleus and the endpoint energy E_0. Both particles carry part of the endpoint energy E_0, which can be calculated from theory. In the SM, where the neutrino is massless, the endpoint of the electron spectrum would therefore correspond to the entire available endpoint

energy E_0, as the neutrino would not carry away any energy. However, it is known that the neutrino is a massive particle, therefore this is not the case in reality. Instead, even for the most energetic electrons emitted from the decay, they can only carry $E_0 - m_\beta$ since the massive neutrino has to be produced. This alters the shape of the endpoint of the beta spectrum as well as the measured endpoint energy. From this, the effective electron antineutrino mass

$$m_\beta^2 = \sum_i m_i^2 |U_{ei}|^2 \tag{1.8}$$

can be measured.

The most sensitive experiment today is the KArlsruhe TRItium Neutrino (KAT-RIN) experiment, which will be explained in more detail in section 2.1. It uses the beta-decay of tritium and obtained a current upper limit of $m_\beta < 0.8\,\text{eV}$ at $90\,\%$ C.L. [19]. The final sensitivity of the KATRIN experiment is expected to be on the order of $200\,\text{meV}$ [20].

Other experiments aiming to determine the neutrino mass via the kinematics of radioactive decays are for example HOLMES and ECHo, which both use the electron capture on Ho^{163} [12], and Project 8, which uses Cyclotron Radiation Emission Spectroscopy [21].

1.2 Sterile Neutrino Physics

There are still many open questions in the field of neutrino physics. As only left-handed particles with a very small mass neutrinos are different compared to the other particles in the SM. Neutrino oscillations have proven the existence of physics beyond the SM and that neutrinos are massive. Since the Yukawa coupling to the Higgs field, which gives other particles in the SM their mass, requires a right-handed counterpart for the concerning particle, it is a natural, small addition to the SM to include right-handed neutrinos.

As neutrinos only interact weakly, right-handed neutrinos would not interact at all, they would be "sterile". This introduces a sterile flavour eigenstate $|\nu_s\rangle$, the so called sterile neutrino, and a corresponding mass eigenstate $|\nu_4\rangle$. Theoretically, many such sterile eigenstates with different masses can exist. In the case of only one sterile eigenstate, the PMNS matrix would be extended to a 4x4 matrix

$$\begin{pmatrix} \nu_e \\ \nu_\mu \\ \nu_\tau \\ \nu_s \end{pmatrix} = \begin{pmatrix} U_{e1} & U_{e2} & U_{e3} & U_{e4} \\ U_{\mu 1} & U_{\mu 2} & U_{\mu 3} & U_{\mu 4} \\ U_{\tau 1} & U_{\tau 2} & U_{\tau 3} & U_{\tau 4} \\ U_{s1} & U_{s2} & U_{s3} & U_{s4} \end{pmatrix} \begin{pmatrix} \nu_1 \\ \nu_2 \\ \nu_3 \\ \nu_4 \end{pmatrix}. \tag{1.9}$$

Because of the mixing of the mass eigenstate $|\nu_4\rangle$ with the active eigenstates $|\nu_i\rangle$, $i \in [1, 2, 3]$, the sterile neutrino would contain a small active component. This mixing

is depending on the matrix elements U_{si}, $i \in [1, 2, 3]$ and is in general very small. Nevertheless, this makes the search for sterile neutrinos possible.

A sterile neutrino mass eigenstate can in principle have an arbitrary mass. There are different motivations for different mass scales, which will be discussed briefly in the following.

Sterile neutrino in the GeV mass scale: Neutrino mass

All particles in the SM, except the neutrino, obtain their mass through Yukawa coupling to the Higgs field. To this end, a right-handed counterpart of the particle is needed, which is why this is impossible for neutrinos in the SM. With the introduction of the right-handed, sterile neutrinos, this would become possible. However, this would result in an unnaturally small coupling constant in order to explain the lightness of active neutrinos [12]. This is a strong argument against a SM origin of the neutrino mass.

Another possibility for massive neutrinos is the See-Saw mechanism. Then, from the new Lagrangian and mass matrix, two mass eigenstates can be derived:

$$m_1 = \frac{m_D^2}{m_R} \tag{1.10}$$

and

$$m_2 \approx m_R, \tag{1.11}$$

with m_D denoting the Dirac Mass and m_R being the Majorana mass of the sterile neutrino. A heavy sterile neutrino with a Majorana mass of $\mathcal{O}(\text{TeV})$ would therefore automatically lead to a small active neutrino mass m_1 [12, 22].

Sterile neutrino in the keV mass scale: Dark Matter

Sterile neutrinos in a mass range of $\mathcal{O}(\text{keV})$ are especially interesting as they serve as potential Dark Matter (DM) candidates. Depending on their production mechanism they can act as Warm Dark Matter (WDM) or Cold Dark Matter (CDM). WDM would mitigate tensions regarding small scale structures in the universe, e.g. the missing satellite problem and the cusp-core problem [12, 22]. One experiment which will search for sterile neutrinos in the keV mass range is the KATRIN experiment with the novel TRISTAN detector. The principle of the sterile neutrino search as well as the experimental setup will be explained in more detail in sections 2.1 and 2.2.

Sterile neutrino in the eV mass scale: Gallium anomaly

Sterile neutrinos with a mass of $\mathcal{O}(\text{eV})$ are proposed to solve several anomalies, for example possible ν_e disappearance in Gallium experiments such as SAGE and GALLEX. The deficit could be explained by an oscillation of the active electron neutrino into an eV-scale sterile neutrino. Recently, the Baksan Experiment on

Sterile Transitions (BEST) experiment confirmed the results of SAGE [23] and GALLEX [24] with higher significance. The best fit of the data is consistent with a $\Delta m^2 = 3.3^{+\infty}_{-2.3}$ eV^2 sterile neutrino [25]. The excess of $\bar{\nu}_e$, that was found by the short baseline experiments LSND and MiniBooNE could also be explained by an active to sterile neutrino oscillation. However, there is a tension with other disappearance or appearance results [12, 26, 27].

Chapter 2

The KATRIN Experiment

The neutrino mass can be probed by direct measurements of the kinematics of single beta-decays due to the alteration of the endpoint of the electron energy spectrum. One experiment investigating the effective electron antineutrino mass is the KArlsruhe TRItium Neutrino (KATRIN) experiment, which uses tritium as a decaying isotope and is explained in detail in section 2.1. In addition to measuring the effective electron antineutrino mass, the KATRIN experiment can also be used to search for sterile neutrinos if their mass is smaller than the endpoint energy of tritium. However, the detector has to be upgraded for this task. For this, the novel TRISTAN detector is currently being developed. The signal of a sterile neutrino in the beta-decay spectrum as well as the requirements for the new detector are described in section 2.2.

2.1 Current KATRIN Experimental Setup

The KATRIN experiment is the successor of the Mainz and Troitsk experiments. Both experiments investigated the effective electron antineutrino mass and set an upper limit of $m_\beta \leq 2.3\,\text{eV}$ [28] and $m_\beta < 2.12\,\text{eV}$ [29] (95 % C.L.), respectively. The KATRIN experiment aims for a final sensitivity of about $0.2\,\text{eV}$ (90 % C.L.) [20] and obtained a current upper limit of $m_\beta < 0.8\,\text{eV}$ at 90 % C.L. [19]. If not stated otherwise, the general reference for the following sections is the KATRIN design report [20].

2.1.1 Neutrino Mass Measurement

The KATRIN experiment uses the isotope tritium for the investigation of the effective electron antineutrino mass via the kinematics of single beta-decay. Tritium is advantageous because of several properties. Its comparably low endpoint energy of $E_0 = 18.6\,\text{keV}$ and short half-life of $T_{1/2} = 12.3\,\text{a}$ ensure reasonable statistics in the endpoint region. Moreover, tritium beta-decay is super-allowed, leading to a pure phase space spectrum.
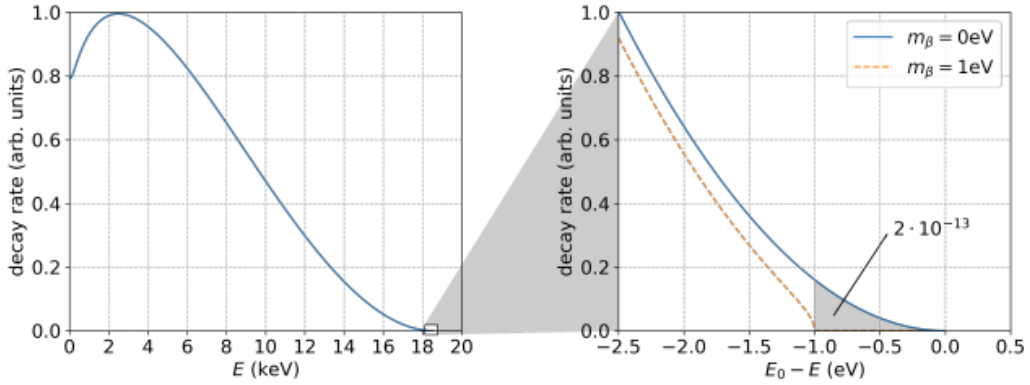
Figure 2.1: Tritium beta-decay spectrum (left) with zoom on the endpoint region (right). The blue curve corresponds to the spectrum if the neutrino was massless. The orange dashed line assumes an effective electron antineutrino mass of $1\,\mathrm{eV}$. In the case with the massive neutrino, the shape of the spectrum in the endpoint region is altered and the spectrum ends below the calculated endpoint energy E_0. Note that only a fraction of 2×10^{-13} electrons falls into the shaded area. Figure taken from [30].

Furthermore, tritium has well-understood final states, due to being the isotope with the lowest atomic number Z. This facilitates understanding and modelling the tritium beta-decay spectrum.

As explained in section 1.1.3, the effective electron antineutrino mass can be extracted from the investigation of the endpoint region of the beta-decay spectrum. The presence of a massive neutrino with an effective mass m_β will shift the observed endpoint energy to $E_0 - m_\beta$ with respect to the calculated endpoint energy E_0. In addition, it alters the shape of the spectrum in the endpoint region. This is illustrated in figure 2.1. In principle, every mass eigenstate leads to such a shift and spectral distortion. However, due to the tiny mass differences, the individual effects of the mass eigenstates cannot be distinguished. Therefore, only the shift and distortion of the effective electron antineutrino mass can be measured.

2.1.2 Experimental Setup

For the neutrino mass measurement, a complex experimental setup is needed, which is shown in figure 2.2. The $70\,\mathrm{m}$-long beamline consists of the rear section, the tritium source, the transport section, the spectrometers as well as the detector, which will be described in more detail in the following paragraphs.
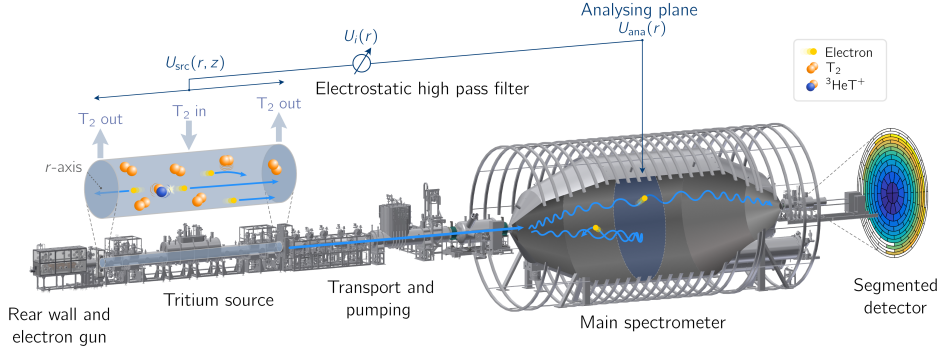
Figure 2.2: A technical drawing showing the beamline of the KATRIN experiment. Calibration and monitoring devices are installed in the rear section at the left hand side. The Windowless Gaseous Tritium Source provides the electrons. There, tritium is injected in the middle of a tube and diffuses to both ends while decaying. Because the tritium is not confined by barriers, the electrons suffer no energy loss. In the transport section, electrons are guided by a magnetic field towards the spectrometer, while tritium is pumped out to prevent contamination and background in the spectrometer. The two spectrometers with MAC-E filters filter electrons with sufficient energies which can then reach the focal plane detector at the right hand side of the beamline. Courtesy of the KATRIN collaboration.

Rear section

In the rear section, various calibration and monitoring devices are installed. Among these is a multi-purpose electron gun which measures the KATRIN response function and investigates systematic effects, as well as a rear detector which monitors the source activity. In addition, a gold-plated rear wall is installed to measure the plasma potential of the WGTS as well as reduce backscattering for the backreflected electrons. This also reduces systematic uncertainties.

Windowless Gaseous Tritium Source

The Windowless Gaseous Tritium Source (WGTS) is the β-electron source of KATRIN, which provides a high and stable decay rate (10^{11} Bq with a stability of $\pm 0.1\,\%$) while introducing only small systematic uncertainties. To avoid energy losses at any kind of barrier between the source and detector, the WGTS solely consists of the open WGTS tube. In the middle of this tube ultra-cold molecular tritium gas is injected and diffuses to both ends of the tube.

Transport and Pumping Section

Tritium is not allowed to reach the spectrometer and detector section, as this would cause additional background. For this reason, the tritium flow is reduced by 14 orders of magnitude in the pumping section. In the differential pumping section, Turbo Molecular Pumps (TMPs) are used to reduce the tritium flow. In the cryogenic pumping section a $3\,\mathrm{K}$ argon frost layer on the walls is used to trap the remaining tritium molecules. In addition, the transport section is arranged in chicanes. While the electrons follow the magnetic field lines through the transport section, the tritium molecules are unaffected by the magnetic field and will therefore bump into the walls, increasing the efficiency of trapping them in the cryogenic pumping section.

Spectrometers

To look for the shift of the measured endpoint energy and the spectral distortion caused by the effective electron antineutrino mass, an excellent energy resolution is needed, which cannot be reached using conventional semiconductor detectors. Therefore, KATRIN deploys a main spectrometer using a Magnetic Adiabatic Collimation combined with an Electrostatic (MAC-E) filter, which was first proposed by P. Kruit [31]. A retarding electric potential U_{ret} is applied to the spectrometer. Electrons with sufficient kinetic energy $E_{\mathrm{kin}} = E_{\parallel} + E_{\perp}$ to overcome this potential can reach the detector. By setting the electric potential to different values and counting the electrons that reach the detector, an integral measurement of the beta-decay spectrum is performed. Therefore, the energy resolution is driven by the spectrometer and not by the detector itself.

As the electric potential is applied in longitudinal direction, it is only sensitive to the longitudinal component of the electron energy $E_{\parallel}$. The transversal component of the energy $E_{\perp}$ is not affected. To ensure that all electrons with a total kinetic energy higher than qU_{ret} are able to reach the detector, the transversal component has to be converted into the longitudinal component. This is achieved by a magnetic field gradient. The magnetic field B_{S} is strong at the source and decreases along the spectrometer until is reaches the minimum strength B_{min} at the position where the electric potential U_0 is maximal. This position is called the analysis plane. At the detector region, the magnetic field B_{max} is maximal. The electrons are moving adiabatically through the spectrometer and their orbital magnetic moment

$$\mu \approx \frac{E_{\perp}}{B} = \mathrm{const.} \tag{2.1}$$

is conserved. Therefore, the transversal momentum of the electron is converted into the longitudinal momentum. As a result the electric potential is sensitive to the total kinetic energy. The working principle of the MAC-E filter is illustrated in figure 2.3.
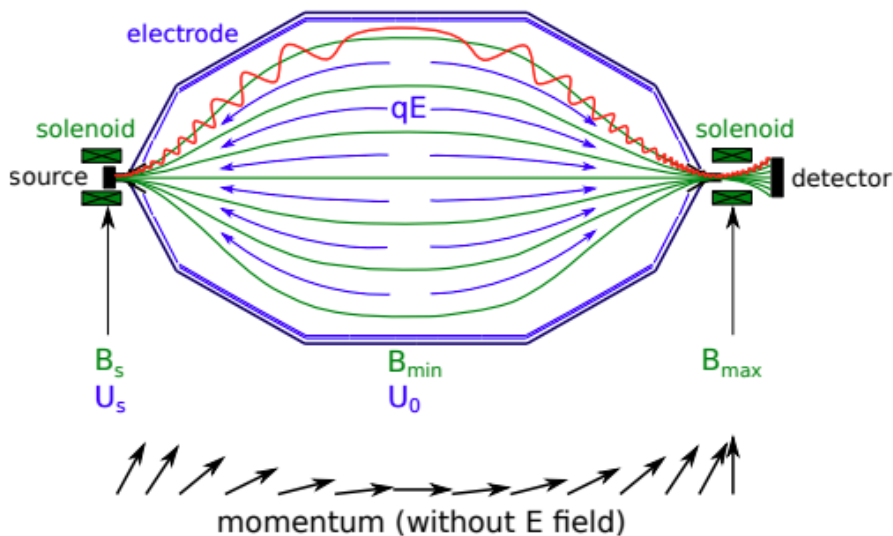
Figure 2.3: Working principle of a MAC-E filter. A magnetic field gradient is produced by superconducting magnets (green). The magnetic field transforms the transversal momentum of the electrons into longitudinal momentum (electron path: red, momentum transformation: lower part). The longitudinal electric field (blue) filters out electrons with sufficient longitudinal energy $E_\parallel < |qU_0|$. Figure taken from [32].

The efficiency of the transformation of transversal into longitudinal momentum defines the energy resolution ΔE:

$$\frac{\Delta E}{E} = \frac{B_{\min}}{B_{\max}}. \tag{2.2}$$

With the MAC-E filter, KATRIN reaches an energy resolution of $\Delta E = 0.93\,\mathrm{eV}$ at the endpoint of the tritium beta-decay spectrum with $E_0 = 18.6\,\mathrm{keV}$ [32], if operated with $B_{\min} = 3 \cdot 10^{-4}\,\mathrm{T}$ and $B_{\max} = 6\,\mathrm{T}$.

There are two MAC-E-type spectrometers in the KATRIN beamline, the pre- and the main spectrometer. The pre-spectrometer was originally designed and used to reduce the amount of electrons reaching the main spectrometer, therefore reducing the background. From the beginning of the fifth measurement phase however, the pre-spectrometer will be switched off, as the interplay between pre- and main spectrometer creates a Penning trap between them. The main spectrometer is sufficient for KATRIN measurements and filters out all electrons with energies below the retarding potential. With the main spectrometer, an integral measurement can be performed.
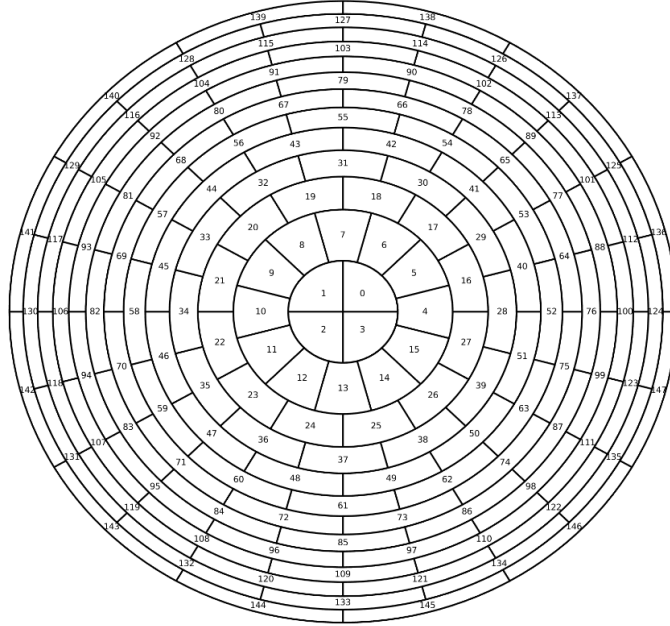
Figure 2.4: Pixel layout of the focal plane detector, with 148 pixels arranged in a ring-wise structure. All pixels have the same area. Figure taken from [34].

Focal Plane Detector

The KATRIN detector consists of a 148-pixel positive intrinsic negative (PIN) diode made out of silicon. The pixels are arranged ring-wise and have an equal area in order to distribute the count rate evenly. The detector has an energy resolution of $\Delta E_{\mathrm{FWHM}} = 1.52\,\mathrm{keV}$ at $18.6\,\mathrm{keV}$ and is able to handle a maximal count rate up to tens of kcps [33]. As the energy resolution is determined by the MAC-E filter and the detector is only used for counting the electrons in the endpoint region of the spectrum, this is sufficient for the neutrino mass measurement. The pixel layout of the Focal Plane Detector can be seen in figure 2.4.

2.2 The TRISTAN Detector System

As discussed in chapter 1, the mixing between active and sterile neutrinos makes it possible to search for sterile neutrinos in the beta-decay spectrum with a mass up to the endpoint energy of tritium. The presence of a sterile neutrino would impact the beta-decay spectrum in a similar way as the active neutrino. However, the current KATRIN detector is designed to handle only low count rates and does not have

sufficient energy resolution. Therefore, the KATRIN detector has to be upgraded for the search for keV-scale sterile neutrino. To this end, a novel TRISTAN detector is currently being developed, which will be integrated into the KATRIN beamline.

2.2.1 Imprint of the Sterile Neutrino in Single Beta-Decay

The active neutrino mass eigenstates alter the shape of the beta-decay spectrum close to the endpoint and shift the observed endpoint energy. However, the mass differences are too small to be distinguished, leading to only one observable: the effective electron antineutrino mass. If the sterile neutrino exists, a fourth sterile mass eigenstate m_4 would need to be introduced. Due to the mixing of active and sterile neutrinos, which can be characterised by the mixing angle θ_s, the beta spectrum would be a superposition of the decay rates $\frac{d\Gamma}{dE}$ of the active states with the sterile state [12]:

$$\frac{d\Gamma}{dE} = \underbrace{\cos^2(\theta_s)\frac{d\Gamma(m_\beta)}{dE}}_{\text{active}} + \underbrace{\sin^2(\theta_s)\frac{d\Gamma(m_4)}{dE}}_{\text{sterile}} . \tag{2.3}$$
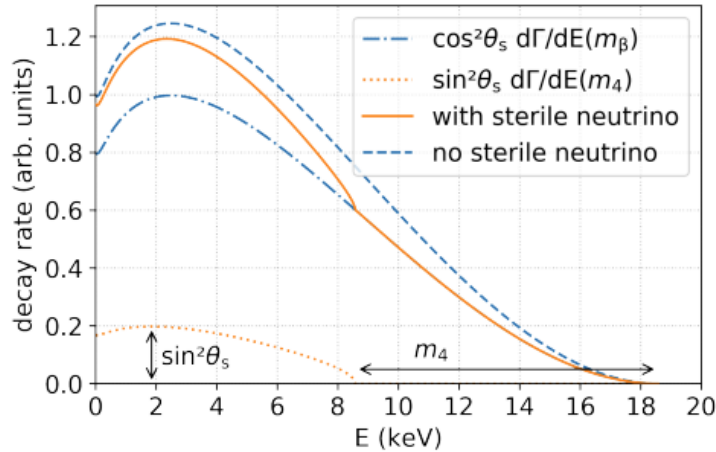
Figure 2.5: Imprint of a sterile neutrino on the tritium beta-decay spectrum. The blue dashed line illustrates the beta spectrum in the case that no sterile neutrino exists in the mass range of the tritium beta-decay. The solid orange line depicts the spectrum with a sterile neutrino with mass m_4, which is then a superposition of the active neutrino branch (dashed-dotted blue) and the sterile neutrino branch (dashed-dotted orange). At $E = E_0 - m_4$, there is a kink-like distortion in the spectrum. The height of this kink depends on the mixing amplitude $\sin^2(\theta_s)$. Figure taken from [30].

The sterile mass eigenstate would therefore lead to another spectral distortion in the beta spectrum.

The location of the kink-like signature depends on m_4, while the signal strength depends on the mixing amplitude $\sin^2(\theta_s)$ [12]. Because the mass of the sterile mass eigenstate is unknown and could in principle take any value, the sterile neutrino does not necessarily affect the endpoint region of the beta spectrum. A keV-scale sterile neutrino for example, which is a suitable DM candidate, would rather result in a kink somewhere in the middle of the spectrum. The effect of a keV-scale sterile neutrino on the beta spectrum of tritium is illustrated in figure 2.5.

Together with a novel TRISTAN detector and readout system, the design goal of the KATRIN experiment is to search for sterile neutrinos with masses up to $18.6\,\mathrm{eV}$ and a mixing angle of $\sin^2(\theta_s) < 10^{-6}$.

2.2.2 Requirements for the TRISTAN Detector System

For the currently ongoing neutrino mass measurements, the focal plane detector is used. For these measurements only the endpoint region of the beta spectrum is of interest. Therefore, only a small amount of electrons reach the detector. Furthermore, the energy resolution of the detector is irrelevant, since the integral measurement technique relies solely on the energy resolution of the MAC-E filter. The characteristic signature of a sterile neutrino, however, could be located anywhere in the spectrum. Therefore, the whole spectrum has to be measured and analysed. This can be done either in the integral mode, in which the retarding potential is varied and the detector counts the incoming electrons for each setting, or in the differential mode, in which the retarding potential is set to a low value to let electrons over a broad energy range reach the detector. In both cases, as the retarding potential is lowered and more electrons reach the detector, it has to be able to handle high total count rates up to 10^8 cps for a three year data-taking period. To reduce the pile-up probability, a minimum of 1000 pixels is required. For the differential mode, an excellent energy resolution of about $\Delta E_{\mathrm{FWHM}} \approx 300\,\mathrm{eV}$ at $20\,\mathrm{keV}$ is crucial to be able to resolve a kink-like structure in the spectrum. Consequently, the current KATRIN detector is not suited for a keV-scale sterile neutrino search and a novel detector and readout system is needed [35].

The novel detector system is currently under development and includes the TRISTAN detector [36, 37]. It is a multipixel Silicon Drift Detector (SDD) array, which will be read out by a highly customised Data Acquisition System (DAQ). The SDD technology is described in chapter 3, while the detector module is introduced in chapter 4.

2.2.3 Staged Approach

The development of the TRISTAN detector is carried out in multiple stages with different detector sizes (number of pixels). In a first proof of concept, 7-pixel devices with and without integrated JFETs were produced and tested in order to verify the suitability of using the SDD technology for electron spectroscopy [36]. Subsequently, larger devices, 47-pixel and 166-pixel detectors, were produced in different configurations to test and characterise the detector in a realistic MAC-E filter environment. For the operation of 166-pixel detectors, three phases are foreseen.

Phase 0

In phase 0, one 166-pixel detector module will be tested in the KATRIN Monitor Spectrometer. This environment closely resembles the conditions in the KATRIN beamline. This thesis will focus on this milestone.

Phase 1

In phase 1, nine 166-pixel detector modules will be operated together in a first sterile neutrino search in the KATRIN beamline. This detector configuration will have about 1500 pixels and is shown in figure 2.6a.

Phase 2

A possible second stage will consist of 21 detector modules with a total of 3486 pixels. A technical drawing of the second stage detector is shown in figure 2.6b.

The statistical sensitivity (95 % C.L.) for the KATRIN experiment with the TRISTAN detector is shown in figure 2.7. The KATRIN experiment with the novel TRISTAN detector will improve the current laboratory limits for the mixing angle θ_s by 3 orders of magnitudes for masses up to 18.6 keV.

(a) Phase 1: Nine modules.

(b) Phase 2: 21 modules.
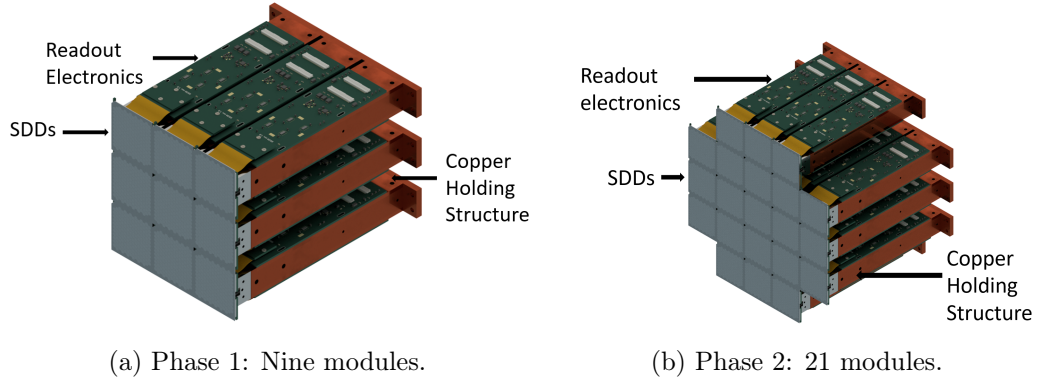
Figure 2.6: (a) Technical drawing of the arrangement of nine TRISTAN detector modules with a total of 1494 pixels (Phase 1). This detector will replace the current KATRIN focal plane detector and will be used for the search for keV-scale sterile neutrinos. (b) Technical drawing of the arrangement of 21 TRISTAN detector modules with a total of 3486 pixels (Phase 2). In a possible phase 2, this detector could replace the phase 1 TRISTAN detector.
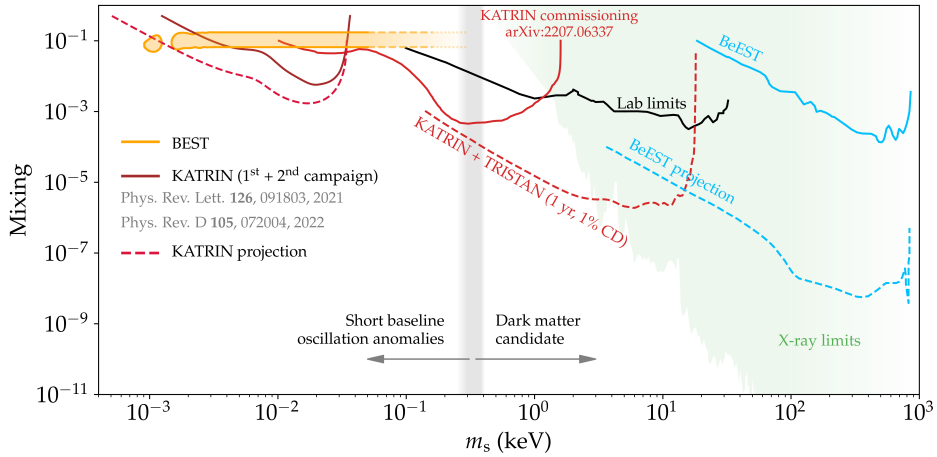
Figure 2.7: Statistical sensitivity for the KATRIN experiment with the TRISTAN detector integrated into the KATRIN beamline. Current laboratory limits are visualised with the solid black line. The solid red line represents the sensitivity of the KATRIN first and second campaign. The dashed red line represents the sensitivity of the KATRIN experiment with the TRISTAN detector after 1 y of data taking. X-ray limits are represented by the green area, the experiments BeEST (blue) and BEST (orange) are also depicted. Courtesy of the KATRIN collaboration.

Chapter 3

Silicon Drift Detector Technology

The final TRISTAN detector will consist of multiple modules, see chapter 4. The centerpiece of each module is an SDD matrix consisting of 166 pixels. The SDD technology was chosen because it meets the requirements described in section 2.1, i.e. the capability of handling high count rates while maintaining a good energy resolution. In section 3.1, the basics of semiconductor physics will be explained. Section 3.2 will give an overview of the SDD technology with a short explanation of the important voltages, which have an impact on the detector performance. Electrons lose their energy quickly in matter. Therefore, for detectors measuring electrons, it is crucial to have only a thin area with reduced detection efficiency at the entrance window side. The entrance window effect for the TRISTAN detector will be described in more detail in section 3.3.

3.1 Semiconductor Physics Basics

In general, there are three types of materials: conductors (metals), semiconductors and insulators, see figure 3.1. In the band model, the states electrons can occupy are described by bands. For $T = 0\,\mathrm{K}$, the valence band is the band with the highest energy that is occupied by electrons. The conduction band is the band with the next higher energy. In metals, there is no band gap, meaning that electrons can move freely from the valence to the conduction band. Insulators are characterised by a large band gap. The valence band is completely filled while the conduction band is empty. This is also true for semiconductors in the absence of thermal excitations. However, semiconductors are materials with a narrow band gap. Therefore, thermal excitations of electrons from the valence to the conduction band are possible even at low temperatures. Then, a weak conductivity is created due to free electrons and holes [38, 39].

Via doping, the conductive properties of the material can be changed. Doping is the process of replacing one atom in the crystal lattice with another element that acts either as an electron donor or an electron acceptor. Those impurities lead to additional acceptor or donor levels inside the band gap, close to the valence band or conduction band, respectively.
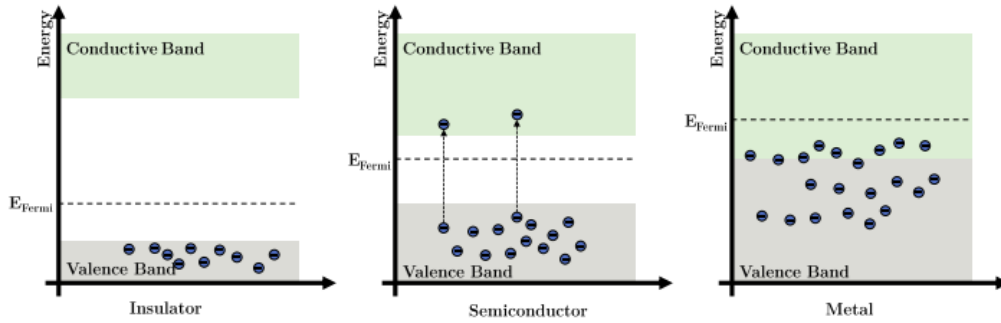
Figure 3.1: Illustration of the band gap of metals (right), semiconductors (center) and insulators (left). The Fermi energy E_{Fermi} describes the highest energy that electrons can take if the system is in the ground state. In insulators, the band gap is large and the conduction band is empty. Semiconductors have a narrow band gap and electrons can be excited from the valence band into the conduction band, making conductivity possible. Metals are always conducting due to the missing band gap. There, both valence and conduction band are filled. Figure taken from [40].

Due to these new levels, the energy to excite electrons from the valence into the conduction band is decreased. This is illustrated in figure 3.2. Common electron donors for materials in the IV group of the periodic table are elements in the V group, for example phosphorous and arsenic. Both have five valence electrons, four of which are used for the formation of covalent bonds in the lattice. One electron remains free for conduction. This is used for n-type doping. For p-type doping, electron acceptors, elements in the III group with three valence electrons are used. In this case, one electron is missing in the covalent bond, creating a hole that is free for conduction. A common electron acceptor is boron [39].

One of the most commonly used structures for semiconductors is the p-n junction, illustrated in figure 3.3. As the name suggests, n-type material is adjoined to p-type material, forming a diode. This leads to a diffusion of electrons from the n region to the p region and of holes from the p to the n region. The charge separation leads to an electric field of opposite polarity which counteracts this diffusion and establishes equilibrium. A space-charge region is formed at the border of the n- and p-type regions. There, all free charge carriers have diffused away and only ionized electron acceptors and donors are left. This region is called the depletion zone. Normally, this depletion zone is small. However, the whole bulk can be depleted by applying a reverse bias voltage [38].
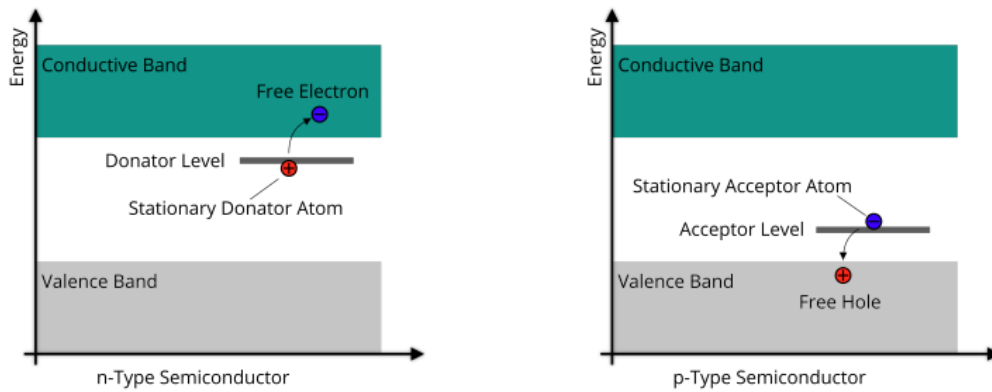
Figure 3.2: Donor (left) and acceptor (right) level in the band gap of a semiconductor, introduced by doping. Additional donor levels are created near the conduction band in the case of n-type semiconductors. For p-type semiconductors, acceptor levels close to the valence band are created. Figure taken from [41].

The depletion zone is important for the use of semiconductors as particle detectors. When an ionising particle moves through the semiconductor, it creates electrons, mostly via ionisation. Those electrons can be guided to an electrode where the signal is read out. However, this signal will only be detectable if there aren't free charge carriers from e.g. thermal excitation. This is ensured by depleting the semiconductor material completely by applying a reverse bias.
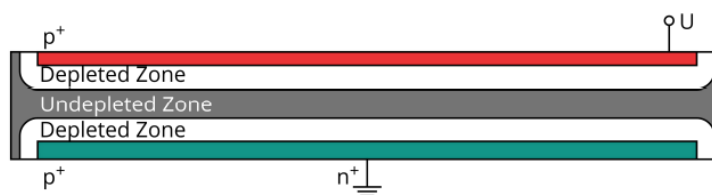
Figure 3.3: Illustration of a PIN-Diode. Electrons move from the n-type material to the p-type material. Holes express the opposite behaviour. Close to the n^+ and p^+ contacts, a depleted region is formed, where only ionized doping atoms are left. In this illustration, the applied bias voltage U is not high enough to deplete the whole bulk, leaving behind an undepleted region in the center of the semiconductor. Figure taken from [41].

To ensure a good energy resolution, semiconductor detectors have to be cooled down for operation. This is due to the leakage current, which is caused by spontaneous excitations of electrons into the conduction band. The band gap size decreases slightly for increasing temperature, leading to more leakage current as less energy is needed for electrons to move into the conduction band. Therefore, the leakage current can be reduced significantly by cooling the detector.

3.2 TRISTAN Silicon Drift Detector

The TRISTAN detectors are Silicon Drift Detectors (SDDs), a special kind of semiconductor detectors. For the readout of the signals, custom-made readout electronics were designed to fulfill the requirements for the detectors.

3.2.1 Silicon Drift Detector Working Principle

In the SDD, silicon is used due to its small band gap $E_g = 1.12\,\mathrm{eV}$ [38] and small electron-hole pair creation energy of $E_{pair} = 3.67\,\mathrm{eV}$ [42]. This results in a good energy resolution even at moderate cooling. Moreover, silicon has a high abundance in the earth crust and can be processed with high purity. The SDD consists of a p-n junction which is depleted by sidewards depletion [43]. The basis of the SDD is a bulk of n^--type silicon. The bottom surface (entrance window side) of the detector is made from a thin layer of p^+-type silicon, the back contact. The detector top surface features several p^+-type drift rings. Both back contact and drift rings are responsible for the depletion of the detector. The drift rings surround a small n^+-doped anode and, in the case of the TRISTAN SDD, a junction-gate field-effect transistor (JFET). The schematic of an SDD as used for the TRISTAN detectors can be seen in figure 3.4.

The negative potential of the drift rings increases from the center outwards, shaping the electric field across the whole device. This is illustrated in figure 3.5. In contrast to the PIN-diode, the SDD with sidewards depletion only requires a small anode. This is beneficial to the energy resolution of the detector, as this leads to a smaller anode capacitance and therefore to a smaller noise contribution. Moreover, this design allows for a multi-pixel design without dead areas between the pixels, as the pixel boundaries are defined only by the electric field. The gapless pixel arrangement as well as the on-chip readout structure can be seen in a microscope picture of a part of a TRISTAN SDD in figure 3.6.

When an ionising particle enters the depleted region, it creates electron-hole pairs. The amount of those electron-hole pairs is proportional to the energy of the incoming particle. The electric field created by the electrode and in particular the drift ring structure guides the electrons to the collecting anode. The signal is then fed to the JFET, which serves as a first amplification stage of the signal.
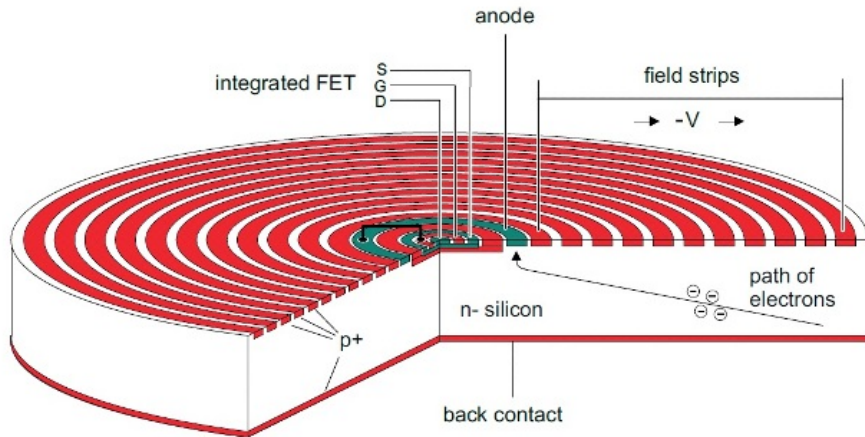
Figure 3.4: Schematics of a TRISTAN SDD. The detector bulk is made from n^--type silicon and is surrounded by p^+-type silicon on the bottom (back contact) and p^+-doped drift rings on top (red). The drift rings surround the n-type anode and the integrated JFET (green). When ionising particles enter the depleted region, electron-hole pairs are created and guided by an electric field to the collecting anode. Figure taken from [44].

An internal JFET is chosen over an external JFET in order to avoid bond connections. Those would introduce parasitic bond pad capacitances. In addition, the first amplification stage is located closer to the signal if carried out by an integrated JFET. Both the lack of parasitic bond pad capacitances and the location of the first amplification stage decrease the electronic noise, leading to a better energy resolution.

23
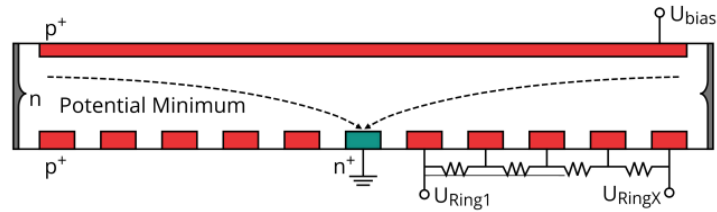
Figure 3.5: Illustration of the electrode arrangement inside an SDD. The applied bias voltage to the back contact on top as well as the drift rings at the bottom (both red) deplete the entire bulk of the semiconductor if the applied voltage is high enough. The drift rings at the bottom create a favoured potential for electrons at the anode in the center (green). The created electrons will be guided to the anode. Figure taken from [41].
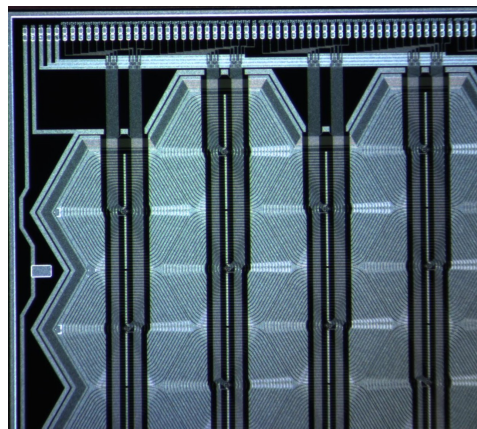
Figure 3.6: Microscope picture of a part of a 166-pixel TRISTAN SDD. The roughly hexagonal drift rings define the pixel boundaries, which allows for a gapless pixel arrangement. A readout line connects each pixel with the contacts at the border of the SDD, so that voltages can be distributed and signals can be transferred.

3.2.2 SDD Readout Electronics

To read out the signals from the detector with an integrated JFET, the Italian company XGLab designed a custom Application-Specific Integrated Circuit (ASIC), the ETTORE ASIC, in collaboration with Politecnico di Milano [45]. Each ETTORE ASIC is a charge sensitive (pre-)amplifier and is responsible for 12 pixels of the detector. The simplified block diagram of one ETTORE channel can be seen in figure 3.7.
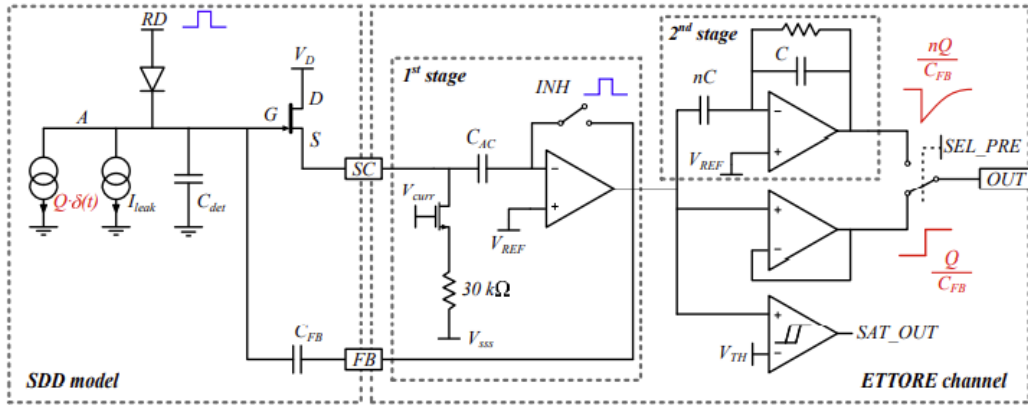
Figure 3.7: Schematic block diagram of one ETTORE ASIC channel. The block diagram of the detector is shown on the left. The detector has a reset diode (RD) to prevent the saturation of the output. In the center, the first stage of the ETTORE ASIC can be seen, which produces the characteristic ramp output. On the right, the second stage is visible. Figure taken from [46].

The output of the ETTORE ASIC can be switched to first or second stage. The first stage output consists of the classical voltage ramp signal, where the leakage current of the detector is responsible for the slope of the ramp and the signals are superimposed steps. An exemplary first stage waveform is shown in figure 3.8. The second stage output introduces a gain factor, which can be chosen to be either 5 or 10, and features an exponential decay constant of about 15 µs. However, it requires a deconvolution operation to be converted to a spectrum. For more information on the ETTORE ASIC, see [45].

During the operation of the detector, the detector has to be reset periodically to prevent the saturation of the first stage output. The signal for the reset is provided by external electronics and the reset itself is done with a reset diode. The reset is applied to all detector pixels simultaneously.
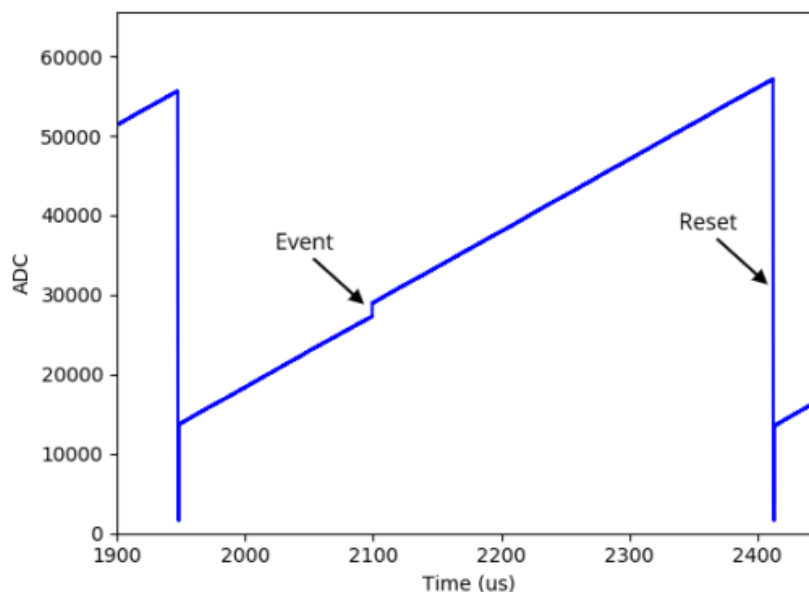
Figure 3.8: Exemplary first stage waveform. The characteristic ramp can be seen, which is caused by an accumulation of charge due to the leakage current. To avoid a saturation of the ETTORE ASICs, the detector has to be reset. The resets can be seen at the start and the end of the ramp. In the first stage, events appear as steps on the waveform. Figure taken from [40].

3.2.3 Overview of Important Detector Voltages

There are several important detector voltages which have to be applied to the SDD and significantly affect the detector performance. Those will be quickly introduced in the following.

Back Contact (BC)

This is the voltage which is required to deplete the detector volume. It is applied to the entrance window side (back contact). This voltage expands the depletion zone of the detector to the whole bulk. Expected values for the TRISTAN detector are $-120\,\mathrm{V} \leq V_{\mathrm{BC}} \leq -80\,\mathrm{V}$.

Back Frame (BF)

This is the voltage applied to the ring surrounding the p-type silicon of the entrance window and helps to define the electrical field for the outer borders of the pixels. Expected values for the TRISTAN detector are $-130\,\mathrm{V} \leq V_{\mathrm{BF}} \leq -90\,\mathrm{V}$.

Inner Guard Ring

The inner guard ring guards the integrated JFET from electrons. A voltage is applied, leading to a potential that causes the electrons to drift away from the center to the anode. A signal from electrons that would pass directly to the JFET instead of the anode would not be amplified and would therefore be too small to be detected. Expected values for the TRISTAN detector are $-30\,\text{V} \leq V_{\text{IGR}} \leq -20\,\text{V}$.

Ring 1 and Ring X

Ring 1 is the innermost drift ring, which has the lowest negative voltage applied to. Ring X is the outermost drift ring with the highest negative voltage applied to. The drift rings are responsible for the potential gradient which guides the electrons to the collecting anode. Ring 1 and ring X are connected to the power supply, while the other rings are connected with voltage dividers to ring 1 and ring X and receive power this way. Moreover, ring X is responsible for depletion as well, together with the back contact. For ring 1, expected values are $-15\,\text{V} \leq V_{\text{R1}} \leq -5\,\text{V}$, for ring X $-150\,\text{V} \leq V_{\text{RX}} \leq -100\,\text{V}$.

V_{SSS} and V_{D}

Those are the supply voltages for the JFET. V_{SSS} is responsible for the JFET source currents and the bias current V_{D} sets the voltage for the JFET drain [46]. Commonly, $V_{\text{SSS}} = -3.9\,\text{V}$ and $V_{\text{D}} = -7.4\,\text{V}$ are used.

V_{IO}

This is the supply voltage for the ETTORE ASICs as well as for other components on the ASIC board. A value of $V_{\text{IO}} = 3.9\,\text{V}$ is used for the TRISTAN detectors.

V_{ResH} and V_{ResL}

The TRISTAN detectors are operated in a pulsed-reset mode. In this mode, external electronics are used to initiate a reset diode. The Res_{H} and Res_{L} voltages determine when the diode is in reverse-biasing or in forward biasing. To discharge the anode and initiate the reset, the voltage V_{ResH} is applied to the anode. To prevent the reset in between the rectangular reset pulses, the voltage V_{ResL} is applied to the anode reset diode. Commonly, $V_{\text{ResH}} = 4.0\,\text{V}$ and $V_{\text{ResL}} = 10\,\text{V}$ are used.

3.3 Entrance Window

The entrance window is the source-facing side of the SDD, where the incoming particle will hit first. Especially for particles with low penetration depth, it is crucial that the detection efficiency is as high as possible even close to the surface of the

SDD. However, a layer with reduced detection efficiency, also called dead-layer, is inevitable. This is due to the depth of the p^+ doping, which can alter the electric potential close to the surface in such a way that electrons can be guided away from the anode rather than towards it.

Additionally, a silicon dioxide layer is always present on top of silicon detectors. This is due to the oxidation of silicon when exposed to air. In this layer, the detector can be regarded as completely insensitive to incoming radiation. There, created charge carriers, i.e. secondary electrons and holes, can recombine with for example defects. Therefore, those are not detectable anymore. To ensure a homogeneous and as thin as possible silicon dioxide layer, this is grown artificially on the detector [41, 47].

The effective entrance window therefore consists of an insensitive silicon dioxide layer and a region with reduced sensitivity where not all charges can be collected, but not all charges are lost. For TRISTAN detectors, typical thicknesses of the effective entrance window are $d \approx 50\,\mathrm{nm}$ [41].

A thin effective entrance window is crucial for the TRISTAN experiment, as measurements with electrons will be performed in the final setup. While photons are able to penetrate matter deeply and interact in point-like interactions, electrons lose their energy quickly and continuously in matter. Therefore, electrons are likely to ionise secondary electrons close to the surface within the effective entrance window. The thicker the effective entrance window, the more secondary electrons are created inside it and therefore not detected. This leads to a shift of the detected electron energy towards lower energies. The entrance window effect, which is illustrated in figure 3.9 is in general negligible for photons, but very important for electrons.
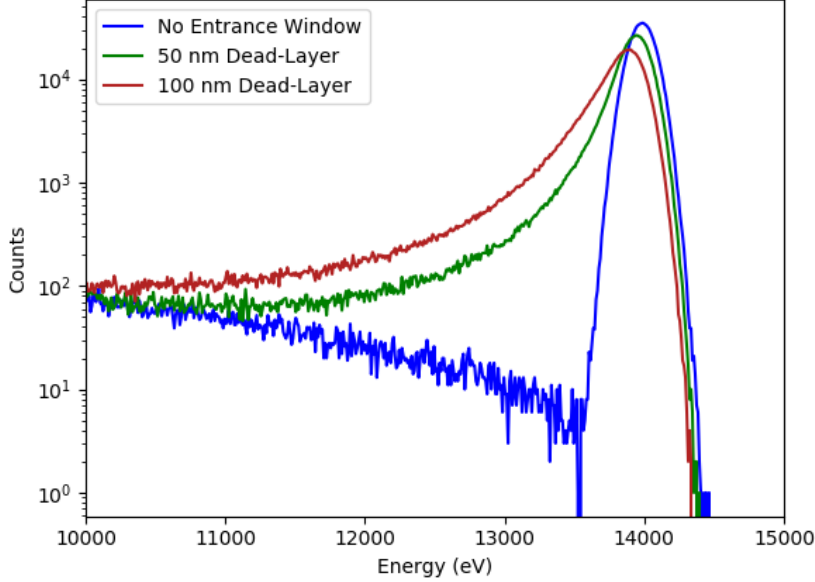
Figure 3.9: Effect of the effective dead-layer on the electron spectrum for $14\,\mathrm{keV}$ electrons. A higher effective dead-layer leads to a higher shift of the maximal energy and a broadening of the peak towards lower energies. Figure taken from [41].

3.4 Noise Theory

An excellent energy resolution is crucial for the search of keV-scale sterile neutrinos in KATRIN with the TRISTAN detector. It is usually given in terms of the Full Width at Half Maximum (FWHM) of a peak. For gaussian peaks, the FWHM is dependent on the variance σ of the peak:

$$\Delta E_{\mathrm{FWHM}} = 2\sqrt{2\log(2)} \cdot \sigma. \tag{3.1}$$

The variance of the peak is generally dependent on the Fano component σ_{Fano} and the electronic component σ_{el}:

$$\sigma = \sqrt{\sigma_{\mathrm{Fano}}^2 + \sigma_{\mathrm{el}}^2}. \tag{3.2}$$

To improve the energy resolution, the noise of the measurement system has to be minimised. There are several noise components that contribute to the total noise of the detector, which will be briefly discussed in the following.

3.4.1 Fano Limit

In semiconductor detectors, ionising particles create electron-hole pairs mostly via ionisation. The number of electron-hole pairs created is dependent on the energy E of the incident particle and the electron-hole pair creation energy E_{pair}. However, fluctuations in the size of the charge cloud and the number of created charge carriers are unavoidable. These fluctuations are described by the Fano factor, which depends on the material and the temperature. At room temperature, a Fano factor of $F = 0.118$ was found for silicon semiconductors [42]. This effect in the charge production process leads to a broadening of spectral lines of

$$\sigma_{\mathrm{Fano}}^2 = F \cdot E \cdot E_{\mathrm{pair}}. \tag{3.3}$$

This contribution to the broadening of peaks cannot be avoided or reduced and thus limits the final energy resolution of the detector.

3.4.2 Noise in a Charge Sensitive Pre-Amplifier

The main reducible contribution to the energy resolution is the electronic noise. In general, three main noise contributions are considered: the shot noise, which describes the influence of statistical fluctuations of the number of charge carrier at a given node, the 1/f-noise, and the thermal noise, which takes into account the velocity fluctuations of charge carriers in resistors. The thermal noise is dependent on the temperature T, the resistance R and the Boltzmann constant k_{B}. The main contribution to the shot noise in the TRISTAN detector is the leakage current I of the pn-junction [48].

With the input power spectral densities of the different noise contributions, a total output noise power density can be calculated for a charge sensitive pre-amplifier. For the TRISTAN detector system, these are shot noise from the detector leakage current, the JFET thermal and 1/f noise and the thermal noise from the current source. This results in an output noise power [49–51] of

$$W_{\mathrm{out}}(f) = \underbrace{\frac{2eI}{(2\pi)^2 f^2}}_{\text{current noise}} + \underbrace{C^2 \cdot \frac{A_{\mathrm{f}}}{f}}_{\frac{1}{f}-\text{noise}} + \underbrace{4C^2 k_{\mathrm{B}} T \cdot \left(\frac{a_{\mathrm{n}}}{g_{\mathrm{m}}} + \frac{1}{g_{\mathrm{m}}^2 R} \right)}_{\text{voltage noise}}. \tag{3.4}$$

The output noise power is dependent on the transconductance g_{m}, which describes the ratio of the outgoing current to the incoming voltage, a device-specific 1/f-coefficient A_{f}, the coefficient $a = 2/3$ for FETs and the capacitance C of the anode. Thus, a smaller anode with a smaller capacitance reduces the noise significantly.

Complimentary to noise investigations in the frequency domain, it is also possible

to transform the noise power into the time domain via a Fourier transform [49–51]:

$$W_{\text{out}}(\tau) = \underbrace{\frac{A_1 \cdot 2eI \cdot \tau}{(2\pi)^2}}_{\text{current noise}} + \underbrace{A_2 \cdot C^2 \cdot A_{\text{f}}}_{\frac{1}{\text{f}}-\text{noise}} + \underbrace{A_3 \cdot 4C^2 k_{\text{B}} T \cdot \left(\frac{a_{\text{n}}}{g_{\text{m}}} + \frac{1}{g_{\text{m}^2} R} \right) \cdot \frac{1}{\tau}}_{\text{voltage noise}} . \quad (3.5)$$

The coefficients A_1, A_2 and A_3 are pulse shaper-specific and can be calculated by integrating over the squared response function of the pulse shaper.

The noise power is typically expressed in ENC^2, which describes the amount of charge that would reproduce the signal made by noise [51]:

$$\text{ENC} = \frac{\sigma_{\text{noise}}}{E_{\text{pair}}} . \quad (3.6)$$

Chapter 4

166-Pixel TRISTAN Detector Module

To search for keV-scale sterile neutrinos with the KATRIN experiment, the current focal plane detector has to be replaced. To this end, the TRISTAN detector has been developed. In the first phase, it will consist of 9 modules each having 166 pixels. In a potential upgrade, 21 identical modules with a total number of about 3500 pixels will be used. In this chapter, the 166 pixel detector modules will be explained in more detail, starting with the module design in section 4.1. In section 4.2, the delicate assembly procedure of the 3D module is described. Although this thesis will focus on the 166 pixel detector modules, it is also applicable for the predecessor, a module consisting of 47 pixels.

4.1 Module Design

For characterising and understanding the technology, 7 pixel detectors were developed. Those detectors were assembled in a planar design: The SDD was fixed parallel to the PCB with the readout electronics. However, in the first phase, 9 modules will be used together as a detector in the KATRIN beamline. For 9 modules to be operated together, a three-dimensional design for the individual modules has to be applied, where the SDD is positioned in a 90° angle with respect to the readout electronics.

The design of a 166-pixel 3D detector module can be seen in figure 4.1. The base consists of a CESIC block mounted on a copper block which is connected to the cooling structure. The copper block acts as a carrier for the in-vacuum electronics, namely the two ASIC boards on either side of the copper block, while the SDD is attached to the CESIC block. Copper is used due to its good thermal conductivity of $386\,\mathrm{W/m/K}$ at $20\,°\mathrm{C}$ and $1\,\mathrm{mbar}$ [52]. To improve the energy resolution, the detector has to be cooled down, which is achieved by a chiller. The cooling power from the chiller is transferred through the copper block to both the ASIC boards and via the CESIC block to the SDD. CESIC is a carbon fiber reinforced silicon carbide, and is used due to its thermal and mechanical properties. It matches the thermal expansion coefficient of silicon, reducing the stress on the SDD when cooling down the detector.
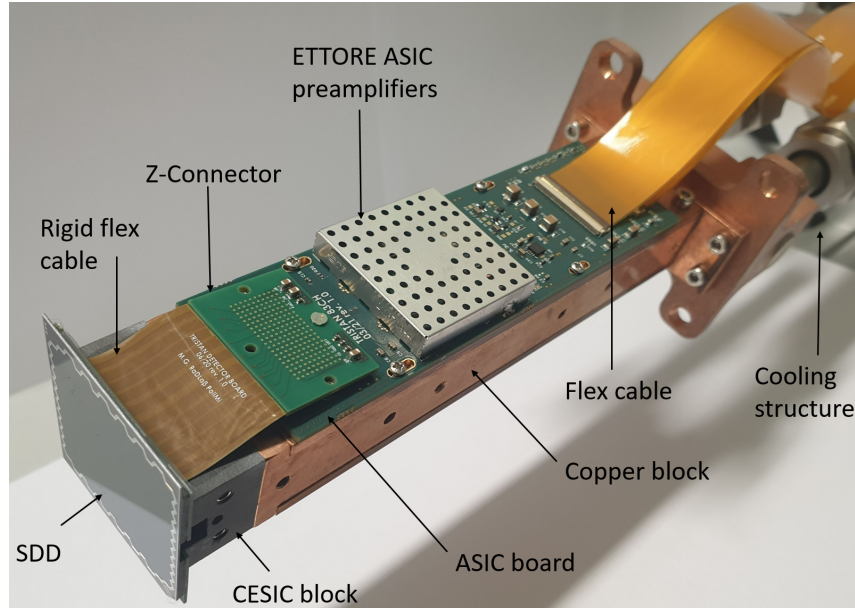
Figure 4.1: 166-pixel TRISTAN detector module. On the left, the SDD is visible, which sits on a CESIC block mounted on a copper block. Bond wires connect the SDD to the rigid-flex cable which is then connected via a Z-connector to the ASIC board. The setup on the bottom side of the copper block is identical. On the ASIC board sit the seven ETTORE ASICS, protected by a metal cap. The signal is transported via flex cables outside the vacuum for further readout.

If the SDD was mounted directly on the copper block and cooled down, the SDD could potentially be damaged by the expansion of the copper block. Therefore, a material is needed which has a similar thermal expansion coefficient to silicon and can be put in between the SDD and the copper block. In theory, a silicon block could also be used as a mount for the SDD. However, compared to silicon, CESIC has better mechanical strength, which is why CESIC is chosen as the SDD carrier.

To transfer the signals from the detector to the DAQ and the voltages from the bias board to the SDD, many connections are required. Due to space constraints, the electronics have to be manufactured and assembled in a very compact manner and special components are needed. Aluminium wire bonds connect the SDD with the rigid flex cables. With those cables, a 90° connection from the SDD to the ASIC board is made. A Z-connector, which is located at the base of the ASIC board between the rigid flex cable and the ASIC board, connects the ASIC board with the rigid flex cable. The ASIC board is the carrier for the in-vacuum readout electronics and contains 7 ETTORE ASIC pre-amplifier [45]. Each ETTORE ASIC amplifies

12 detector channels. The signals are then transferred with flex cables outside the vacuum to the bias system.

4.2 Assembly of the Detector Module

The 3D column shaped design of the module, where the SDD is glued to a carrier block, requires a specific assembly procedure. For this, a dedicated assembly jig was designed. As a material for the jig, the thermoplastic polymer PEEK is chosen. It features optimal thermal, chemical and mechanical properties. On the one hand, it can withstand the necessary temperatures during the hardening of the glue and is unaffected by chemical substances such as the glue itself. On the other hand, it is both soft enough to mitigate the possibility of damaging the SDD due to surface roughness in the jig and hard enough to provide enough support during the bonding process.

The module assembly is a very delicate procedure. During the assembly the SDD is handled without a protective coating and is therefore prone to damages due to particle deposits on the sensitive region of the SDD. Preventing particles from falling onto the sensitive region of the SDD or between the CESIC block and the SDD is therefore crucial [53]. For this reason, the assembly is carried out in a clean room at the Halbleiterlabor of the Max-Planck Gesellschaft.

Gluing step I: Rigid flex cables to CESIC block
The first gluing step is shown in figure 4.2. First, all components have to be cleaned with acetone, isopropanol and distilled water and dried with nitrogen.

The CESIC block is inserted into the PEEK jig. The side of the CESIC block where the SDD will be glued on is facing down. Afterwards, a thin line of glue is applied to the rigid flex cables and they are gently pressed to the side of the CESIC block. The PEEK jig is designed in such a way that aluminum bridges can be installed above the sides of the CESIC where now the rigid flex cables are glued to. They keep the rigid flex cables in place while the glue hardens in an oven at $60\,°C$ for $5.5\,h$.

Gluing step II: SDD to CESIC block
After the rigid flex cables have been glued to the CESIC block, they are again cleaned alongside with the SDD and the PEEK jig. This is done with acetone, isopropanol and distilled water to reduce the risk of residual glue or particles interfering with the assembly procedure.

The second step is to glue the SDD on the CESIC block. The SDD is carefully placed into the PEEK jig with the sensitive entrance window side facing downwards.
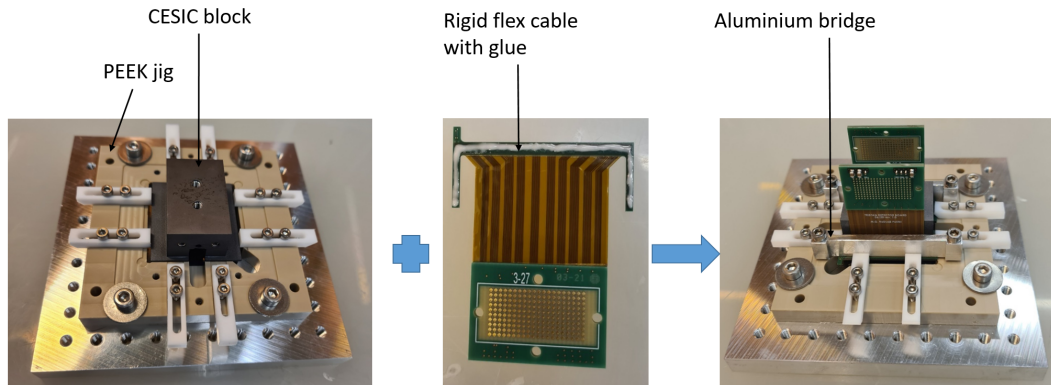
Figure 4.2: First step of gluing: Gluing the rigid flex cables to the CESIC block. Left: The CESIC block is placed in the PEEK jig. Middle: The glue is applied to the rigid flex cables. Right: The rigid flex cables are placed on the sides of the CESIC block and held down in place by aluminium bridges. Afterwards, the glue is hardened in an oven.
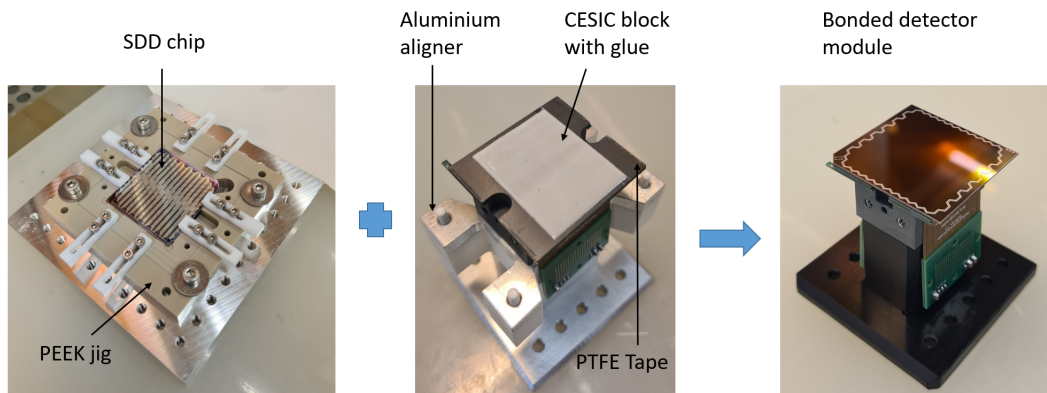
Figure 4.3: Second step of gluing: Gluing the SDD to the CESIC block. Left: The SDD is placed in the PEEK jig with the sensitive entrance window side facing downwards. Only the insensitive edges are touching the jig. Middle: Glue is applied to the center of the CESIC block. The CESIC block is placed in the aluminium mounter and lowered onto the SDD. Afterwards, the glue is hardened in an oven. Right: After the bonding, the new detector module is ready for tests.

The SDD can only touch the jig at the edges in the non-sensitive volume. If the sensitive volume touches the jig or anything else, the detector might be damaged.

After placing the SDD in the jig, the ring X wire bonds are set, as the bond pads become inaccessible during the assembly process. Afterwards, glue is applied to the CESIC block. To ensure an even glue thickness and to avoid spilling the glue over the edges of the CESIC block and the SDD, 190 µm thick PTFE tape is put on the edges of the CESIC block before the glue is applied. This also helps preventing damages to the SDD, as it prevents possible small particles between the CESIC block and the SDD to be pressed onto the surface of the SDD. This is described in more detail in [53]. The CESIC block is then put onto the SDD with the help of aluminium mounters and the glue is hardened in an oven. This step of the assembly procedure is illustrated in figure 4.3.

The first attempts of gluing the SDD onto the CESIC block were performed using a glue containing small spacer balls. The intention was to have a defined distance between the surfaces. These spacers, however, damaged many pixels of the SDD, resulting in not completely functioning detectors. Therefore, EPOTEK920FL without spacer balls is now used as a glue. The PTFE tape ensures a defined distance of SDD to CESIC block. With this glue and this procedure, several well-working detector modules have been build.

The detector has to be bonded after the glue is hardened, which is done with aluminium bond wires. This completes the assembly procedure. The detector can finally be mounted on a module block with the ASIC boards and is ready for testing.

Chapter 5

Experimental Setups

For the commissioning and tests of the 166-pixel TRISTAN detector modules, two different setups were used. In section 5.1, the Data Acquisition System used in both setups is discussed in detail. The first setup, a dedicated laboratory setup for the first commissioning of the detector modules, is described in section 5.2. For the measurements with electrons in a realistic MAC-E filter environment, the KATRIN Monitor Spectrometer is used, which is discussed in section 5.3.

5.1 Data Acquisition System

The collected charge from the detector is readout via a charge sensitive preamplifier. Two different outputs can be selected. For the first stage, ramp-like waveforms are obtained. A second stage is generated by an AC-coupling and provides the signal with an exponential decay. While the waveform can be used for a first check of the functionality of the detector and can also be analysed offline, a more efficient way to do so is via the use of a Data Acquisition System (DAQ). A DAQ can process the raw waveforms and process the information into more convenient data modes, for example histograms of events. Two DAQs that meet the requirements for the 166-pixel TRISTAN detector are the CAEN DAQ and the Athena DAQ. The CAEN DAQ system consists of three synchronised CAEN VX2470B cards, while the Athena DAQ is a custom-made DAQ developed and produced by Politecnico di Milano [54]. Both DAQs will be discussed in the following.

5.1.1 Athena DAQ System

One investigated option is the custom-made Athena system, which was designed and manufactured by Politecnico di Milano [54]. In contrast to the CAEN DAQ, it is an analogue pulse processor (APP) and was specifically developed for the 166-pixel TRISTAN detector module.
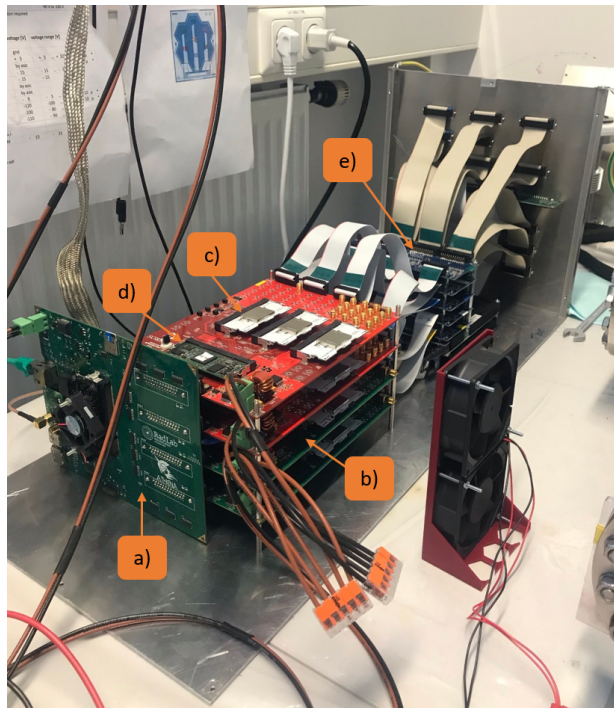
Figure 5.1: Athena DAQ system. The Athena data aggregator platform (a) distributes the global trigger and handles the processed events. It is responsible for the four Kerberos modules (b), which handle the event processing. Each Kerberos module consists of three SFERA ASICs (c) and one FPGA (d). Each SFERA ASIC takes a maximal input of 16 detector channels and processes the waveform input. The FPGA is used for signal regulation and external communication. The signals are transferred from the detector to the bias system (e) and then to the Athena DAQ system.

5.1.1.1 Working Principle of Athena System

For the following explanation of the working principle of the Athena system, [54] is used as a general reference, if not stated otherwise. The Athena system consists of two main components: Four Kerberos modules, which handle the event processing, and the Athena data concentrator platform, which is responsible for the global trigger and the handling of the processed events. A picture of the Athena system is shown in figure 5.1.

Kerberos modules
Each Kerberos module consists of three analogue pulse processors, the SFERA

ASICs, and one Field Programmable Gate Array (FPGA). The SFERA ASICs are interchangeable in the three SFERA slots. One SFERA ASIC takes a maximum of 16 channels as an input, therefore, one Kerberos module can handle up to 48 detector channels. The SFERA ASICs process the waveform input with two semi-Gaussian shapers of 9th order. The first acts as a fast filter to detect events over a threshold and rejects pile-up, while the second one is responsible for the event energy reconstruction. The processed signals are then digitised by three onboard Analogue-to-Digital-Converters (ADC). Prior to the acquisition of data, the SFERA ASICs have to be programmed via the Graphical User Interface (GUI) with the desired parameters, such as the peaking time. The FPGA is used for the management of the digital signals as well as for the communication with the Athena aggregator.

Athena data concentrator platform
The Athena data concentrator platform, which will be referred to as Athena in the following, can handle up to four Kerberos modules, making the Athena system suitable for the readout of up to 192 detector channels simultaneously. It acts as an event builder for the Kerberos modules. Once one Kerberos module detects an event, Athena is notified and distributes a global trigger to all Kerberos modules. This means, that all channels across all Kerberos modules are read out simultaneously if one channel triggers. A complete map of the detector at the time of the event is therefore saved. This is especially useful for e.g. charge sharing and cross talk investigations.

5.1.1.2 Characterisation of the Athena System with a Pulse Generator

In a first step, the Athena DAQ system was thoroughly characterised with a pulse generator, i.e. no detector was connected to the DAQ. To this end, voltage signals were directly injected from a pulse generator into the Athena system. The signal consists of 20 pulses with amplitudes in the range of $2-40\,\text{mV}$ in $2\,\text{mV}$ steps and is illustrated in figure 5.2. Since voltage steps with different amplitudes correspond to events with different energies, this signal is expected to lead to 20 monoenergetic and equidistant peaks with the same height. Because no detector is connected, almost no noise is expected to lead to a broadening of the Gaussian peaks.

All 16 channels belonging to one SFERA ASIC show the same behaviour. If unphysical features appear on pulse spectra, they appear on the spectrum of all 16 channels. If the spectrum of one channel is clean, the spectra of all 16 channels are clean. Therefore, in the following analysis, the 16 channels belonging to one SFERA slot will be called a channel group and only one exemplary spectrum is shown to describe the whole channel group. An exemplary, clean pulse spectrum for one channel is shown in figure 5.3. Out of twelve channel groups, eight channel groups show this desirable behaviour.
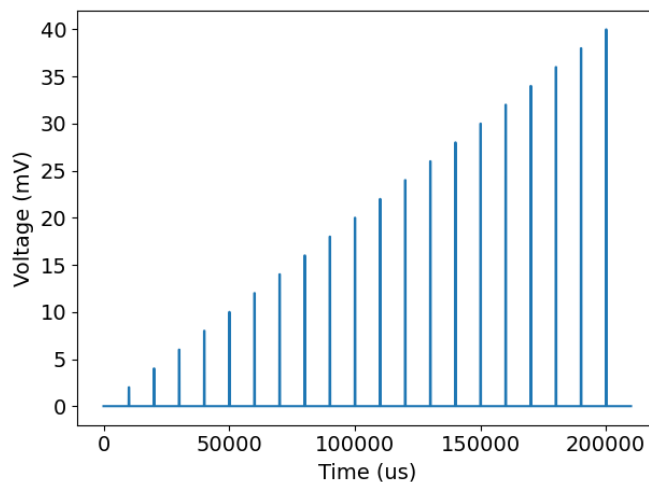
Figure 5.2: Pulse generator signal used for the characterisation of the Athena DAQ system without a detector. 20 pulses with amplitudes ranging from $2-40\,\text{mV}$ in $2\,\text{mV}$ steps are used.

Three channel groups show a very broad null peak, but have otherwise clean spectra. These three channel groups do not change their behaviour when the measurement is repeated with different SFERA ASICs, but are always located on one specific Kerberos module. Therefore, this issue can be most likely attributed to a problem with the Kerberos module itself rather than on the SFERA ASICs. One channel group exhibits an abnormal behaviour in the center of the spectrum. There, multiple smaller peaks seem to be superimposed on an otherwise clean spectrum, and the amplitude of the peaks at the highest ADC values is reduced for several peaks. The resulting spectrum is illustrated in figure 5.4. The number of events in the peaks with the reduced height is equal to the number of expected events if the number of events superimposed on the normal spectrum is added. Therefore, this might be attributed to a problem with correctly associating the event energies. This problem is limited to one specific channel group on a Kerberos module with one specific FPGA. Therefore, the problem is likely caused by a malfunctioning FPGA.

Other problems that appeared while testing the Athena system were programming problems of the SFERA ASICs and connection problems of the whole Athena system. As described above, the SFERA ASICs have to be programmed with the desired parameters. However, occasionally, unknown problems prevented the SFERA ASICs from being programmed. In addition, the Athena system was prone to losing the network connection with the computer, especially during long-time measurements. Unfortunately, none of the described problems could be solved.
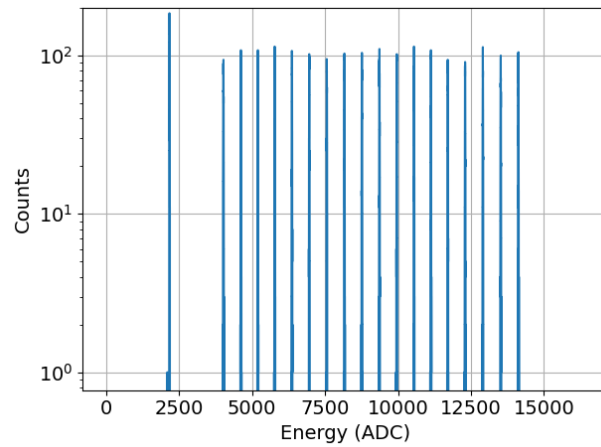
Figure 5.3: Exemplary, clean spectrum of the Athena pulse analysis for one channel. The first peak at the lowest ADC values is the null peak. It corresponds to the case where the energy filter is evaluated on the baseline of the waveform instead of an event. As each channel is read out whenever one channel triggers, this null peak is expected to be large. The other 18 peaks are equidistant and of Gaussian shape. The number of events in the narrow Gaussian peaks is equal for each peak. Two peaks fall under the detection threshold.
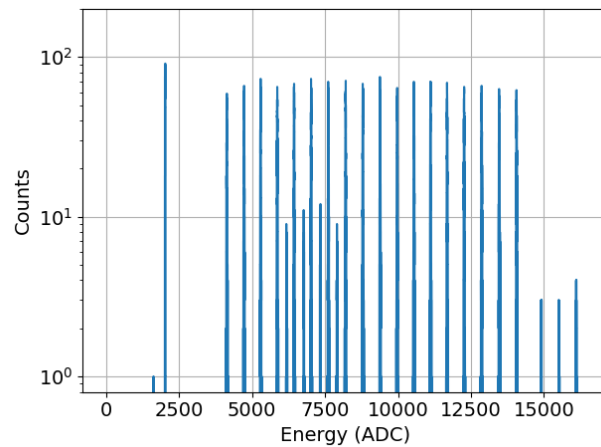
Figure 5.4: Pulse analysis spectrum acquired with the Athena DAQ of a channel in the channel group affected by the malfunctioning FPGA. The underlying clean spectrum is distorted by smaller peaks in the center region. In addition, the peaks at high ADC values have a reduced amplitude and consequently number of counts per peak.

5.1.2 CAEN DAQ

The second investigated DAQ option is the CAEN DAQ. For the characterisation measurements of one TRISTAN 166-pixel detector module, three VX2470B cards were used. Each card is a Digital Pulse Processor (DPP) and is capable of acquiring 64 channels. The three cards are synchronised and can convert the information on the waveforms into different data formats:

Spectrum data

In the spectrum acquisition mode, only the histogram of the ADC bin amplitudes is saved, therefore only energy spectra can be reconstructed. Spectrum data is convenient for fast first analyses and requires the least amount of disk space.

Listmode data

In the listmode acquisition mode, the histogram of the ADC bin amplitudes as well as the timestamp of all events are saved. This way, detector related effects such as charge sharing between pixels can be investigated.

Listwave data

In the listwave acquisition mode, a snippet of the waveform with the detected event is saved, along with time information and the event energy in ADC. This requires the most disk space but also contains the most information for offline analysis. With listwave data, noise investigations can be conducted, e.g. noise curves.

Waveform data

In the waveform acquisition mode, raw waveform data is saved. If the first stage waveforms are saved, noise analyses such as noise spectral density investigations can be performed.

To extract the energy of the event from the waveform, the CAEN DAQ uses a trapezoidal filter. The working principle of such a filter is illustrated in figure 5.5. The waveform is averaged in two windows which are separated by the gap time t_{gap}. Both windows have the length of one peaking time t_{peak}. The gap time has to be at least as long as the signal rise time for the trapezoidal filter to function properly. The averaged values of the two windows are then subtracted from each other, leading to a characteristic trapezoidal filter response. The event energy can then be read out as the height of the flat top of the trapezoidal filter output.

(a) Scheme of shaping and gap time.

(b) Waveform with resulting trapezoid.
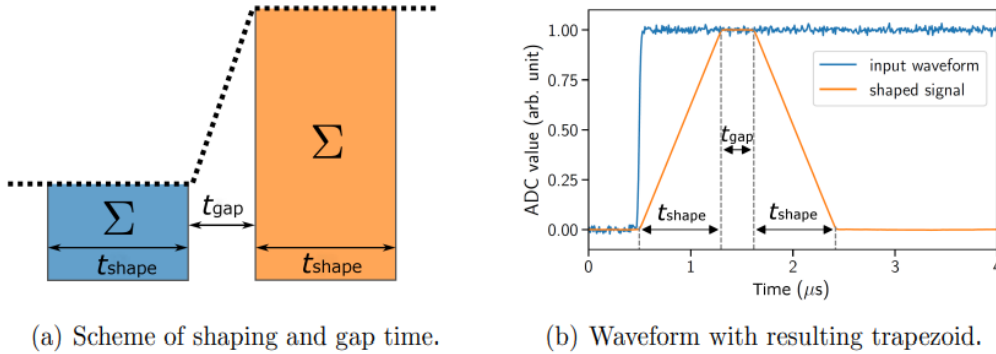
Figure 5.5: Left: Working principle of a trapezoidal filter. The black points represent the waveform. The waveform is averaged in two windows with length t_{shape}. The two windows are separated by the gap time t_{gap}. The values of the averaged windows are then subtracted from each other. Right: Trapezoidal filter output (orange) for a step waveform (blue). The height of the flat top of the trapezoidal filter output corresponds to the event energy. Figure taken from [55].

5.1.3 Comparison of the DAQ systems

In the next step, the two DAQ systems were compared to each other. For this, measurements with a 166-pixel TRISTAN detector were taken. For the Athena DAQ system, it was only possible to acquire energy spectra at temperatures below zero degree Celsius, as the system was not functional together with the detector at room temperature. With the CAEN DAQ system, it is possible to measure at room temperature. Both data sets were taken with an ^{55}Fe source using a dedicated test stand at MPP, which will be described in more detail in section 5.2. The system was cooled down to a temperature of $-50\,°\mathrm{C}$ on the chiller, which roughly translates to a temperature at the SDD of around $-29\,°\mathrm{C}$.

The comparison of two exemplary energy spectra can be seen in figure 5.6. With the CAEN DAQ, all pixels show physical and clean ^{55}Fe spectra. Beside the two main ^{55}Fe peaks at 5.9 keV and 6.4 keV, respectively, three smaller peaks are visible: A silicon escape peak from the main peak, located 1.74 keV beneath the main peak, and two setup-specific fluorescence peaks stemming from one of the materials in the setup. The two ^{55}Fe peaks are clearly separated, hinting at a good energy resolution. No distortions are visible in the spectra. For the spectra acquired with the Athena DAQ, not all pixels exhibit this desirable behaviour. Out of the 166 pixels, 129 pixels show a physical spectrum with comparable energy resolution to the spectra taken with the CAEN DAQ. However, the three peaks at smaller energies are shifted with respect to the spectra taken with the CAEN DAQ.
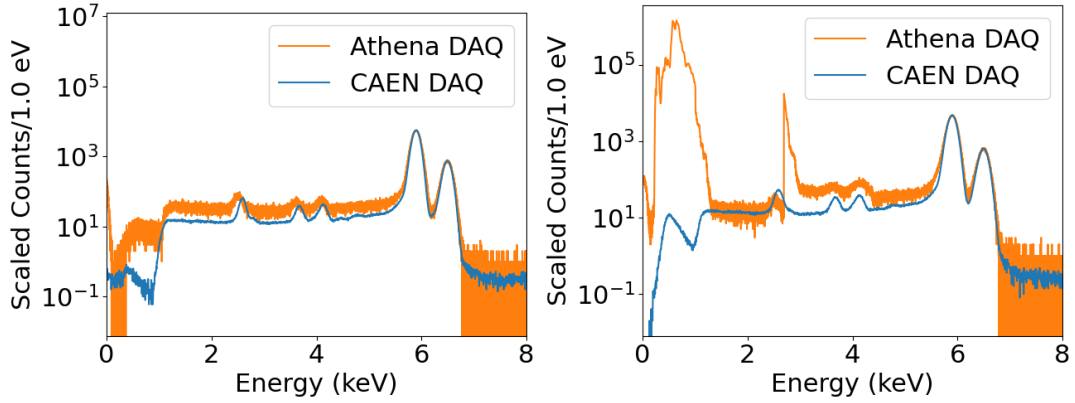
Figure 5.6: Comparison of the ^{55}Fe energy spectra taken with the Athena DAQ (orange) and the CAEN DAQ (blue) for two different pixels. For better comparability, both spectra are scaled to the height of the Mn-K$_\alpha$-peak. Left: Both DAQs show a physical ^{55}Fe spectrum with comparable energy resolution. However, the spectrum acquired with the Athena system seems to have a higher backscattering tail. In addition, the silicon escape peak and the two fluorescence peaks of the material in the setup, are shifted compared to the CAEN spectrum. The origin of the shift is not clear. Right: The Athena spectrum has a very broad null peak that extends into the low-energy part of the spectrum. Between $2.5-4.5$ keV, a non-physical distortion is present, which is the result of the FPGA problem.

Furthermore, the backscattering tail is more pronounced than in the spectra acquired with the Athena DAQ. In addition, a broad null peak is observed in 35 pixels, that partially extends into the spectrum above the threshold. Of those pixels, 16 pixels also have a non-physical distortion in the spectrum, that is located approximately between $2.5-4.5$ keV. This correlates with the problems experienced in the pulse generator analysis and is likely due to the FPGA problem. Additionally, the spectra acquired with the Athena DAQ have less statistics compared to spectra taken with the CAEN DAQ with equal runtime. The Athena DAQ has a higher deadtime due to the readout of all detector channels every time one channel triggers.

In figure 5.7, a comparison of the energy resolution is shown for all pixels. The median energy resolution amounts to $\Delta E_{\text{FWHM, CAEN}} = 193$ eV for the CAEN DAQ and $\Delta E_{\text{FWHM, Athena}} = 210$ eV for the Athena DAQ, both at a peak energy of 5.9 keV. Both the median energy resolution and the energy resolution for almost all pixels are better when the data was acquired with the CAEN DAQ.
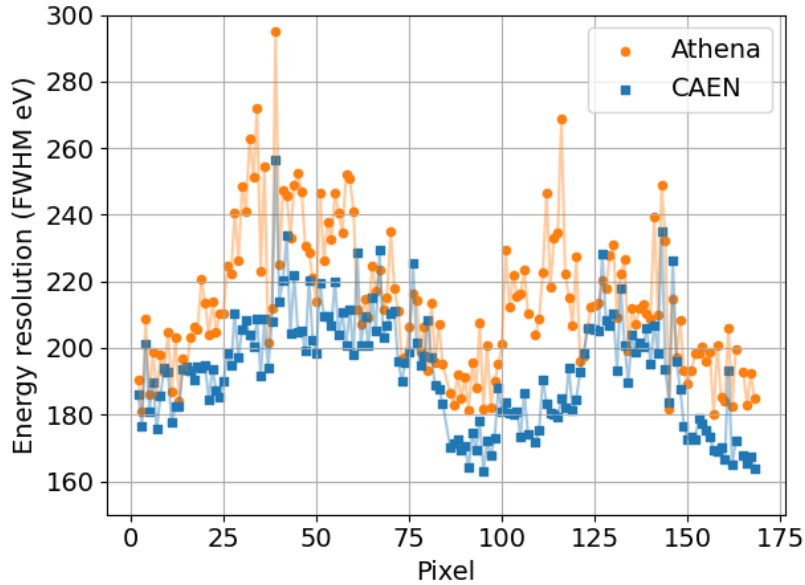
Figure 5.7: Comparison of the energy resolution of the Athena DAQ (orange) and the CAEN DAQ (blue) for individual pixels. For almost all pixels, the energy resolution of the CAEN DAQ is better than the one obtained with the Athena DAQ.

Due to the better energy resolution and reliability of the CAEN DAQ as well as the persisting spectral distortions and connection problems of the Athena DAQ, it was decided to use the CAEN DAQ for all subsequent measurements presented in the scope of this thesis.

5.2 Vacuum Cross Setup

The first characterisation measurements of the TRISTAN detector were carried out using a dedicated test setup (vacuum cross) at the Max-Planck Institute for Physics (MPP). This is shown in figure 5.8. Two pulse generators provide signals for the reset logic and inhibit. The signals are transferred from the detector to the bias system located in the bias board box and then to the CAEN DAQ where they are read out. The detector is mounted on the copper block and is connected to the cooling structure. A source holding structure for radioactive calibration sources can be mounted above the entrance window of the detector. The source is aligned with the center of the SDD. The detector is assembled in the vacuum cross.
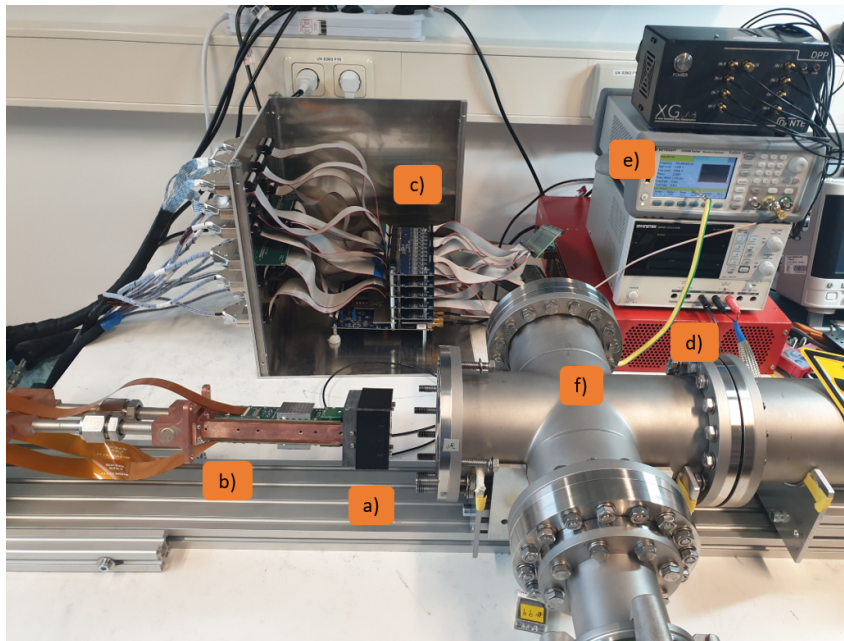
Figure 5.8: Experimental setup (vacuum cross) at the MPP to investigate the 166-pixel TRISTAN detector. The TRISTAN detector (a) with a custom-made holding structure is installed on the copper block (b) which is mounted on the cooling structure. The signals are transferred to the bias system (c) and further to the CAEN DAQ (d). The pulse generators (e) provide the reset and inhibit signals. The vacuum cross (f) is connected to a vacuum pump. Moreover, a chiller is connected to the cooling structure.

Two sources are available at the MPP, an ^{55}Fe source and an ^{241}Am source. For the measurements carried out in the scope of this thesis, the ^{55}Fe source was used.

5.3 KATRIN Monitor Spectrometer Setup

After initial commissioning measurements in the vacuum cross setup, it is important to test the detector modules in a realistic environment which closely resembles the KATRIN experiment. Since the neutrino mass measurements are still ongoing, the KATRIN Monitor Spectrometer (MoS) is chosen for this task.

5.3.1 Operating Principle

The MoS consists of the repurposed spectrometer of the former Mainz experiment, the predecessor of the KATRIN experiment.
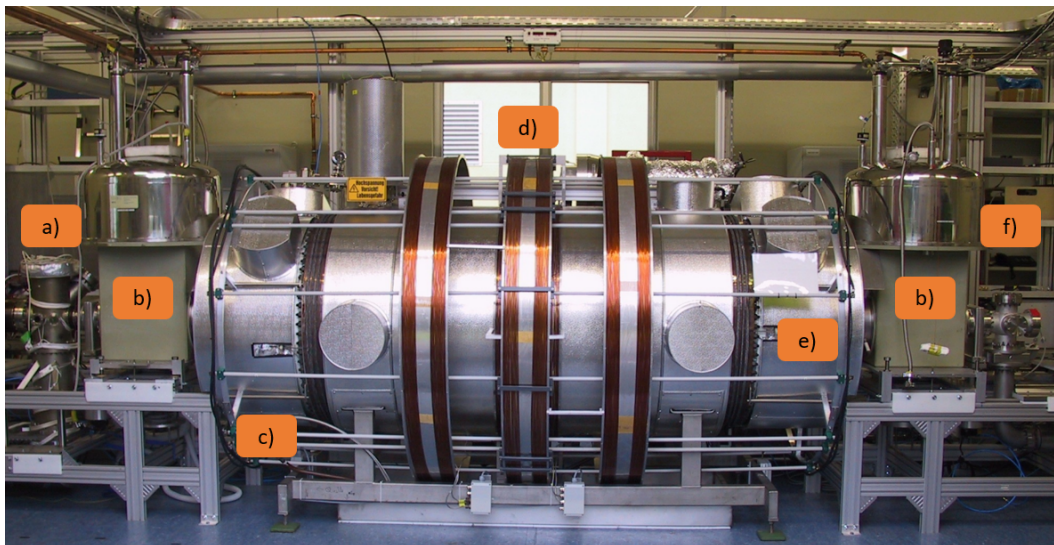
Figure 5.9: KATRIN Monitor Spectrometer. In the source section (a) up to four sources can be placed. Two superconducting magnets (b) create the magnetic field for the MAC-E filter. The EMCS (c) compensates the earth magnetic field while the LFCS (d) confines the magnetic lines inside the spectrometer tank (e). In the detector section (f), the 166-pixel TRISTAN detector module is installed. Picture taken from [56].

It is connected to the high voltage supply of the KATRIN main spectrometer and was initially supposed to monitor high voltage fluctuations. More recently, however, it serves as a test stand, e.g. for the 166-pixel detector module. A photograph of the MoS can be seen in figure 5.9. For the following sections, where the individual components of the MoS are described, [56] is used as a general reference if not stated otherwise.

Spectrometer

Just as the pre- and main spectrometer of the KATRIN experiment, the MoS also makes use of the MAC-E filter principle. It consists of a tank with a diameter of $1\,\mathrm{m}$ and a length of $3\,\mathrm{m}$. The tank is grounded. Inside the tank, a cylindrical electrode is located. Additionally, a wire electrode is inside the cylindrical electrode. High voltage can be applied to the cylindrical electrode and an additional $5\,\mathrm{kV}$ potential difference between the cylindrical and the wire electrode can be realised. The spectrometer has an energy resolution of $\Delta E = 0.92\,\mathrm{eV}$ at an electron energy of $17.8\,\mathrm{keV}$.
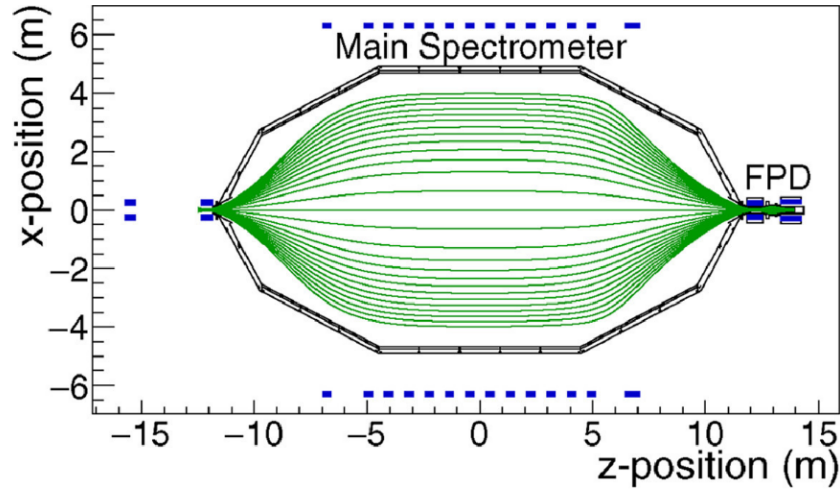
Figure 5.10: Magnetic field configuration for measurements of radiation originating in the source section of the KATRIN MoS. The magnetic field lines (green) are confined in the tank and do not touch the walls. Instead, they guide the electrons from the source section (left) to the detector section (right). Figure adapted from [57].

Vacuum System

To ensure that the electrons reach the detector, good vacuum conditions are required. A series of pumps create a vacuum of $2.1 \cdot 10^{-10}$ mbar inside the spectrometer. First, a scroll pump creates a pre-vacuum. The first Turbo Molecular Pump (TMP) improves the vacuum to intermediate values $< 10^{-5}$ mbar. Three additional TMPs, one each at the source section, the spectrometer and the detector, are needed to achieve the final vacuum. To minimise the outgassing of components installed inside the spectrometer that could worsen the vacuum, the spectrometer can be baked out at a temperature of 200 °C.

Magnetic System

Two superconducting magnets are used to create the magnetic field for the MAC-E filter. For operation, liquid helium cooling of the magnets is required to achieve a temperature of 4.2 K. Typical magnetic flux values of the magnets are on the order of 6 T at 50 A. A typical magnetic field configuration for measurements in the KATRIN spectrometer is shown in figure 5.10. This is applicable for the MoS as well.

Air Coil System

Two additional air coil systems, the Earth Magnetic Field Compensation System (EMCS) and the Low Field Compensation System (LFCS) are installed. The EMCS consists of horizontally-arranged white tube-like electrodes and compensates

the magnetic field of the Earth. Four additional air coils constitute the LFCS, which confines the magnetic field lines to the interior of the tank. This ensures that the electrons are guided in such a way that they do not hit the spectrometer walls.

Source section

In the source section, up to four sources can be installed. Since the tube is movable, movements in the axial and radial direction are possible. An electric potential of up to about 1 kV can be applied to the sources to shift the energy spectrum of the outgoing radiation as desired.

5.3.2 Photon and Electron Sources

Multiple sources can be used for measurements in the MoS, emitting both electrons or photons. While the characterisation with photons can be realised easily and reliably, the goal of this thesis is the characterisation of the detector module with electrons as this type of radiation will be detected in the final measurement configuration to search for keV-scale sterile neutrinos. In the following, the available sources in the MoS will be presented in more detail.

^{55}Fe

The isotope ^{55}Fe has a half-life of 2.7 years and decays via electron capture to ^{55}Mn. As listed in table 5.1, three emitted X-rays are of interest. Since the Mn-$K_{\alpha 1}$ and Mn-$K_{\alpha 2}$ lines are too close to each other in energy, they cannot be resolved. For this reason, they are considered as one Mn-K_α line with an energy of approximately 5.9 keV. The Mn-K_α and Mn-K_β lines, however, can be distinguished if the energy resolution of the detector is good enough. Therefore, those two lines can serve as a good first indicator of the energy resolution even by eye. A typical ^{55}Fe energy spectrum can be seen in figure 7.1.

Table 5.1: X-ray energies of the decay of ^{55}Fe suited for calibration measurements [58].

	Energy (keV)	Relative Probability
Mn-$K_{\alpha 1}$	5.898 75	0.51
Mn-$K_{\alpha 2}$	5.887 65	1
Mn-K_β	6.490 45	0.205

To be able to measure with ^{55}Fe in the MoS, a source holder attached to a calibration arm, which moves the source into the beamline, had to be designed and manufactured. The source holder is made of non-magnetic stainless steel and is mounted on the calibration arm. The calibration tools are shown in figure 5.11.

Figure 5.11: Left: Photograph of the custom-designed calibration arm and view port that is installed at one of the feedthrough ports of the MoS setup. The calibration arm can be extended into the beamline. Right: Source holder made out of non-magnetic stainless steel.

^{83m}Kr

In the MoS, the isomeric isotope ^{83m}Kr is used as the main source for measurements with beta electrons. It has a short half-life of 1.83 h and is produced via the decay of ^{83}Rb with an efficiency of 74 %. Rubidium in turn has a half-life of 86.2 d and is implemented on a Highly Oriented Pyrolithic Graphite (HOPG) substrate. There, it continuously decays to ^{83m}Kr which then decays via two gamma transitions [59]. The energies of the emitted gamma rays are listed in table 5.2. The decay scheme is shown in figure 5.12.

Table 5.2: Gammas emitted in the decay of ^{83m}Kr [59].

	Energy (keV)	Relative Probability
γ	9.4057	0.055
γ	32.1516	0.000 062

^{83m}Kr is convenient as a calibration and characterisation source for the KATRIN experiment in general and the MoS in particular. Via internal conversion, ^{83m}Kr is an electron source with various energies. In addition, another advantage of ^{83m}Kr is that the energy of the K32-line is very close to the energy of the tritium endpoint energy. The different conversion electron energies are listed in the appendix in table A.1 along with the internal conversion coefficient and the intensity per decay.

Figure 5.12: The decay scheme of ^{83}Rb and ^{83m}Kr. The nuclear levels are described by the half-life, the spin-parity, the energy of the transition in keV and the branching ratio. For the decay of ^{83}Rb, the intensity in % as well as the multipolarity and the energy in keV are given. Figure taken from [60], based on data from [61].

The Auger electrons with energies of 1.5 keV and 10.8 keV are omitted, since they are not of interest for the analysis in this thesis.

A typical conversion electron spectrum of ^{83m}Kr can be seen in figure 5.13. Most of the lines listed in table A.1 are too close to each other in energy to be resolved. Therefore, only seven separate peaks can be observed in an energy spectrum. The peak nomenclature, which is used in this thesis is based on the shell the electron is emitted from (K, L, M or N) and on the energy of the photon used in internal conversion (9.4 or 32 keV). In particular, the L32 and M32 peaks are of interest. In a real spectrum taken with an SDD, those are the cleanest peaks as they are least affected by detector effects, e.g. backscattering tails of other peaks.

Wall Electrons
The third source of radiation in the MoS are the walls of the spectrometer itself. Given a magnetic field configuration that "looks" at the wall, i.e. guides electrons from the wall to the detector, electrons of a selectable energy reach the detector. The energy of the peak of the electron spectrum is determined by the voltage applied to the spectrometer, as it accelerates the so called wall electrons towards the detector. The required magnetic field configuration is shown schematically in figure 5.14, using the example of the KATRIN main spectrometer. It is also applicable for the MoS.

Figure 5.13: Conversion electron spectrum of ^{83m}Kr. Most peaks consist of multiple individual peaks which are too close to each other to be resolved. Therefore, the summed intensities for lines originating from the same electron shell are shown. Figure taken from [60].
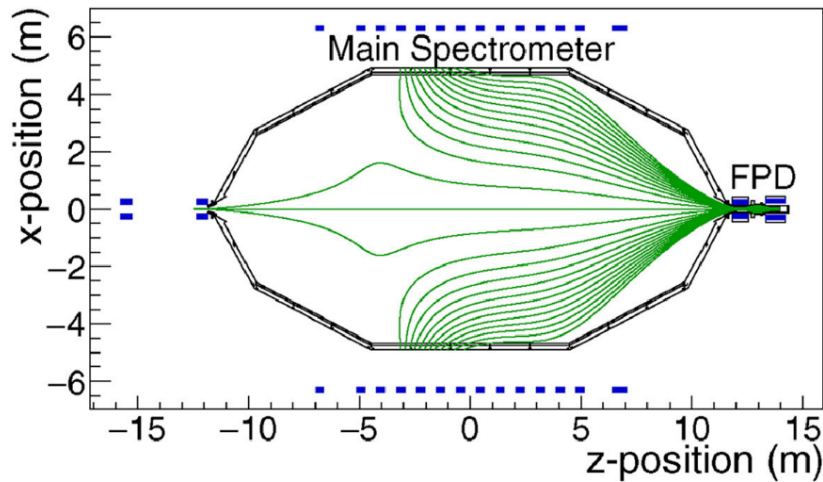
Figure 5.14: Magnetic field configuration for wall electron measurements at the KAT-RIN main spectrometer. This configuration is also applicable for the MoS. The magnetic field (green lines) guides electrons from the spectrometer walls to the detector. Some magnetic field lines also connect the source section with the detector, leading to a small contribution of source electrons in the center of the flux tube. Figure adapted from [57].

Two main processes create wall electrons: Cosmic muons and radioactive decays from materials inside the spectrometer walls or the building around the spectrometer. Cosmic muons are minimally ionizing particles. They continuously create secondary electrons while moving through matter. They pass the spectrometer walls twice and might also traverse components of the electrode system inside the spectrometer. There, secondary electrons with sufficient energy near the surface might escape from the material into the vacuum of the spectrometer and can finally reach the detector. The ionized electrons can initially have energies in the order of MeV. However, due to scattering and cascade processes, most emitted electrons have energies below $30\,\text{eV}$, with peak energies around $1-2\,\text{eV}$ [57, 62]. A second process for the creation of wall electrons are radioactive decays in the spectrometer material. In the stainless steel spectrometer, this is dominated by beta-decays of the isotopes ^{60}Co, ^{137}Cs and ^{40}K. Furthermore, thorium and uranium decay in the concrete of the MoS hall. They emit gamma rays, which can emit electrons from the material in the spectrometer wall via the Compton effect or the photo effect [62].

In the scope of this thesis, wall electrons in the range from $5\,\text{keV}$ to about $32\,\text{keV}$ were measured.

5.3.3 Detector Installation in the MoS

The installation of the 166-pixel TRISTAN detector module in the KATRIN MoS was performed in September 2022. For the readout of the detector, the CAEN DAQ, see section 5.1, as well as the bias system were set up in the MoS hall. This setup is shown in figure 5.15. Two pulse generators supply the detector with the reset signal and the inhibit signal.

The detector itself is mounted on the cooling structure. The cooling structure is movable and allows for movements in x, y and z direction. A protective cap is mounted above the detector, letting the SDD exposed, see figure 5.16. This cap was originally designed to reduce potential outgassing of the readout electronics into the spectrometer vacuum. To this end, a ring was installed in the cross facing the spectrometer. The cap fits into the ring, sealing the spectrometer with respect to the ASIC boards. Recently, however, the cap is mainly used as an additional protection for the SDD. The ring is not installed anymore, as no significant improvement of the vacuum in this configuration was observed. A chiller is connected to the cooling structure and can cool the SDD down to $-29\,°\text{C}$.
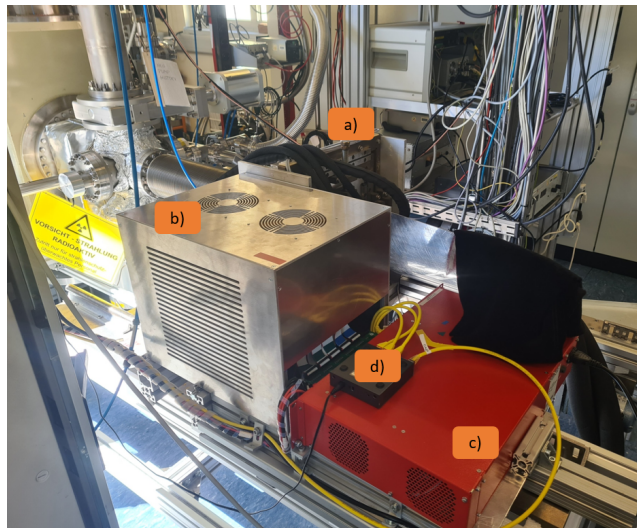
Figure 5.15: Bias system and CAEN DAQ in the MoS hall. Cables (a) transfer the acquired signals from the detector to the bias system (b) which amplifies the signals and transfers them to the CAEN DAQ (c). The DAQ is connected via an ethernet connection (d) to the computer.

Figure 5.16: Left: Detector mounted on the cooling structure. The cooling structure is movable and allows for movements in x, y and z direction. Right: 166-pixel TRISTAN detector with protective cap on. The SDD is exposed, the cap was originally designed to protect the vacuum from outgassing of the readout electronics.

5.4 Electron Response Function

While photon peaks are typically fitted with either a simple Gaussian function or a Gaussian function with a shelf term, the detector response to electrons is more complicated. Thus, for a precise analysis, a more complex model is needed. For the analysis carried out in this thesis, an empirical electron response model was used to fit electron peaks. The electron response function takes into account the dead layer effect of the detector when measuring electrons, leading to a low-energy shoulder of the main peak. Moreover, the backscattering tail is included. The base of the response function is still a Gaussian function f_{Gauss} with mean μ, variance σ^2 and amplitude A:

$$f_{\text{Gauss}} = A \cdot \exp\left(-\frac{(x-\mu)^2}{2\sigma^2}\right). \tag{5.1}$$

Next, a diffusion term f_{Diff} is added, which takes the parameters A, μ and σ from a previous Gaussian function as well as the the ratio r of the diffusion part and the main peak, and β, which determines the steepness of the shoulder of the main peak:

$$f_{\text{Diff}} = A \cdot r \cdot \exp\left(\frac{x-\mu}{\beta}\right) \cdot \left(1 - \text{erf}\left(\frac{x-\mu}{\sqrt{2}\sigma} + \frac{\sigma}{\sqrt{2}\beta}\right)\right). \tag{5.2}$$

The backscattering part $f_{\text{Backscatter}}$ of the spectrum is included in the model taking into account the ratio between backscattering tail and main peak r_{back} and the parameters a, b and c. Here, a defines the threshold of the fitting region of the backscattering tail, while b and c are responsible for the shape of the backscattering tail:

$$f_{\text{Backscatter}} = A \cdot r_{\text{back}} \cdot \left(\frac{x-a}{\mu}\right)^b \cdot \left(1 - \frac{x}{\mu}\right)^c. \tag{5.3}$$

After fitting the individual components and extracting the fit parameters, a combined fit is conducted for the final electron response:

$$f_{\text{ElectronResponse}} = f_{\text{Gauss}} + f_{\text{Diff}} + f_{\text{Backscatter}} \tag{5.4}$$

Chapter 6

Optimal Detector Working Point

During the commissioning and characterisation of the new 166-pixel TRISTAN detector module, it was thoroughly investigated with photons using an ^{55}Fe source in the dedicated laboratory setup at MPP, see section 5.2. An important part of this characterisation was to determine the optimal detector working point. To this end, all relevant detector voltages, which are described in more detail in section 3.2.3, were varied in a suited parameter space and the optimal values were extracted based on the following four parameters: The number of working detector channels, the average detector energy resolution, the stability of the energy calibration in terms of the peak positions in the acquired spectra and the stability of the total count rate. The measurements were performed in vacuum at a temperature of $-27\,°$C at the SDD. The energy calibration was performed by fitting a Gaussian function and a shelf function to the Mn-K$_\alpha$ and Mn-K$_\beta$ lines in the ^{55}Fe spectrum. In addition, the energy resolution was extracted from the Mn-K$_\alpha$ line in terms of FWHM.

For all following analyses, supplementary plots of the investigated parameters on e.g. the stability of the count rate and the energy calibration can be found in the appendix B.

6.1 JFET Parameters

The integrated JFETs in the detector pixels require two supply voltages: The bias voltage V_{SSS} and the drain voltage V_{D}. In particular, the drain voltage V_{D} has a strong impact on the detector performance. A more intuitive parameter than V_{SSS} is the drain current I_{D} of the JFET. By varying V_{SSS} on the bias board, I_{D} is changed as well. The investigated range of I_{D} was $50\,\mu$A $\leq I_{\mathrm{D}} \leq 350\,\mu$A per detector channel. In the measurements, all pixels worked without distortions for all values and the stability of the count rate and the energy calibration were unaffected as well. However, as shown in figure 6.1a, an optimum in terms of energy resolution was found for a drain current of $I_{\mathrm{D}} = 200\,\mu$A.

The JFET drain voltage V_{D} has a stronger effect on the detector performance. As can be seen in figure 6.1b, for too high and too low voltages, the energy resolution is degraded. An optimum was found for a voltage of $V_{\mathrm{D}} = 7.5\,$V.
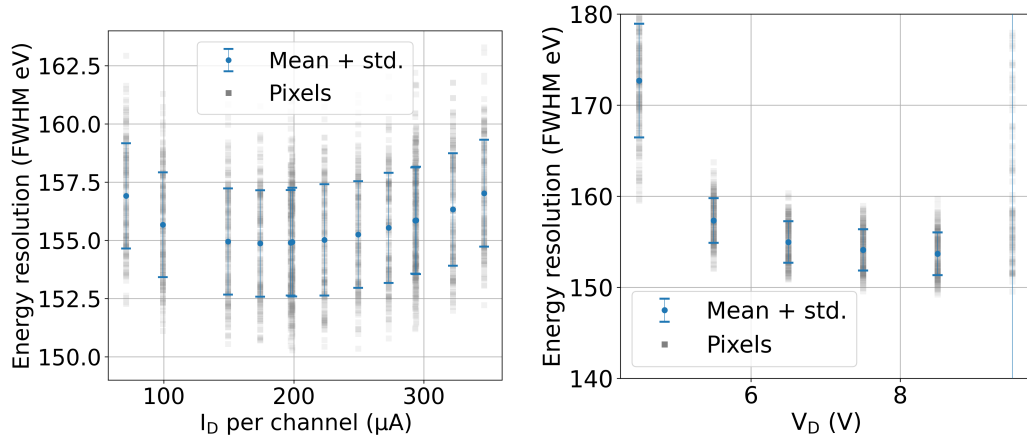
(a) Effect of I_{D} on the energy resolution.

(b) Effect of V_{D} on the energy resolution.
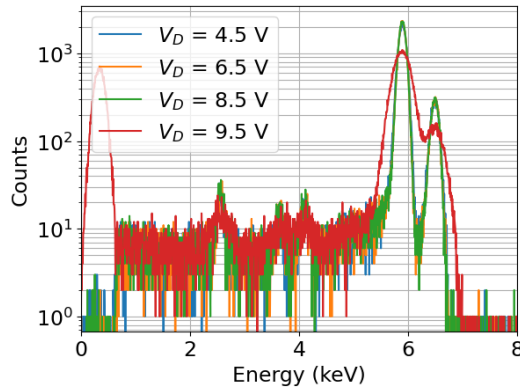
(c) Effect of V_{D} on the spectrum.

Figure 6.1: Effect of the JFET current I_{D} (a) as well as of the drain voltage V_{D} (b) on the energy resolution in a measurement with an ^{55}Fe source. The mean energy resolution for all pixels as well as the standard deviation are represented by the blue points and error bars, respectively. The values for the individual pixels are plotted in grey. The effect of V_{D} on the spectrum is shown in (c). For too high voltages, spectral distortions appear and the energy resolution is degraded. Adapted from [53].

Additionally, distortions in the spectrum, depicted in figure 6.1c, became apparent for too high voltages. However, the count rate and energy calibration were stable over the investigated voltage range.

6.2 Reset Parameters

To prevent a saturation of the first stage detector output, a reset mechanism is required. The reset is managed by external electronics and can be adjusted by the following parameters: The reset voltages V_{ResH} and V_{ResL}, and the reset length T_{Reset}. As long as the values are within their specifications, no significant effect of those parameters on the detector performance is expected.

Reset Voltages

To determine the optimal detector working point in terms of the reset logic, first the voltage V_{ResH} was varied in the range $2.5\,\text{V} \leq V_{\text{ResH}} \leq 5\,\text{V}$. The voltage is applied to the anode to discharge the anode and therefore initiates the reset. During the measurement, all pixels were functional. The detector functionality and performance was not affected by varying the voltage. The effect of V_{ResH} on the energy resolution can be seen in figure 6.2a. No significant effect was observed, i.e. the energy resolution stayed approximately constant within the scanning range. This is also true for the count rate and the energy calibration. The calculated expectation for V_{ResH} amounts to $V_{\text{ResH}} = 4\,\text{V}$, therefore this value was used for all subsequent measurements.

The voltage V_{ResL} is applied in between the reset pulses to the anode reset diode and prevents the reset, as it should close the connection to the anode as long as $V_{\text{IGR}} < V_{\text{ResL}} < V_{\text{R1}}$. The voltage was varied in the range $-13\,\text{V} \leq V_{\text{ResL}} \leq -7\,\text{V}$. The nominal value amounts to $V_{\text{ResH}} = -10\,\text{V}$. Just as for the voltage V_{ResH}, the detector performance was not affected by the parameter and no significant effect was observed on the energy resolution, see figure 6.2b. The count rate and the energy calibration were stable as well. Therefore, $V_{\text{ResL}} = -10\,\text{V}$ was used for all subsequent measurements.

Reset Length

Finally, the impact of the duration of the reset on the detector performance was investigated. To this end, the reset length was varied in the range of $0.75\,\mu\text{s} \leq T_{\text{Reset}} \leq 5\,\mu\text{s}$. If the reset length is too short, the anode is not fully discharged. A longer reset time than necessary increases the dead time of the system but otherwise has no negative effect on the detector performance. For the tested values, no significant effect on the energy resolution, or on the count rate and energy calibration was observed, as can be seen in figure 6.2c.
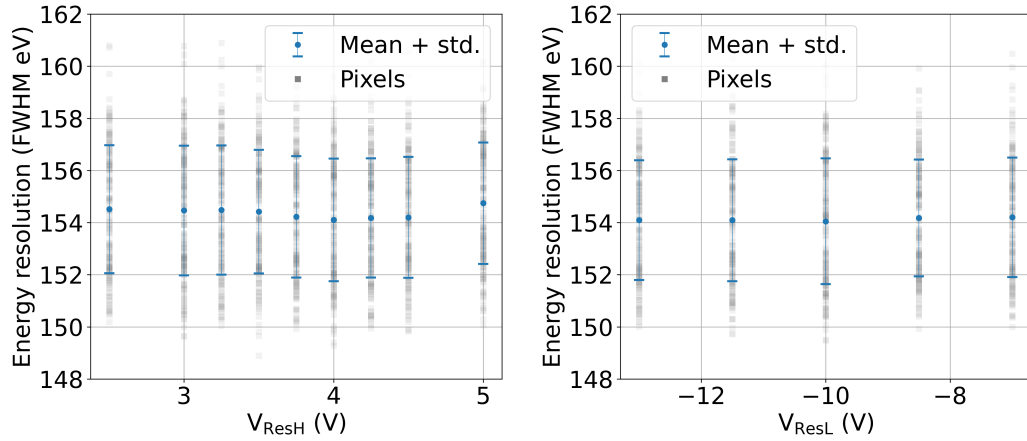
(a) Effect of V_{ResH} on the energy resolution.

(b) Effect of V_{ResL} on the energy resolution.
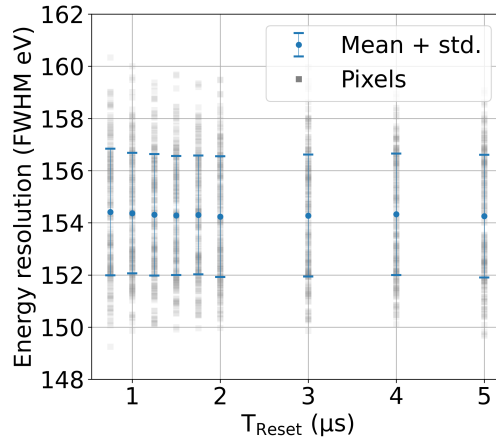
(c) Effect of T_{Reset} on the energy resolution.

Figure 6.2: Effect of the reset parameters on the energy resolution. The blue points and error bars represent the mean of the energy resolution of all pixels and the standard deviation, respectively. The grey dots represent individual pixels. For all three parameters, no significant impact on the energy resolution was observed. Adapted from [53].

For most of the measurements that were carried out prior to this characterisation campaign, a value of $T_{\text{Reset}} = 1.5\,\mu\text{s}$ had been used to ensure that the anode is fully discharged. Consequently, this value was also used for the measurements carried out in the scope of this thesis.

6.3 Back Contact, Ring 1 and Ring X Voltages

The detector back contact voltage V_{BC}, ring 1 voltage V_{R1} and ring X voltage V_{RX} are responsible for the depletion of the detector, as well as for the shape of the electric potential inside the detector. Therefore, all three voltages are expected to have a strong impact on the detector performance.

Back Contact Voltage
For the investigation of the effect of the back contact voltage, a sweep over various combinations of back contact and ring 1 voltages was performed. The voltages were varied in the ranges $-130\,\text{V} \leq V_{\text{BC}} \leq -95\,\text{V}$ and $-14\,\text{V} \leq V_{\text{R1}} \leq -9.5\,\text{V}$. For the investigation, both the back contact and back frame voltages were supplied externally by a source meter. The voltages V_{BC} and V_{BF} were varied simultaneously, so that the relation $V_{\text{BF}} = V_{\text{BC}} - 10\,\text{V}$ held at all times. The ring 1 voltage was still supplied by the bias system.

Varying the two voltages had a strong influence on the functionality of the detector. Only a narrow working point was found, in which the detector was fully functional. For other voltage combinations, many pixels showed distortions in the energy spectra or even stopped working. Figure 6.3a shows the effect on the energy resolution for all functional pixels. For the working voltage combinations, the energy resolution as well as the energy calibration and the count rate were comparable and no voltage combination was clearly favoured. Since the working point for $V_{\text{BC}} = -115\,\text{V}$ and correspondingly $V_{\text{BF}} = -125\,\text{V}$ was more stable with respect to the ring 1 voltage, these values were used for the subsequent measurements.

Ring 1 and Ring X Voltages
In the next step, the impact of the ring 1 and ring X voltages on the detector performance were investigated. Both voltages were supplied externally by a source meter, while the other detector voltages were supplied by the bias system. For the measurements, the voltages were varied in the ranges $-130\,\text{V} \leq V_{\text{RX}} \leq -90\,\text{V}$ and $-15\,\text{V} \leq V_{\text{R1}} \leq -5\,\text{V}$. These measurements were performed for inner guard ring voltages of $V_{\text{IGR}} = -20\,\text{V}, -25\,\text{V}$ and $-30\,\text{V}$. The effect on the energy resolution for all functional pixels is shown in figures 6.3b- 6.3d.

For the investigated inner guard ring voltages, a narrow window in which the detector is functional was found.

(a) V_{BC}-V_{R1} sweep.

(b) V_{RX}-V_{R1} sweep for $V_{\mathrm{IGR}} = -20\,\mathrm{V}$.

(c) V_{RX}-V_{R1} sweep for $V_{\mathrm{IGR}} = -25\,\mathrm{V}$.

(d) V_{RX}-V_{R1} sweep for $V_{\mathrm{IGR}} = -30\,\mathrm{V}$.
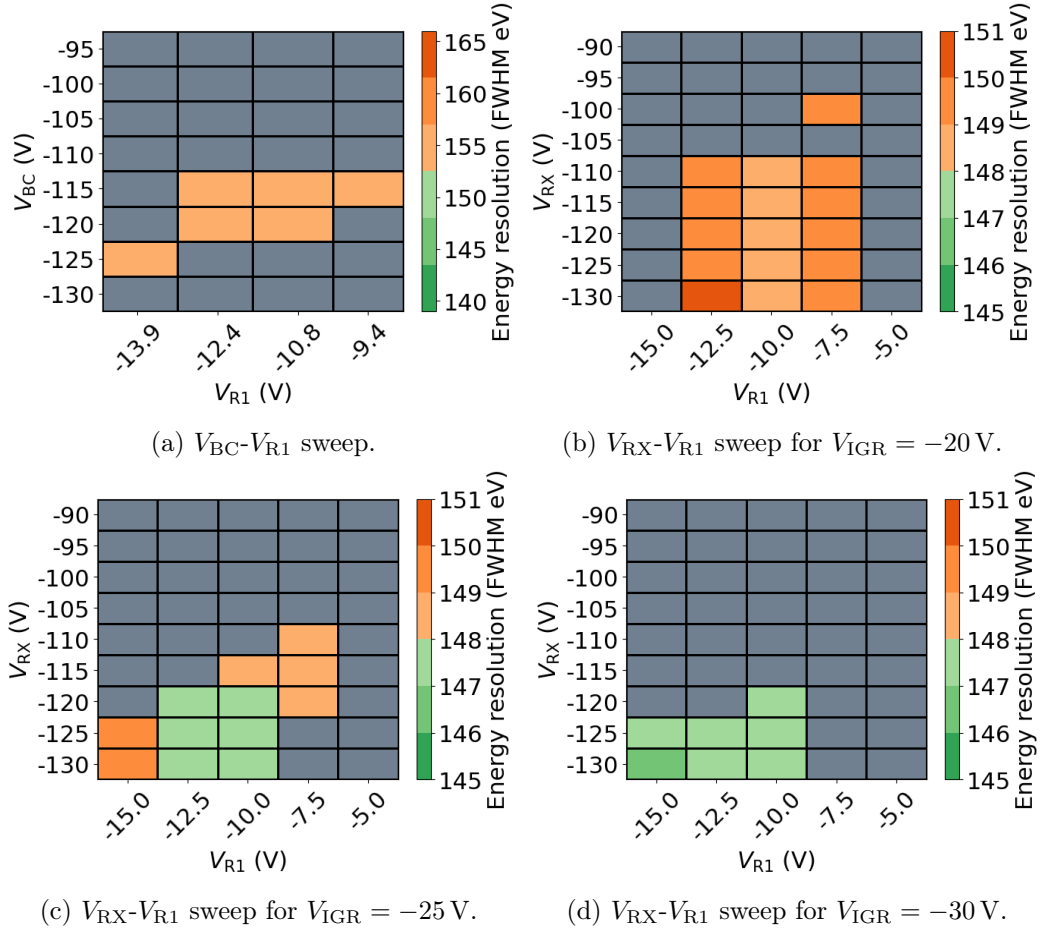
Figure 6.3: Effect of V_{BC} (a) and V_{R1} and V_{RX} (b-d) on the mean of the energy resolution. The V_{R1} and V_{RX} sweep was performed at different V_{IGR}. Voltage combinations, for which one or more pixels show distortions or stopped working are shown in grey. (a) A narrow working point exists, where all pixel are functional. In this region, no voltage combination is preferred. (b) For voltage combinations inside the working point, no significant effect on the energy resolution is observed. (c) More negative Ring X voltages $-130\,\mathrm{V} \leq V_{\mathrm{RX}} \leq -120\,\mathrm{V}$ with $-12.5\,\mathrm{V} \leq V_{\mathrm{R1}} \leq -10\,\mathrm{V}$ are preferred. (d) The working point is narrower for more negative V_{IGR}. No significant effect on the energy resolution is observed.

The working point heavily depended on the inner guard ring voltage and became narrower for more negative inner guard ring voltages. For the voltage combinations for which all pixels were functional, the energy resolution, energy calibration and count rate were stable. For the subsequent measurements, the voltages $V_{\mathrm{RX}} = -120\,\mathrm{V}$ and $V_{\mathrm{R1}} = -10\,\mathrm{V}$ were used. This is a stable voltage combination for all inner guard ring voltages, where the combinations around it are still functional.

6.4 Inner Guard Ring

The inner guard ring guards the integrated JFET from electrons that are guided towards the anode. If the voltage applied to the inner guard ring is not correct, charges can be guided directly into the JFET and therefore be lost. For a more detailed analysis of the charge loss at the inner guard ring see [63]. To avoid charge losses, the inner guard ring voltage V_{IGR} has to be optimised. Dedicated measurements were performed to determine the optimal detector working point with respect to this voltage by varying it in the range $-30\,\mathrm{V} \leq V_{\mathrm{IGR}} \leq -15\,\mathrm{V}$.
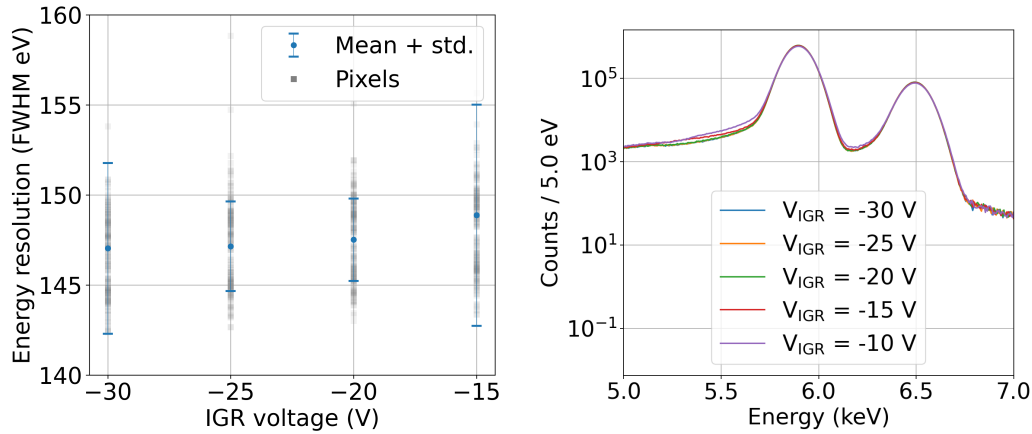
(a) Effect of V_{IGR} on the energy resolution.

(b) Effect of V_{IGR} on the ^{55}Fe spectrum

Figure 6.4: Effect of the inner guard ring voltage on the energy resolution (a) and the spectrum (b). (a) The blue points and the error bars represent the mean of the energy resolution and the standard deviation, respectively. The grey dots represent individual pixels. No significant improvement of the energy resolution was observed. However, $V_{\mathrm{IGR}} = -20\,\mathrm{V}$ has a smaller spread of the energy resolution of the pixels and is therefore preferred. (b) The ^{55}Fe energy spectrum for different inner guard ring voltages with a zoom on the peak region. If the voltage V_{IGR} is too high, a shoulder on the lower energy part of the peaks appear. Adapted from [53].

The voltage V_{IGR} had no significant impact on the energy resolution, see fig-

ure 6.4a, the count rate, the energy calibration or the detector functionality. However, too positive voltages, e.g. $V_{\text{IGR}} = -15\,\text{V}$, lead to low-energy tails on the low-energy part of peaks, see figure 6.4b. An optimal value of $V_{\text{IGR}} = -20\,\text{V}$ was determined because the spread of the energy resolution of the individual pixels was smaller and the working point in the ring 1 and ring X voltage sweep was broader for this value.

6.5 Summary

The detector functionality and performance is influenced by the applied voltages. Relevant voltages are the supply voltages for the JFET, the voltages regulating the reset mechanism, the voltages responsible for the depletion of the detector and the formation of a sufficient electric field inside the detector as well as the inner guard ring voltage. These voltages were varied in order to optimise the detector performance.

For some ranges of the drain voltage and the inner guard ring voltages, spectral distortions were observed in the energy spectra of certain pixels. Only a narrow working point in regards to combinations of the back contact, ring 1 and ring x voltages was found, where all pixels were functional. The optimal detector voltages are listed in table 6.1. Those are used for all subsequent measurements, together with a reset length of $T_{\text{Reset}} = 1.5\,\mu\text{s}$. Using these values, the energy resolution of a 166-pixel TRISTAN detector module was improved from 155 eV to 146 eV at a peaking time of $t_{\text{peak}} = 2\,\mu\text{s}$ for 5.9 keV photons.

Table 6.1: Optimal detector voltages, which were used for all subsequent measurements

	Value in V
BF	-125.0
BC	-115.0
IGR	-20.0
R1	-10.0
RX	-120.0
V_{SSS}	-3.9
V_{D}	7.5
V_{ResH}	4.0
V_{ResL}	-10.0

Chapter 7

First Investigations in the KATRIN Monitor Spectrometer

To search for keV-scale sterile neutrinos, the final TRISTAN detector will replace the current focal plane detector in the KATRIN beamline and measure electrons from the tritium beta-decay. To ensure the functionality of the module design, it has to be tested in an as realistic environment as possible. For this task, the MoS is chosen as a test stand. In this chapter, the S0-166-04 detector module is characterised for the first time in a MAC-E filter environment at the MoS. To ensure a working detector, it is first commissioned with ^{55}Fe, as described in section 7.1. Due to entrance window effects, the calibration especially for measurements with electrons is not trivial. Therefore, different available calibration methods are discussed in section 7.2. For the analyses presented in this thesis, a calibration method using wall electrons is being used for all data sets. The first characterisation of the detector module with electrons is summarised in section 7.3.

For the following measurements, the detector was cooled down to a temperature of $T_{\mathrm{SDD}} = -29\,°\mathrm{C}$ at the SDD. The CAEN DAQ described in section 5.1 is used for the data acquisition. For the characterisation measurements, the detector bias voltages listed in table 6.1 and obtained by the optimisation measurements presented in chapter 6 are used.

7.1 Commissioning with ^{55}Fe

To ensure the functionality of the detector module, the first tests in the MoS are conducted with an ^{55}Fe source. The ^{55}Fe source is installed in the source holder onto the new calibration arm. Due to its high activity, aluminium foil with a thickness of approximately $80\,\mu\mathrm{m}$ is put into the source holder between the source and the detector. This is done in order to reduce the amount of radiation reaching the detector. In figure 7.1, the ^{55}Fe spectrum is shown for all pixels. Out of 166 pixels, 165 are working. All of those pixels show a clean spectrum with five visible peaks. The two main peaks correspond to the Mn-K_α and Mn-K_β lines of the ^{55}Fe source. Those two peaks are well separated, indicating a good energy resolution of the detector. Two

silicon escape peaks are visible, which are located 1.74 keV below the main peaks [64]. Another peak at lower energies results from the aluminium foil in the source holder and corresponds to the aluminium fluorescence line at $E_{Al} \approx 1.5$ keV.

A quantitative measure of the performance of the detector module is the energy resolution. To determine the energy resolution, each iron peak is fitted with a simplified model containing a Gaussian function and a shelf function. The Gaussian function is fitted in a narrow window where the detector response is described well by a Gaussian function. A Gaussian fit to an exemplary spectrum is shown in figure 7.2. The means of both Gaussian functions are used for calibration, while the energy resolution is calculated with the variance σ extracted from the Gaussian fit of the peaks and is given in terms of FWHM. In the following analyses, only the energy resolution of the Mn-K_α peak is considered, since it contains more statistics.

In figure 7.3, the corresponding energy resolution is shown in a pixel map. Out of 166 pixels, 165 pixels are functional and the detector shows a homogeneous behaviour of the energy resolution. The median energy resolution of the detector amounts to $\overline{\Delta E_{\mathrm{FWHM}}} = 151$ eV at a peaking time of 2 µs for photon energies of $E_\gamma = 5.9$ keV. This is very comparable to measurements at the test stand at the MPP, where the detector yields a median energy resolution of $\overline{\Delta E_{\mathrm{FWHM}}} = 147$ eV at a peaking time of 2 µs for photon energies of $E_\gamma = 5.9$ keV.
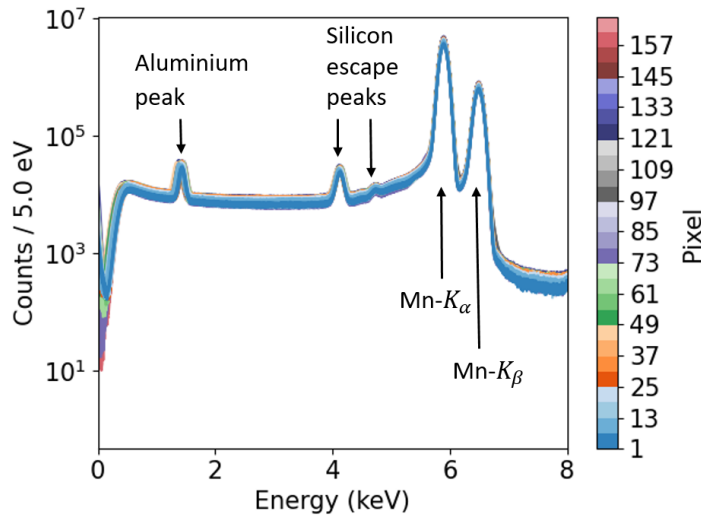
Figure 7.1: ^{55}Fe spectrum of all pixels measured in the MoS. Out of 166 pixels, 165 pixels are working and show a clean spectrum with well separated Mn-K_α and Mn-K_β peaks. Both silicon escape peaks 1.74 keV below the main peaks are visible as well as a fluorescence line from aluminium at $E_{Al} \approx 1.5$ keV [64].
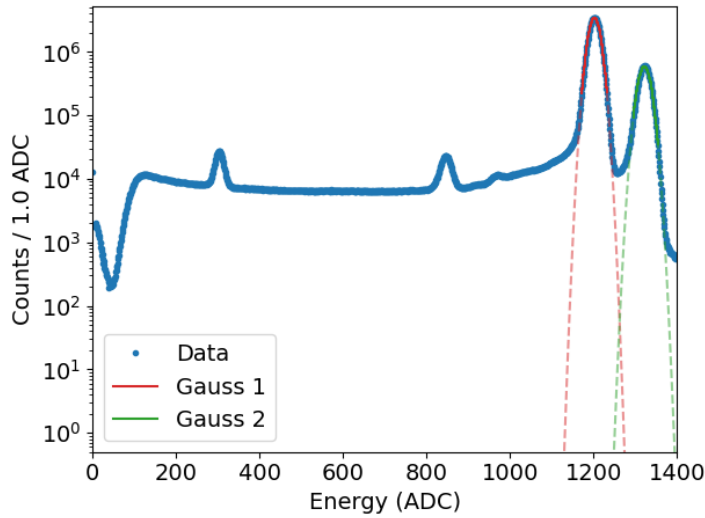
Figure 7.2: Exemplary fit of an ^{55}Fe spectrum. A Gaussian function is fitted to the Mn-K$_\alpha$ (solid red) and Mn-K$_\beta$ (solid green) peaks in a narrow window, where the peaks can be approximated as Gaussian functions. The interpolated Gaussian function of the fit are depicted with the dashed line in the respective colours. The means are used for calibration while the variance σ of the Mn-K$_\alpha$ peak is used to determine the energy resolution ΔE_{FWHM}.

The slightly worse energy resolution at the MoS can be attributed to the different setup with longer cables and additional noise sources in the MoS, e.g. unintentional light sources inside the spectrometer. A detailed noise investigation can be found in chapter 8.

Pixel 46 is not functional and therefore depicted in grey in the pixel map. This pixel shows an untypical behaviour on the waveform level, which was already observed in earlier tests at the MPP test stand and was fixed by adjusting cables and connections as well as the SDD voltages. At the MoS, however, it is difficult to get access to the in-vacuum connections once the detector is installed. Attempts to recover the pixel without this access were unsuccessful. Therefore, the pixel is excluded from all further analyses in the MoS.
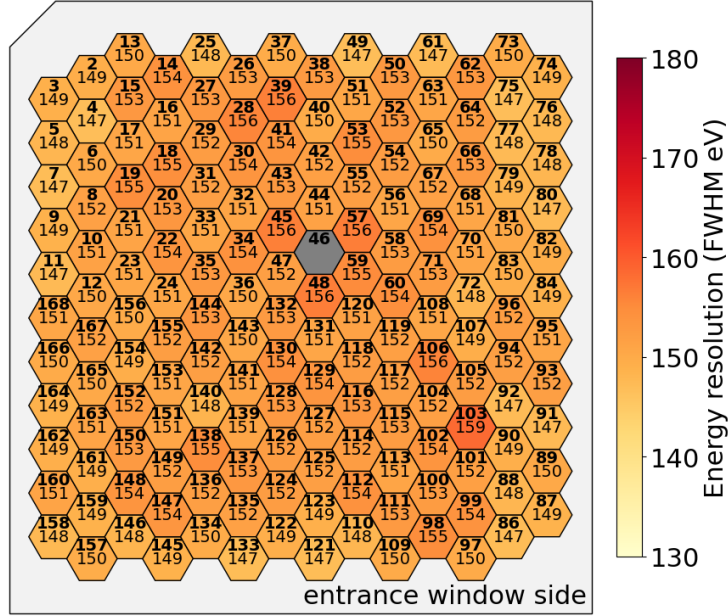
Figure 7.3: The energy resolution pixel map for the ^{55}Fe measurement in the MoS. The energy resolution across all pixels is homogeneous. Pixel 46 is depicted in grey and is deactivated due to untypical behaviour on the waveform level. The median energy resolution of the measurement in terms of FWHM is extracted from a Gaussian fit to the Mn-K$_\alpha$ peak and amounts to $\overline{\Delta E}_{\mathrm{FWHM}} = 151\,\mathrm{eV}$ at a peaking time of $2\,\mu s$.

7.2 Energy Calibration Methods in the MoS

For measurements with photons from the ^{55}Fe source, the Mn-K$_\alpha$ and Mn-K$_\beta$ lines can be directly used for energy calibration. For measurements with electrons in the MoS, however, the energy calibration is not straight forward. In principle, three energy calibration sources are available: ^{55}Fe, ^{83m}Kr and wall electrons. More information about the sources is given in chapter 5. In the following, the energy calibration methods and their shortcomings will be explained briefly.

Energy Calibration with ^{55}Fe
The isotope ^{55}Fe is a popular energy calibration source because it emits monoenergetic photons. Its measured spectra contain two peaks, which correspond to the Mn-K$_\alpha$ and Mn-K$_\beta$ lines, see table 5.1. These two peaks can be used for energy calibration. Because ^{55}Fe is a photon emitter, the effect of the entrance window is minimal, leading to an accurate energy calibration. However, the calibration can

only be done with two peaks at low energies, which are close to each other in energy. The calibration is therefore accurate for an energy range around approximately $0 - 10$ keV. For higher energies, however, the energy calibration becomes less suitable and it does not fit to the measured electron energy spectra. For wall electron energies of $E_{\mathrm{e}^-} = 31.6$ keV, where the entrance window effect is expected to be negligible, this can be seen in figure 7.4. There, the difference between the measured mean of the peaks calibrated with calibration parameters acquired from an ^{55}Fe measurement and the applied retarding potential is shown in a pixel map. The absolute median energy shift amounts to 279 eV, which is unacceptable for a calibration.
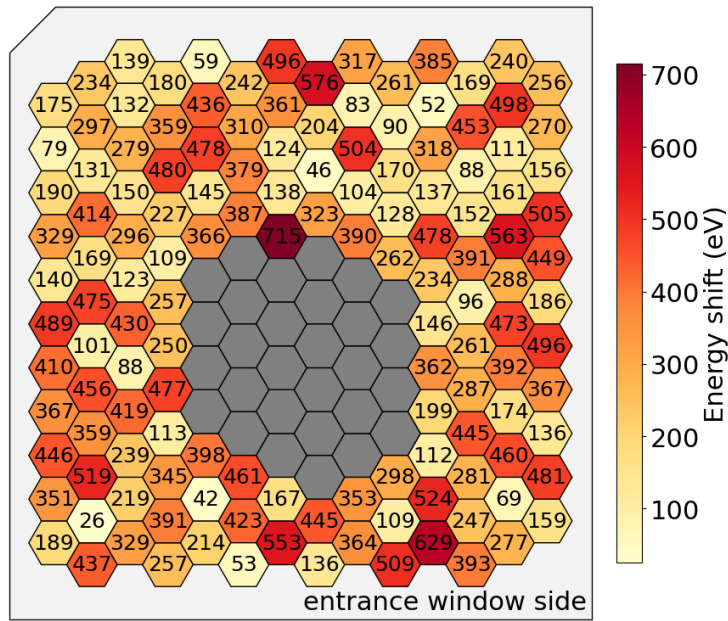
Figure 7.4: The absolute energy shift of a 31.6 keV wall electron measurement which was calibrated with calibration parameters extracted from an ^{55}Fe calibration. The energy shift is defined as the difference between the measured mean of the peaks calibrated with the ^{55}Fe calibration and the applied retarding potential in the MoS. The median energy shift amounts to 279 eV, which is unacceptable for a calibration.

Energy Calibration with Electrons from $^{83\mathrm{m}}$Kr

The main source of electrons in the MoS is the $^{83\mathrm{m}}$Kr source which is installed in the source chamber. This source emits multiple electron lines along with photon lines. However, the rate of the photons detected in the detector is negligible and therefore too small to use those for the energy calibration. The energies of all lines of interest are listed in table A.1. In theory, many lines are available for the energy

calibration. However, at lower energies, they overlap significantly and the effect of the entrance window has to be taken into account. Therefore, the best candidates are the well separated K32, L32 and M32 lines at $E_{K32} = 17.8 \, \text{keV}$, $E_{L32} = 30.2 \, \text{keV}$ and $E_{M32} = 31.8 \, \text{keV}$, respectively.

Analogous to the Mn-K_α and Mn-K_β peaks in case of the calibration with ^{55}Fe, this method produces a good energy calibration in a range close to the peaks but becomes less accurate at low energies due to the small distance between the two calibration points.

Another possibility is to calibrate with the M32 line and zero, assuming that $0 \, \text{ADC}$ corresponds to $0 \, \text{eV}$. To check the accuracy of this method, an offline manual trapezoidal filter analysis was performed on the waveform. The fluctuation of the null peak position is in the order $\mathcal{O}(25 \, \text{eV})$. Assuming a linear dependence of the energy calibration, this method is accurate on a wide energy range, because the two calibration points are spaced over nearly $32 \, \text{keV}$. In addition, it can be performed in the same run as the actual measurement.

However, electrons from the ^{83m}Kr source are more prone to entrance window effects than photons. Therefore, the measured energy is always shifted to lower energies depending on the entrance window thickness and the electron energy. This shift can be estimated with simulations to amount to $40 \, \text{eV}$ for electrons with an energy of $32 \, \text{keV}$ and an effective entrance window thickness of $50 \, \text{nm}$ [41]. In addition, source effects are present in the ^{83m}Kr source, which can lead to a degradation of the energy resolution and small spectral distortions. This might also introduce an uncertainty to the energy calibration.

Energy Calibration with Wall Electrons

Due to the variable retarding potential inside the spectrometer, different energies of wall electrons can be selected. This way, there are no distortions due to overlaps of multiple lines for each selected energy. An exemplary wall electron spectrum measured at the MoS is shown in figure 7.5. For an energy calibration with wall electrons, the peak at different wall electron energies is fitted with the electron response function, see eq. 5.4. The peak positions, which are defined as the position of the maximum of the peaks, are plotted against the applied retarding potential to obtain a calibration curve. This is fitted linearly to extract the calibration parameters slope and offset. An exemplary calibration curve is shown in figure 7.6. The voltages are known precisely with an uncertainty of $< 1 \, \text{V}$. However, for lower incident energies, the effect of the entrance window becomes larger, shifting the measured maximum of the wall electron peak to lower energies. This can be seen in the residuals of figure 7.6. To minimise this effect, only wall electron energies above $20 \, \text{keV}$ are used for the energy calibration. Nevertheless, an error of about $30 \, \text{eV}$ is introduced due to the entrance window effect.
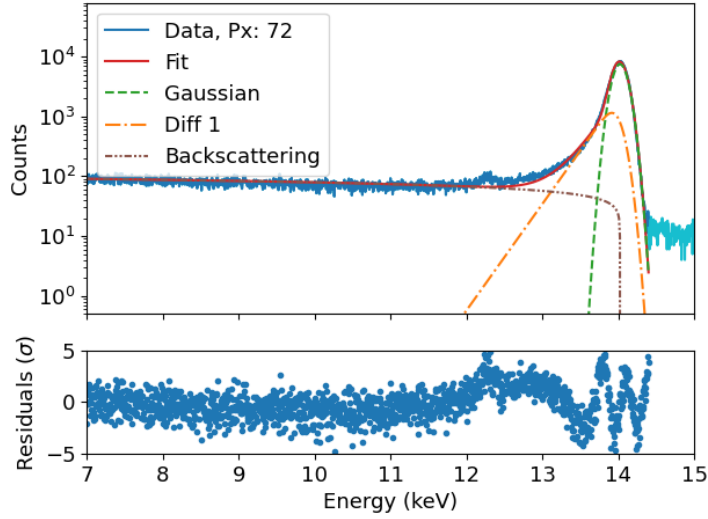
Figure 7.5: Fit of an exemplary wall electron spectrum at 14 keV. The data inside the fitting range is shown in blue. The fit (red) consists of a Gaussian component (green), a diffusion term (orange) and a backscattering tail (brown).

The center region of the detector receives only a small rate of wall electrons in the wall electron configuration. Additionally, some pixels in the center are illuminated by the ^{83m}Kr source, which overlaps with the wall electron spectra for high wall electron energies. For these reasons, some pixels are excluded from the energy calibration with wall electrons. A pixel map with included and excluded pixels is shown in figure 7.7.

An energy calibration with wall electrons has several advantages. First, it is possible to perform the calibration and the actual measurement in the same setup with regards to the magnetic fields, detector position and temperature. Furthermore, because the calibration and the measurement source is the same, additional uncertainties from possible source effects can be excluded. This ensures equal conditions for the calibration and the calibrated measurement. Secondly, because four calibration points are used, the calibration is rather robust and accurately reproduces the wall electron energies extracted from the spectra down to $\mathcal{O}(50\,\text{eV})$ for energies higher than 10 keV, as can be seen in the residuals in figure 7.6. Therefore, an energy calibration with wall electrons is used for all wall electron measurements in the MoS in the scope of this thesis.
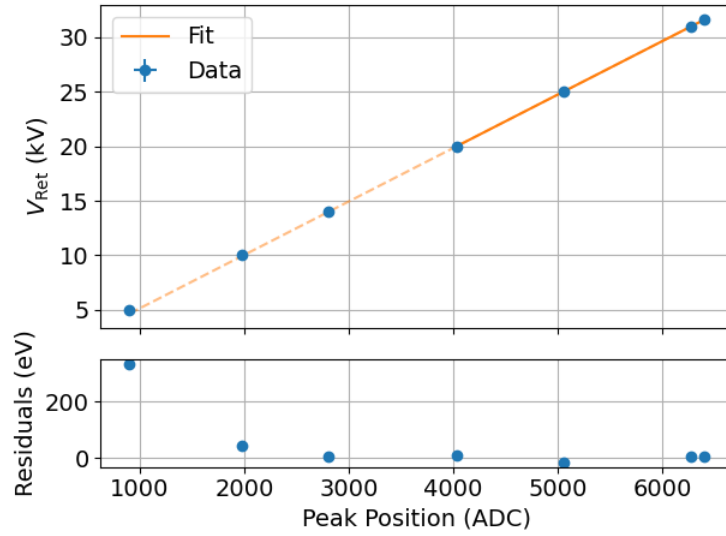
Figure 7.6: Exemplary energy calibration curve for wall electrons. The peak position is plotted over the retarding potential V_{Ret} (blue). The linear fit to the four most energetic wall electron data points is depicted by the solid orange line. The dotted orange line shows the interpolation of the fitted energy calibration to lower energies. In the lower panel, the residuals in eV are shown. Although the energy calibration becomes less accurate for lower energies due to the increasing impact of the entrance window, the energy calibration is accurate for all energies except for 5 keV up to $\mathcal{O}(50\,\text{eV})$.
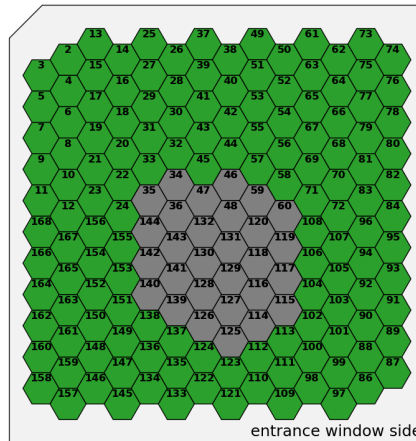
Figure 7.7: Calibrated pixels illustrated in a pixel map. The green pixels were calibrated with wall electrons. The grey pixels are excluded from the analysis because of low rates and overlap from the $^{83\text{m}}$Kr source.

Ideal Energy Calibration Source

None of the discussed energy calibration sources is ideal for characterisation measurements of TRISTAN detector modules at the MoS. For future modules, a better calibration source would be beneficial. An ideal calibration source emits multiple well defined and well separated photon lines to minimise entrance window effects and to get an accurate energy calibration over a wide range of energies. One example of such a source is ^{241}Am, which was already used for energy calibration and characterisation purposes with TRISTAN detectors, see e.g. [65]. Unfortunately such a source was not available for the measurements performed in the scope of this thesis. However, an installation on the calibration arm is possible for future measurements.

7.3 First Investigations with Wall Electrons

The final TRISTAN detector system will measure electrons from the beta-decay of tritium in the KATRIN beamline. Therefore, the characterisation of the detector response for electrons is crucial. The first characterisation of the 166-pixel TRISTAN detector module with electrons have been performed at the MoS with two different electron sources: conversion electrons from the decay of the isotope ^{83m}K and wall electrons. The characterisation of the detector module with the installed ^{83m}Kr source in the MoS is explained in detail in [53]. This thesis will focus on the first characterisation of the detector module with wall electrons in the MoS. By setting the retarding potential to different values, different energies of wall electrons can be achieved. The retarding potential is known very precisely and fluctuates with less than 1 V. The wall electrons can therefore be regarded as a monoenergetic electron source. A list of the performed measurements with their selected electron energies, their runtime and their median energy resolution in terms of FWHM is shown in table 7.1. All measurements are performed at a temperature of roughly $T_{\mathrm{SDD}} = -29\,°\mathrm{C}$ at the SDD. The wall electron energies were chosen over a wide range to be able to observe and investigate possible energy-dependent effects, such as the influence of the entrance window. The highest energy was chosen to be comparable to the ^{83m}Kr M32 line.

To analyse the performance of the 166-pixel detector module in the MoS, first the energy resolution for electrons is investigated. To this end, each pixel is fitted with the electron function, which is explained in detail in section 5.4, and calibrated with the parameters extracted from the calibration curve. An exemplary fit to a wall electron spectrum and an exemplary calibration curve can be seen in figure 7.5 and figure 7.6, respectively. The energy resolution is extracted in terms of FWHM from the fitted curve to the spectrum.

---

[1]Because of heavy distortions of the peak in pixels in the region with worse energy resolution, this value should only be understood as on order of magnitude.

Table 7.1: Energy, runtime and median energy resolution of measurements with wall electrons.

Energy (keV)	Runtime (h)	Median ΔE_{FWHM} (eV)
5.0	2.00	610[1]
10.0	2.00	280
14.0	2.00	270
20.0	2.00	285
25.0	2.00	303
31.0	15.75	326
31.6	2.00	332

It is shown in figure 7.8 and figure 7.9 in form of pixel maps, that represent the location of the pixels on the detector as seen from the source, for each investigated wall electron energy. The median energy resolution of the detector module is listed in table 7.1 for all measurements.

From the characterisation with photons, see section 7.1, a homogeneous energy resolution on the whole detector module is expected. In the wall electron measurements at the MoS, however, a half moon shaped region exists for all measurements, in which the energy resolution is significantly worse compared to the rest of the detector module. The difference in energy resolution in this region compared to the rest of the detector module is decreasing with increasing incident energy. At high incident energies, however, another effect appears, which leads to a degradation of the energy resolution in the upper left corner of the detector, see figure 7.9. The origin of this effect is not yet understood. However, it is an effect unique to measurements with wall electrons and it is not observed in $^{83\mathrm{m}}$Kr measurements. The additional effect could stem from the influence of the magnetic field configuration for wall electron measurements on the electron properties or other setup specific effects. Moreover, pixel 163 expresses a significantly worse energy resolution than its neighbouring pixels for higher incident energies. This is assumed to be due to an additional entrance window effect which only affects this specific pixel. The origin of this effect is currently under investigation.

The half moon shaped region of worse energy resolution is also observed in $^{83\mathrm{m}}$Kr measurements with the same detector module in the MoS. The effect is independent of the detector position inside the MoS and therefore also independent of the magnetic field lines. Because it always affects the same pixels, it is likely a detector effect rather than an effect of the source or the setup. It is consistent with the hypothesis that the region on the detector which expresses a worse energy resolution, has a thicker entrance window compared to the region on the detector with better en-

ergy resolution. More details on ^{83m}Kr measurements and additional measurements regarding this effect can be found in [53].

(a) $E_{\mathrm{Wall}} = 5\,\mathrm{keV}$

(b) $E_{\mathrm{Wall}} = 10\,\mathrm{keV}$

(c) $E_{\mathrm{Wall}} = 14\,\mathrm{keV}$
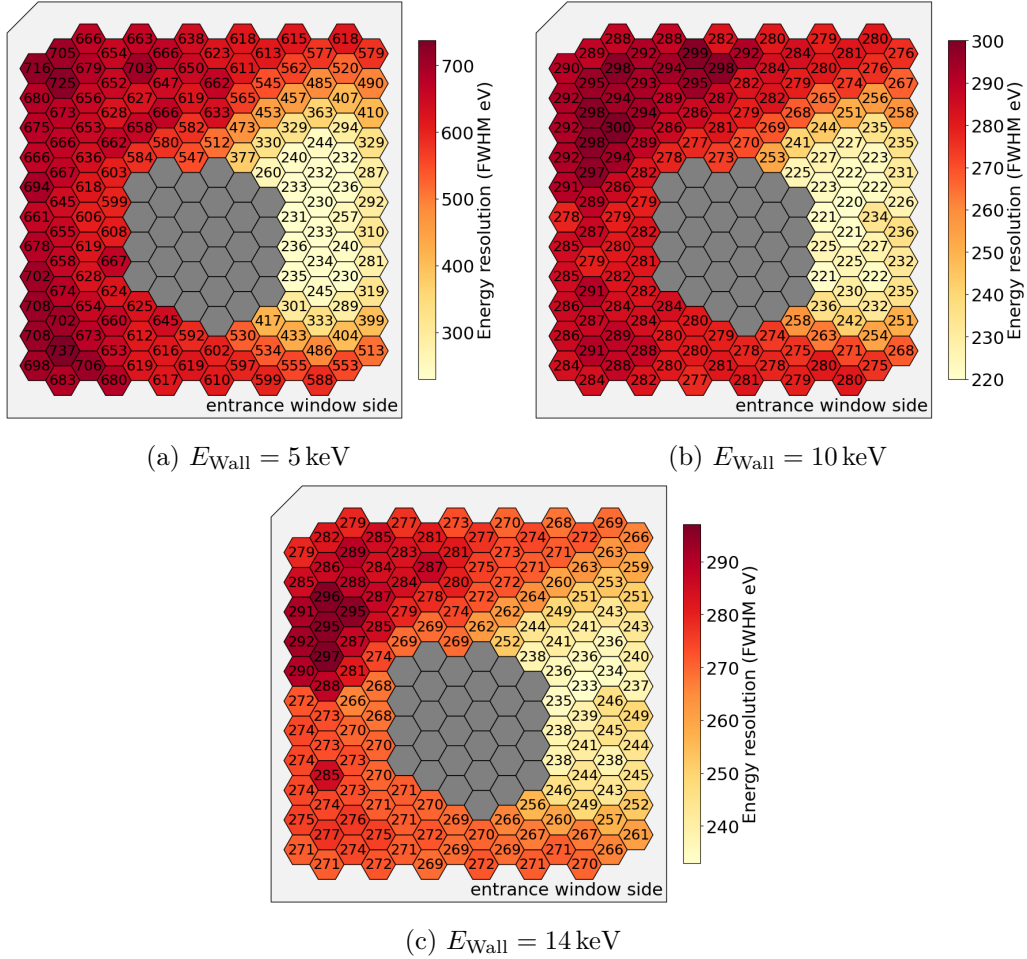
Figure 7.8: Energy resolution pixel maps for the wall electron analysis for electron energies of 5 keV, 10 keV and 14 keV. Note that the scale of the colourbar is not equal for all plots. For all wall electron energies, a roughly half moon shaped region is observed, where the energy resolution is significantly worse compared to the rest of the detector. The effect is energy-dependent and increases with decreasing electron energy, hinting at an entrance window effect. Because of spectral distortions for $E_{\mathrm{Wall}} = 5\,\mathrm{keV}$, only the order of magnitude of the energy resolution is correct for this energy.

(a) $E_{\mathrm{Wall}} = 20\,\mathrm{keV}$

(b) $E_{\mathrm{Wall}} = 25\,\mathrm{keV}$

(c) $E_{\mathrm{Wall}} = 31\,\mathrm{keV}$

(d) $E_{\mathrm{Wall}} = 31.6\,\mathrm{keV}$
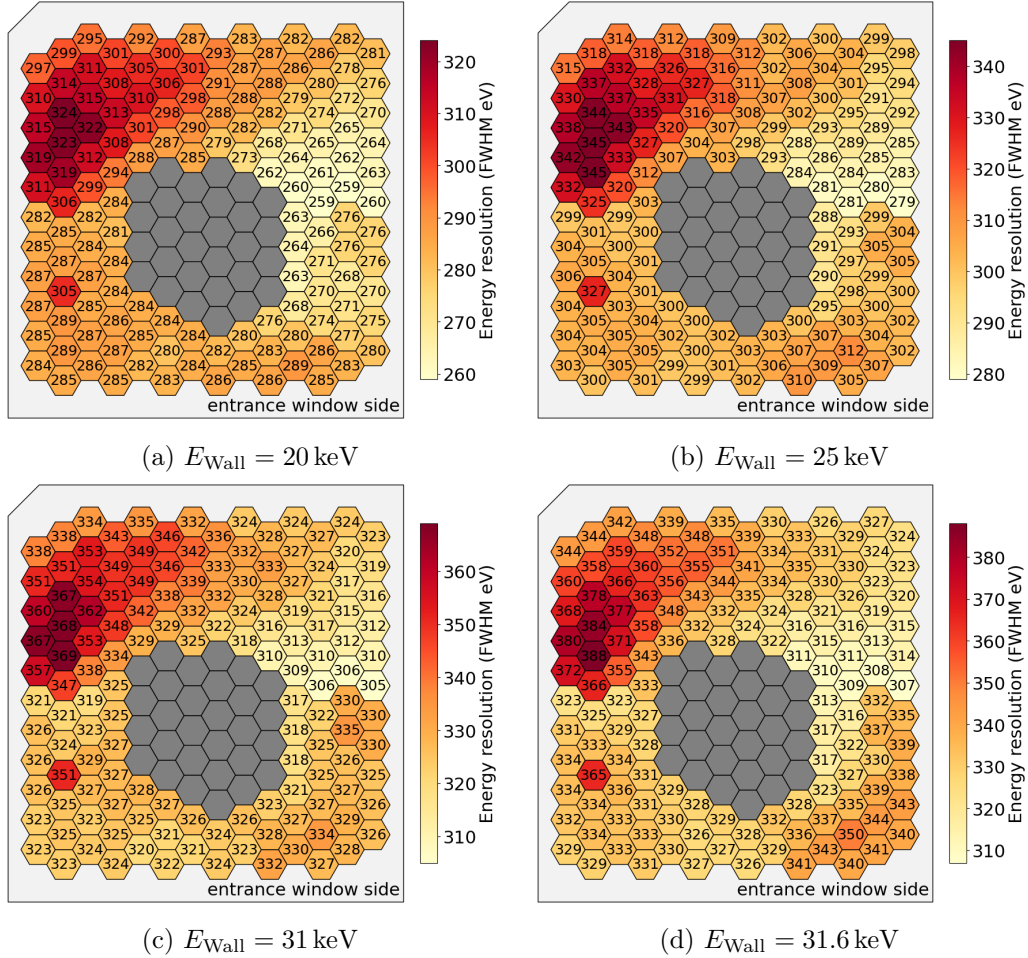
Figure 7.9: Energy resolution pixel maps for the wall electron analysis for electron energies of $20\,\mathrm{keV}$, $25\,\mathrm{keV}$, $31\,\mathrm{keV}$ and $31.6\,\mathrm{keV}$. These energies are used for calibration. Note that the scale of the colourbar is not equal for all plots. As for lower incident energies, a roughly half moon shaped region is observed, where the energy resolution is significantly worse compared to the rest of the detector. This effect is energy-dependent and is less pronounced for these high energies. Additionally, there is another effect that degrades the energy resolution at the upper left side of the detector, which is dominant for high incident energies. Moreover, pixel 163 (lower left) expresses a significantly worse energy resolution than the surrounding pixels.

Nevertheless, even with the worse energy resolution on one part of the detector, a median energy resolution of $\overline{\Delta E_{\text{FWHM}}} = 285\,\text{keV}$ at an incident electron energy of $E_{e^-} = 20\,\text{keV}$ and a peaking time of $t_{\text{peak}} = 2\,\mu\text{s}$ is achieved, which fulfills the requirement for the energy resolution of the final TRISTAN detector system.

Because of the different detector responses for electrons, the region with worse energy resolution and the region with better energy resolution will be examined separately in the following investigations. As a next step, the energy dependency of the energy resolution is examined for both regions, see figure 7.10.
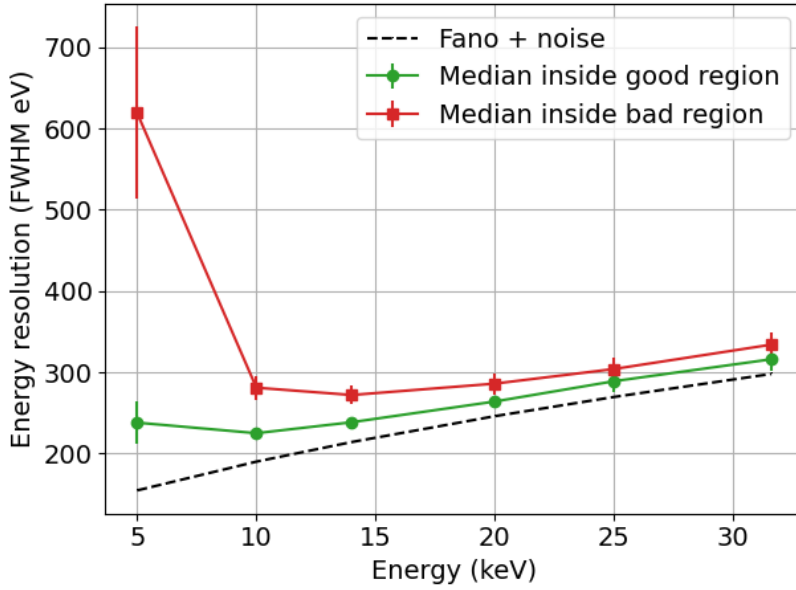
Figure 7.10: Energy resolution plotted against the incident energy of the wall electrons for the two regions of the detector. For all energies, the energy resolution outside the half moon shaped region (green) is better than inside (red). This effect is more pronounced for low incident energies. In black, the expected behaviour from Fano statistics and noise investigations is shown. The difference between the expectation and the measurements is due to entrance window effects. Due to spectral distortions for pixels in the region with worse energy resolution for $E_{\text{Wall}} = 5\,\text{keV}$, only the order of magnitude of the energy resolution is correct for this energy.

In general, the energy resolution is dependent on the noise of the setup, the energy of the incoming particle due to the Fano statistics and possible detector effects. The noise of the setup is assumed to be equal to the noise in the measurements for photons and is constant over the whole detector. A more detailed noise investigation, where the noise contribution $\sigma_{\text{el.}}$ is extracted, is performed in chapter 8. The Fano

statistics lead to an irreducible degradation of the energy resolution for increasing incident energies. The expectation for the energy resolution taking into account only the Fano statistics and the noise of the setup, however, underestimates the measured energy resolution for both the region with better energy resolution and the region with worse energy resolution. The difference between the expectation and the measurements is attributed to detector effects, where the main contribution is assumed to be the entrance window. The entrance window effect is especially important for electrons, as electrons have a shorter interaction length. Therefore, they are more likely to interact close to the entrance window surface. Inside the effective entrance window region the electric potential is not sufficient to guide all charge carriers to the anode. Therefore, a fraction of charge carriers that are created inside the effective entrance window region might be lost. In a spectrum, this leads to a shift of the peak towards lower energies and creates a shoulder on the low-energy side of the peaks. This additional shoulder broadens the peak, which affects the energy resolution in terms of FWHM. This effect is also energy dependent and decreases for increasing incident energies, as the mean free path of electrons decreases for decreasing incident energies. Therefore, electrons with lower energies are more likely to interact inside the entrance window region, which results in a worse energy resolution due to the low-energy shoulder on the peaks. For increasing energies, this effects becomes smaller. In summary, this means that at low incident energies, the effect of the entrance window is dominating the energy resolution, while at high incident energies, it is dominated by the Fano statistics. A difference in the thickness of the entrance window would therefore be more clearly observed for lower energy electrons. This is clearly observed in the wall electron data. While the median energy resolution of the region outside the half moon is better than inside for all energies, the difference in the median energy resolution for both regions is decreasing for higher energies. Again, this points to a thicker entrance window on the part of the detector where the energy resolution is worse compared to the rest of the detector as the origin of the observed effect. The best energy resolution can be achieved at $14\,\text{keV}$ for both regions.

In addition to the difference in energy resolution, a large difference in the shape of the spectrum is observed. This effect is more pronounced for lower incident energies and can be seen in figure 7.11. For all energies, pixels inside the half moon shaped region with worse energy resolution show a broader peak with pronounced shoulders towards lower energies. The lower the incident energy of the electrons, the more pronounced these features become in the spectrum. For $E_{\text{Wall}} = 5\,\text{keV}$, the peak of the pixels inside the half moon shaped region is heavily distorted, while for $E_{\text{Wall}} = 31.6\,\text{keV}$, only a slight shoulder towards lower energies is observed. This behaviour is also in agreement with the hypothesis of an increased entrance window thickness on the half moon shaped region on the detector.

(a) $E_{\mathrm{Wall}} = 5\,\mathrm{keV}$

(b) $E_{\mathrm{Wall}} = 10\,\mathrm{keV}$

(c) $E_{\mathrm{Wall}} = 31.6\,\mathrm{keV}$

(d) Location of pixels on the detector
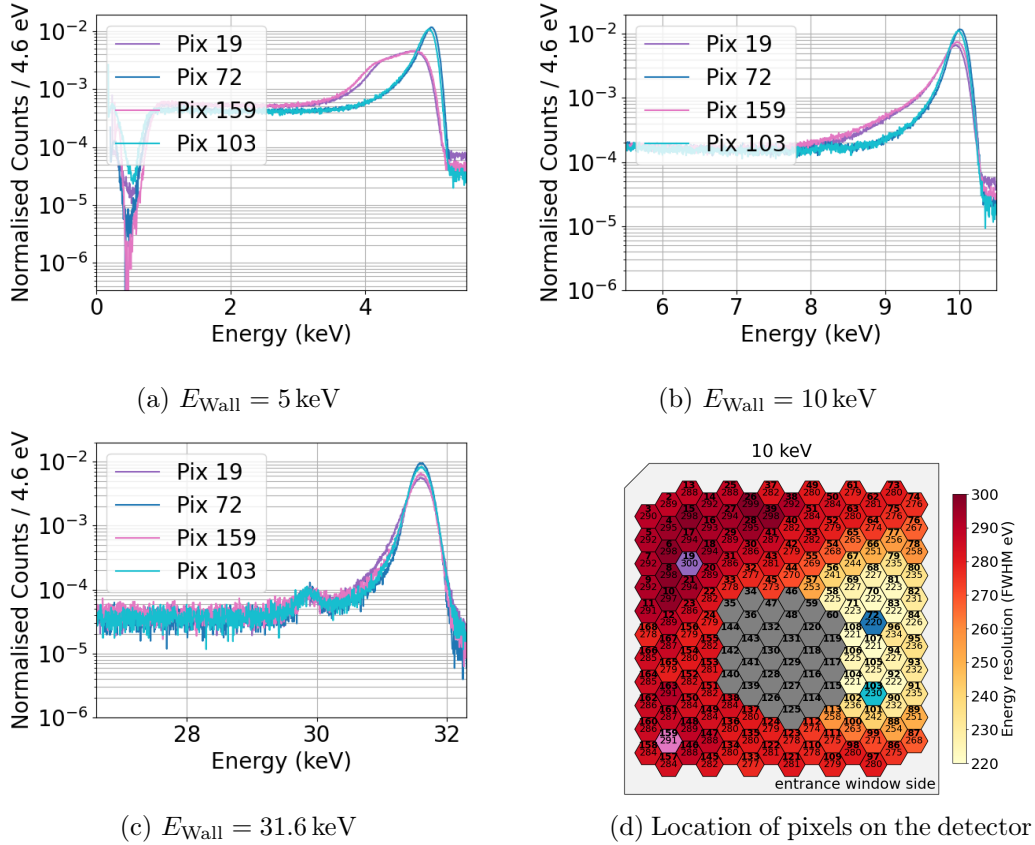
Figure 7.11: Comparison of spectra from selected pixels on different regions of the detector for (a) $E_{\mathrm{Wall}} = 5\,\mathrm{keV}$, (b) $E_{\mathrm{Wall}} = 10\,\mathrm{keV}$ and (c) $E_{\mathrm{Wall}} = 31.6\,\mathrm{keV}$. Pixel 72 and 103 (blue) are located in the region with better energy resolution. Pixel 19 and 159 (purple) are located in the upper left and lower left of the detector, respectively, where the resolution is worse. The locations of the pixels are marked in the pixel map (d). The spectra are scaled to the total counts in the spectra. For all energies, the pixels inside the half moon shaped region have worse energy resolution and pronounced shoulders towards lower energies. This effect is energy dependent. While it is very pronounced for low incident energies, e.g. $E_{\mathrm{Wall}} = 5\,\mathrm{keV}$ and $E_{\mathrm{Wall}} = 10\,\mathrm{keV}$, it is only slightly visible for $E_{\mathrm{Wall}} = 31.6\,\mathrm{keV}$. For very low energies ($E_{\mathrm{Wall}} = 5\,\mathrm{keV}$), the shape of the peaks for pixels inside the half moon shaped region is heavily distorted as well. This clear energy dependence in both energy resolution and spectral distortion hints at a thicker entrance window inside the half moon shaped region.

Due to the distortion of the peak for low incident energies, the electron response fit does not provide exact values for the energy resolution for $E_{\text{Wall}} = 5\,\text{keV}$. Nevertheless, the order of magnitude of the extracted values is correct.

In addition to a worse energy resolution and more pronounced shoulders towards lower energies of the peaks, a thicker entrance window would also result in an energy shift of the peak. This shift is defined as the difference between the measured energy at the maximum of the peak and the applied retarding potential. It is shown in figure 7.12 for the region on the detector with better energy resolution and the region with worse energy resolution separately.
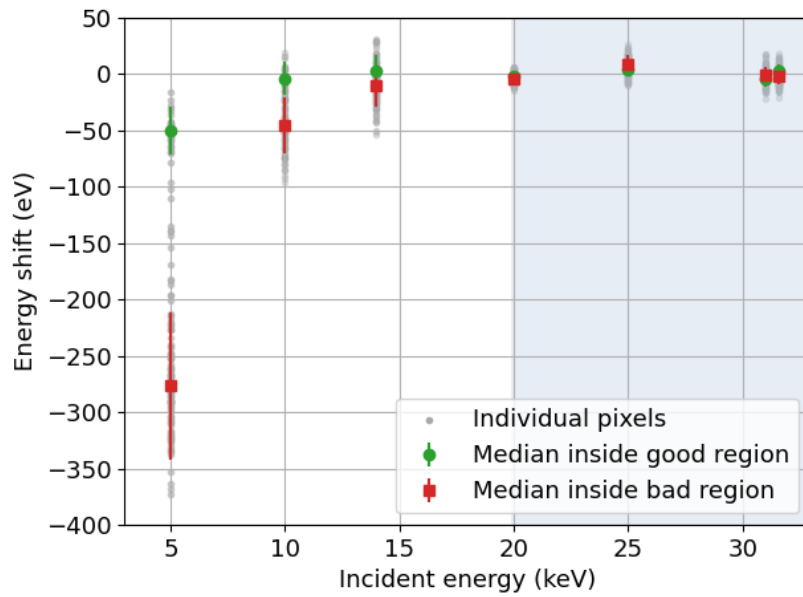
Figure 7.12: Median energy shift plotted against incoming energy for the region on the detector with better energy resolution (green) and for the region with worse energy resolution (red). The energy shift is calculated by taking the position of the maximum of the peak and calibrating this with the wall electron calibration. The applied spectrometer potential is subtracted from this value. For energies between $20 - 32\,\text{keV}$, the shift is close to zero as those energies are used for calibration. They are greyed out in the plot, as the entrance window effect is hidden by the calibration procedure. For decreasing energies, the entrance window effect leads to increasing energy shifts and the difference between the two detector regions increases. Pixels inside the region with worse energy resolution express a significantly higher energy shift than pixels in the region with better energy resolution.

Again, a clear energy dependency is visible. For the energies $20-32\,\text{keV}$, which were used for calibration, the energy shift is almost zero. This is because the entrance window effect is not considered in the process of calibration and the measured peak maxima are assumed to correspond to the applied voltage to the spectrometer. Therefore, only energies below $20\,\text{keV}$ are considered in the investigation of the energy shift. For those energies, the energy shift increases for decreasing incident energy for both regions of the detector. The difference between the region with worse energy resolution and the region with better energy resolution increases as well for decreasing incident energy. While for $14\,\text{keV}$, both regions perform quite similarly, for lower incident energies, the energy shift for pixels inside the region with worse energy resolution is significantly larger than for pixels inside the region with better energy resolution. This behaviour is in agreement with the expectation from a thicker entrance window on one part of the detector and is also observed in $^{83\text{m}}\text{Kr}$ measurements, see [53].

As shown in figure 7.3, no half moon shaped region of worse energy resolution was observed for measurements with photons in the MoS and at the MPP, since photons are less sensitive to entrance window effects. However, during an investigation of the ratio of the counts in the peak shoulder compared to the counts in the peak, this structure was also observed. More details can be found in [53]. This observation is also consistent with a thicker entrance window on one part of the detector, as photons deposit their energy almost point-like inside the detector. Most of the photons deposit their entire energy in the sensitive detector volume and only a small fraction of them is affected by the entrance window. Although all investigations up to the date of this thesis point to a thicker entrance window on one part of the detector, this effect and its origin are still under investigation.

7.4 Summary

A first test of in situ energy calibration methods has been performed in the MoS, revealing that a rough energy calibration is possible using wall electrons. Nevertheless, there are limitations of this calibration. For future tests and the final TRISTAN detector system, an energy calibration method with photons over a large energy range is needed.

The measurements with wall electrons show the first electron data captured with the 166-pixel TRISTAN detector module in a MAC-E filter environment similar to the KATRIN experiment. However, an energy dependent inhomogeneity in the detector performance was observed in electron measurements in form of a region on the detector with better energy resolution and a half moon shaped region with worse energy resolution. This inhomogeneity was confirmed in investigations of the shape of the electron energy spectra and the energy shift of the peaks in the energy

spectra. All performed investigations point to a thicker entrance window in the region on the detector which expresses a worse energy resolution compared to the rest of the detector.

Nevertheless, it was shown that a mean energy resolution below $300\,\text{keV}$ at an incident electron energy of $20\,\text{keV}$ and a peaking time of $t_{\text{peak}} = 2\,\mu\text{s}$ is possible even with increased entrance window effects. For the detector region with better energy resolution, an energy resolution of $E_{\text{FWHM}} \leq 330\,\text{keV}$ in an incident energy range of $10\,\text{keV} \leq E_{e^-} \leq 32\,\text{keV}$ can be achieved for a peaking time of $t_{\text{peak}} = 2\,\mu\text{s}$.

Chapter 8

Noise Investigations

A crucial requirement for the final TRISTAN detector is an excellent energy resolution of about $\Delta E_{\mathrm{FWHM}} \approx 300\,\mathrm{eV}$ at electron energies of $20\,\mathrm{keV}$ [36]. The Fano limit provides an irreducible lower limit on the energy resolution for semiconductor detectors. However, the energy resolution increases through noise contributions of the readout electronics and the setup. The MoS provides a MAC-E filter environment similar to the KATRIN beamline. To test the noise characteristics of the detector module in this realistic environment, the noise performance will be investigated in this chapter.

The noise behaviour of the detector system, which is closely connected to the detector energy resolution, can be investigated in either the time or the frequency domain. A complete picture of the electronic noise of the system can be seen in the frequency domain in form of a noise power density spectrum. This is achieved by applying a Fourier transformation on raw waveform data, changing from the time domain to the frequency domain. As events would distort the noise power density, waveform data without events is used for this analysis. The distortions due to the resets in the waveforms are averaged out. For investigations of the noise performance in the time domain listwave data is used. This is in general more intuitive as it directly correlates to the detector energy resolution.

The noise analysis is divided in two parts. In section 8.1, the electronic noise for measurements in the MoS is analysed. This is done both in the time and in the frequency domain. In section 8.2, first, a comparison between the noise for photon measurements with ^{55}Fe in the MoS and at the MPP is performed in the time domain. Finally, the noise performance of the detector for $^{83\mathrm{m}}$Kr electrons is investigated.

8.1 Investigation of the Electronic Noise Performance

Electronic noise refers to the baseline noise of the waveform. It is caused by the readout system as well as the setup itself and needs to be controlled in order to achieve good energy resolution. First, the noise density spectra are analysed and compared for the setups at the MPP and in the MoS. In the next step, the electronic

noise is investigated in the time domain to extract the contribution $\sigma_{\mathrm{el.}}$ to the energy resolution of the detector module.

The noise density spectra in the MPP and in the MoS are shown for all pixels in figure 8.1. During the measurement in the MoS, both magnetic fields and an electric potential are applied, while there is no electric or magnetic field present in the setup at the MPP. In both setups, all pixels except pixel 7 show a homogeneous behaviour. Pixel 7 shows a significantly larger noise power density at the MPP setup at frequencies of $10^4 - 10^6$ Hz. This is due to a unstable cable connection, which increased the noise on the waveform. The connection problem was solved for later measurements and was not present at the measurement in the MoS. The general shape of the noise power density spectrum is similar for the setup at the MPP and in the MoS. At high frequencies, the noise density is dominated by a constant voltage noise component. The observed spikes are originating from noise sources, e.g. on the bias system. At low frequencies, the current noise from the detector is dominating. For TRISTAN detectors, the dominating contribution to the current noise is the detector leakage current, which is temperature-dependent. During both measurements, the detector was cooled down to $T_{\mathrm{SDD}} = -29\,^\circ\mathrm{C}$. Therefore, the leakage current is negligible and there is only a small increase in the noise power density at high frequencies.

(a) Noise density spectrum at MPP.   (b) Noise density spectrum in the MoS.
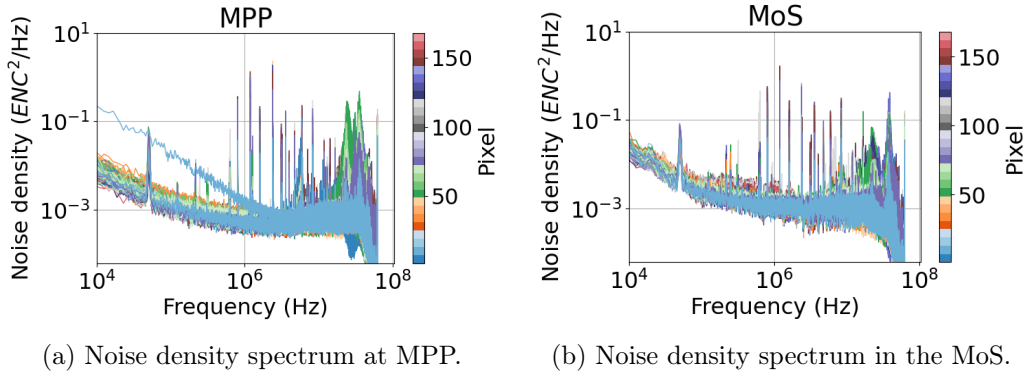
Figure 8.1: Noise power density spectra in (a) the MPP and (b) the MoS for all pixels. In contrast to the MPP, electric and magnetic fields are present in the MoS. In both setups, all pixels behave homogeneously. One exception to the homogeneity is pixel 7 in the MPP setup, which exhibits a significantly higher noise power density at low frequencies due to a bad cable connection. The noise power density at the MPP and in the MoS is very similar and point to a similar detector performance.

As almost all pixels in both setups express a similar noise power density, the resulting noise power densities of one exemplary pixel at the MPP and in the MoS are compared in figure 8.2. The noise power density at the MPP is smaller compared

to the one measured in the MoS for all frequencies. The difference is more pronounced in a frequency range of $10^4 - 10^6$ Hz, which corresponds to increased noise at higher peaking times in the time domain in the MoS. This results from longer cables as well as additional noise sources inside the MoS, e.g. unintentional light sources on the equipment inside the spectrometer. For a more complicated setup like the MoS, this increase in noise is expected. Nevertheless, both measurements are in agreement with the expectation based on previous noise investigations of prototype detectors, see [48], and are comparable to each other. Therefore, the electronic noise is expected to be approximately equal for the MPP setup and the MoS.
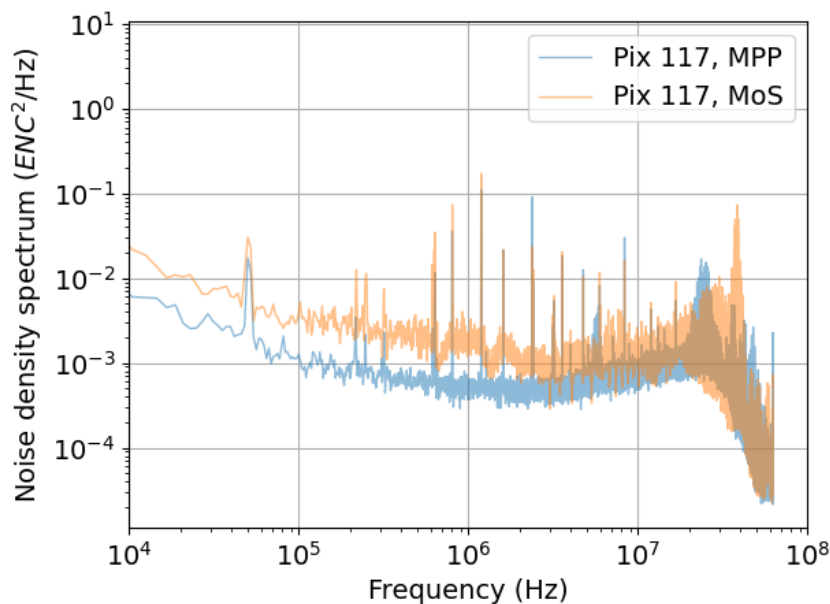
Figure 8.2: Comparison of the noise power density in the MPP setup (blue) and the MoS (orange). While both setups perform similarly at high frequencies, the noise power density of the MoS setup is higher than the MPP one for lower frequencies due to additional noise sources in the MoS.

In electron measurements with the detector module, two regions on the detector with different energy resolutions are observed, see section 7.3. The noise density spectrum can be used to exclude an increased electronic noise for pixels in the region with worse energy resolution as the origin of this effect. For this, a comparison between the mean noise power density of pixels inside the half moon shaped region with worse energy resolution and outside the region is performed. The resulting noise power density spectra can be seen in figure 8.3. There is no difference observed between the mean of noise power density for the pixels inside the region with worse

energy resolution compared to the mean for pixels outside the region. The electronic noise is equal for both regions on the detector and the effect of different energy resolutions on the detector module can not be explained by electronic noise.
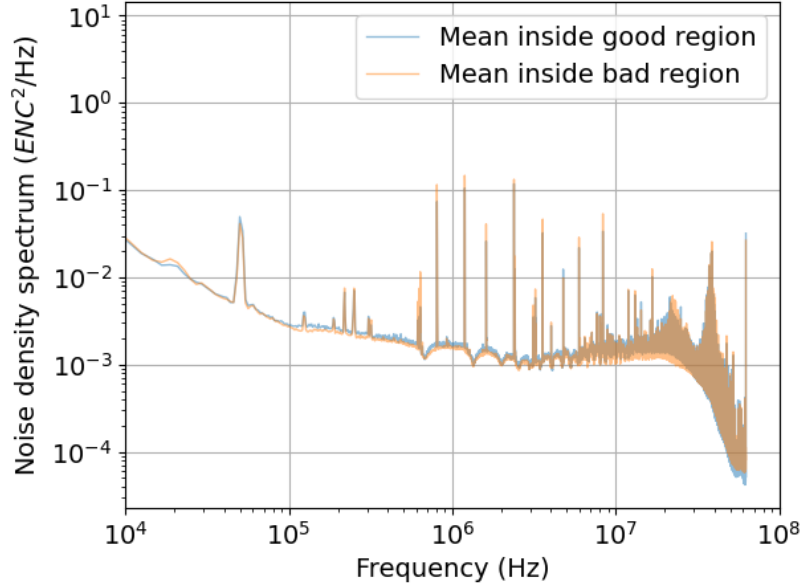
Figure 8.3: Comparison of the mean noise power density for pixels inside the half circle with good energy resolution (blue) and outside (orange). No difference in the noise behaviour of both regions is observed across all frequencies.

To extract quantitative values for the electronic noise contribution $\sigma_{\text{el.}}$, the electronic noise is investigated in the time domain. For this task listwave data of a ^{83m}Kr source in the MoS is used. The measurement was performed at an SDD temperature of $T_{\text{SDD}} = -29\,^{\circ}\text{C}$ in a magnetic field and with a retarding potential of $V_{\text{Ret}} = 30.2\,\text{kV}$ applied to the MoS. In listwave data, $20\,\mu\text{s}$ snippets of the waveform around the event are saved. To extract the electronic noise, only the waveform in the beginning of the wave snippet before the event happens, is used. A manual trigger is applied at the beginning of the waveform and a trapezoidal filter is evaluated for different peaking times at the position of the manual trigger. This way, the filter response to the real electronic noise without events can be reconstructed. A zero peak is visible in the filter response. The position of this zero peak is consistent with $0\,\text{ADC}$. The peak is Gaussian shaped and is fitted in the next step by a Gaussian function. The energy resolution can be extracted from the variance σ of the fit and is plotted against the peaking time of the trapezoidal filter. The electronic noise curve is shown in figure 8.4 for all pixels.
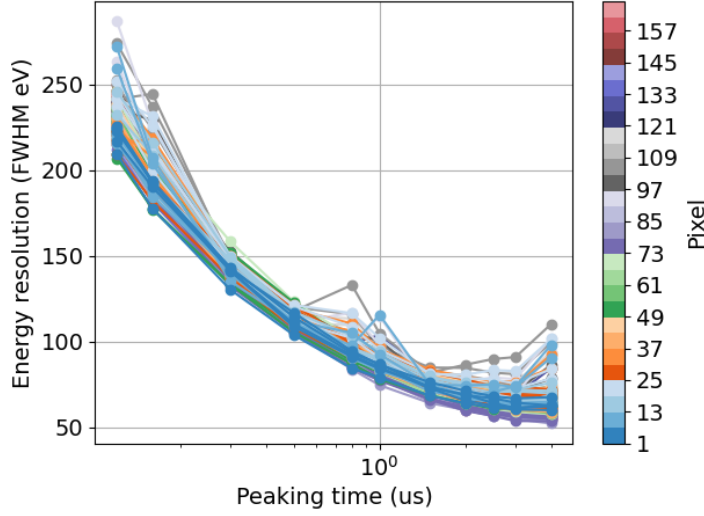
Figure 8.4: The energy resolution resulting from purely electronic noise is plotted against the peaking time of the trapezoidal filter. The measurement was performed in magnetic and electric fields in the MoS. All pixels are homogeneous and show the expected behaviour. There is a slight degradation at high peaking times around 4 µs. This is due to additional noise contributions in the MoS. Some slight outliers are attributed to an unstable fit.

All pixels express a homogeneous behaviour with only a few slight outliers, that are attributed to an unstable fit. At low peaking times, the contribution from the voltage noise is dominant and results in a worse energy resolution. For higher peaking times, the energy resolution is dominated by the current noise. The main contribution to the current noise in the TRISTAN detector module is the leakage current, which is negligible for low temperatures. Therefore, the energy resolution improves for longer peaking times. An electronic noise contribution of $\Delta E_{\mathrm{FWHM}} = 67\,\mathrm{eV}$, which corresponds to $\sigma_{\mathrm{el.}} = 7.6\,\mathrm{ENC}$, is found at a peaking time of $2\,\mathrm{µs}$. Since the noise power densities are very similar at the MPP and in the MoS for almost all pixels, this value is expected to hold approximately for both setups and both in the region with better energy resolution and the region with worse energy resolution. The homogeneous behaviour of all pixels is in agreement with the homogeneity of the pixels in the noise power density investigation in the frequency domain.

8.2 Investigation of the Total Detector Noise Performance

A noise curve of physical events can be investigated as a measure of the total noise performance of the TRISTAN detector, as it includes all effects that influence the energy resolution, including possible detector effects. In the following, this is shown for 5.9 keV photons emitted from a ^{55}Fe source and for electrons emitted from an ^{83m}Kr source.

8.2.1 Noise Performance for Photons

The noise performance analysis for 5.9 keV photons emitted from a ^{55}Fe source was performed both in the MPP setup and in the MoS. During both measurements, the detector was cooled down to $T_{\mathrm{SDD}} \approx -29\,^{\circ}\mathrm{C}$ and neither magnetic fields nor electric fields were applied. For the analysis, listwave data was taken and analysed offline with a trapezoidal filter for different peaking times. The spectra are calibrated with the Mn-K$_\alpha$ and Mn-K$_\beta$ peaks, which are fitted with a Gaussian function and a shelf term. Only the energy resolution of the Mn-K$_\alpha$ peak is considered in the resulting noise curves for all pixels, which can be seen in figure 8.5.
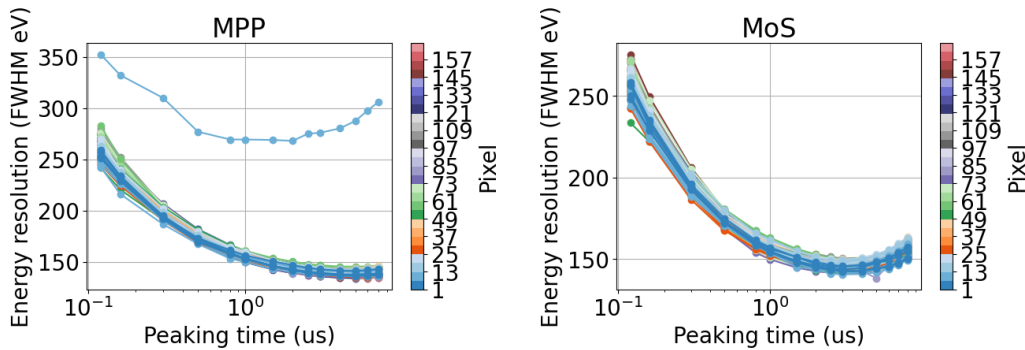
(a) Noise curve of ^{55}Fe events at the MPP. (b) Noise curve of ^{55}Fe events in the MoS.

Figure 8.5: Energy resolution of an ^{55}Fe spectrum against the peaking time of the offline trapezoidal filter for all pixels. In both setups, the detector was cooled to $T_{\mathrm{SDD}} \approx -29\,^{\circ}\mathrm{C}$. Both measurements were done in absence of magnetic and electric fields. All pixels express a homogeneous behaviour in both setups, except for pixel 7 at the MPP. A bad cable connection results in additional noise for this pixel, which was fixed in later measurements. For the MoS data, the energy resolution deteriorates for high peaking times. This is due to additional noise sources inside the MoS.

In both setups, all pixels are homogeneous. The single exception to this is pixel 7 at the MPP setup, which has a significantly worse energy resolution across all peaking times. This is in agreement with the noise power density shown in section 8.1. The origin of this behaviour is a bad cable connection on the vacuum-side of the setup and was fixed in later measurements. In addition, both setups show a small spread of the energy resolution for the individual pixels of less than 13 eV at peaking times > 0.3 µs. At short peaking times, voltage noise dominates and results in a worse energy resolution. For a cooled detector, the leakage current is negligible, therefore the energy resolution is expected to improve for high peaking times. This can be seen for both setups. However, in the MoS, additional noise contributions cause a degradation of the energy resolution for high peaking times. Those noise sources are e.g. unintentional light sources inside the spectrometer as well as longer cables.

A comparison of the median of both noise curves and the expectation from the electronic noise investigation is shown in figure 8.6.
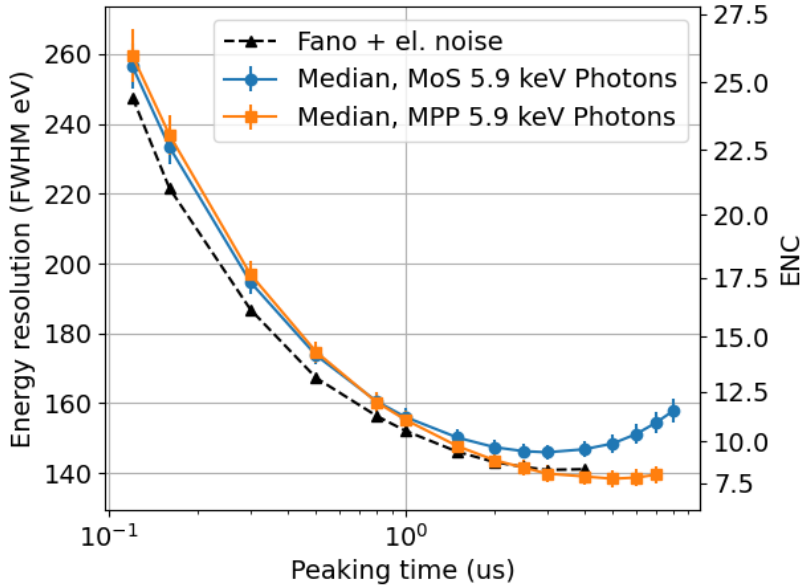
Figure 8.6: Comparison of the median of both photon noise curves at the MPP (orange) and in the MoS (blue). The expectation from the electronic noise investigation (black) is obtained by correcting the extracted electronic noise with the Fano contribution and is in good agreement with both noise curves. The energy resolution is better for the detector in the MPP setup than in the MoS for high peaking times due to additional noise components in the MoS.

Note that because the electronic noise is extracted from listwave data, only peaking times up to $4\,\mu s$ could be obtained. The extracted variance $\sigma_{\mathrm{el.}}$ of the electronic noise is corrected with the expected Fano contribution to obtain the expected energy resolution at $E_\gamma = 5.9\,\mathrm{keV}$, as described by equation 3.1. Both results are in good agreement with the expectation from the electronic noise investigation and the TRISTAN detector module performance in the MoS is comparable with the performance at the MPP. However, the additional noise sources in the MoS result in a worse energy resolution especially for high peaking times compared to the MPP setup. For the MoS, an optimum is found for $E_\gamma = 5.9\,\mathrm{keV}$ at a peaking time of $3\,\mu s$ with a median energy resolution of $\Delta E_{\mathrm{FWHM}} = 146\,\mathrm{eV}$. At the MPP, the median energy resolution at $3\,\mu s$ peaking time amounts to $\Delta E_{\mathrm{FWHM}} = 140\,\mathrm{eV}$.

8.2.2 Noise Performance for Electrons

The effect of two regions on the detector with different energy resolution was observed most pronounced in measurements with electrons. To investigate the total noise including detector effects for electrons, noise curves for electrons are investigated. To this end, listwave data containing events of the L32-line of a ^{83m}Kr source was taken. In the measurement, a magnetic field and a retarding potential of $V_{\mathrm{Ret}} = 30.2\,\mathrm{kV}$ was applied. The data is analysed with a manual trapezoidal filter for different peaking times. The resulting spectra are calibrated with the means of the L32- and M32-line and the L32-peak was fitted with the electron response function, see eq. 5.4. The resulting noise curve for all pixels is shown in figure 8.7.

While all pixels show a similar shape of the noise curve, the spread of the energy resolution of the individual pixels amounts to $59 - 63\,\mathrm{eV}$ and is therefore significantly larger than for the noise curves obtained from photon events or electronic noise. This is in agreement with the observation of a region with worse energy resolution on the detector, which is present both in wall electron measurements and measurements of conversion electrons of a ^{83m}Kr source. In addition, pixel 163 shows a worse energy resolution across all peaking times than the rest of the pixels. This is assumed to be due to an additional entrance window effect for this specific pixel. The origin of this additional effect is under investigation. The overall shape of the noise curve for electrons is similar to the one for photons as well as for electronic noise but shifted to worse energy resolutions. Again, an additional current noise contribution is seen for high peaking times, which leads to a degradation of the energy resolution. This is assumed to be caused by e.g. unintentional light sources originating from equipment inside the spectrometer. An optimum of $\Delta E_{\mathrm{FWHM}} = 348\,\mathrm{eV}$ at $E_{\mathrm{e}^-} = 30.4\,\mathrm{keV}$ is found for a peaking time of $t_{\mathrm{peak}} = 3\,\mu s$.
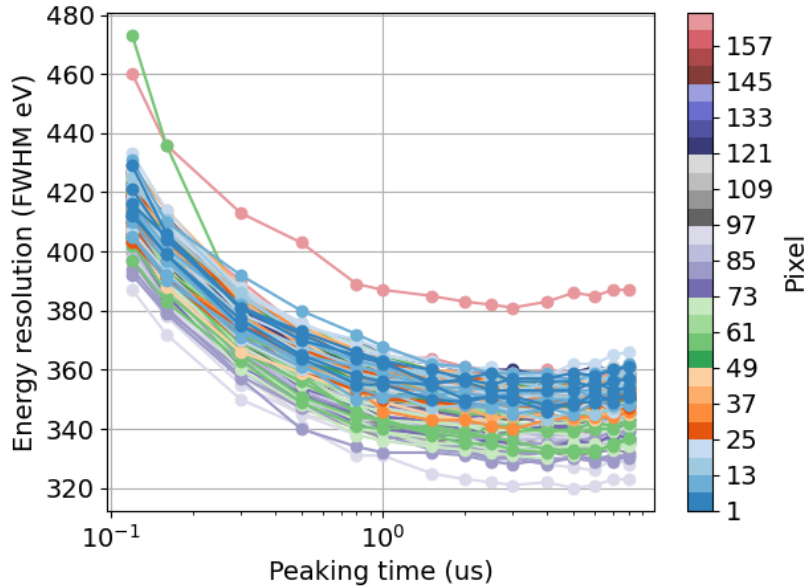
Figure 8.7: Noise curve for a ^{83m}Kr measurement at the MoS for all pixels. The spread of the pixels for all peaking times is significantly larger compared to measurements with photons. Due to an additional entrance window effect for pixel 163, this pixel shows significantly worse energy resolutions for all peaking times. The general shape of the noise curve is in agreement with the expectation from photon and electronic noise curves.

To check for additional noise contributions that are not caught in the electronic noise, a comparison between the expected noise curve from the electronic noise investigation corrected with the Fano limit and the measured noise curves for electrons is performed. For this, the measured noise curve is divided into the median noise curve for pixels in the region with better energy resolution and the median noise curve of pixels in the region with worse energy resolution. This can be seen in figure 8.8. The general shape of the three curves is similar, however, there is an offset between the measurements and the expectation. This offset is smaller for the region with better energy resolution than for the region with worse energy resolution and does not depend on the peaking time. The difference between the expectation and the measurement amounts to $47-55$ eV for the region with better energy resolution and $62-66$ eV for the region with worse energy resolution. This is in agreement with the hypothesis that the region with worse energy resolution has a thicker entrance window compared to the region with better energy resolution. Since the entrance

window effect is a detector effect which only affects physical events and especially electrons, this is not included in the electronic noise or the Fano contribution.
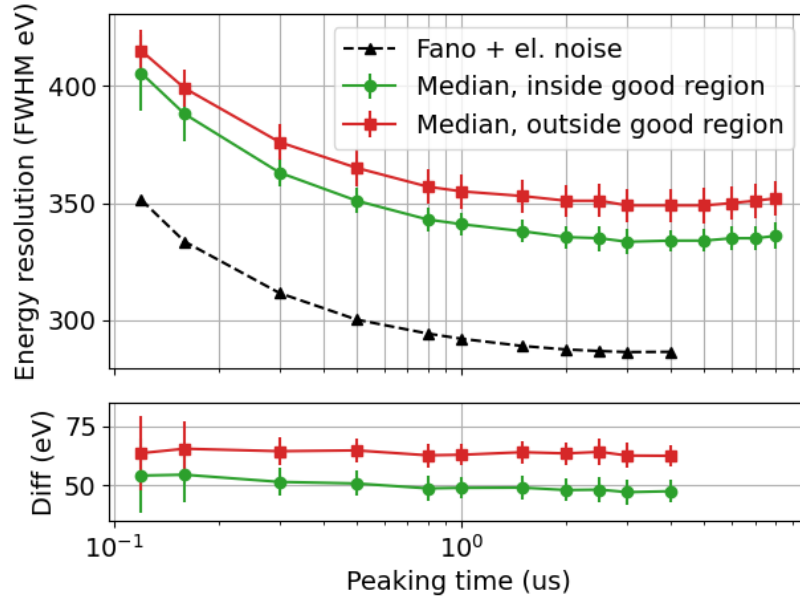
Figure 8.8: Upper panel: Comparison of the median of the electron noise curve at the MoS for the region with good (green) and worse (red) energy resolution with the expectation from the electronic noise investigation (black). The two detector regions with different energy resolutions are clearly separated. The shape of the two measured and expected noise curves are similar. An offset between the three curves is observed. Lower panel: The difference of the measured noise curve and the expected noise curve from the electric noise contribution corrected with the Fano limit for 30.4 keV electrons is plotted against the peaking time of the trapezoidal filter. For both regions, the result is approximately flat, no dependence on the peaking time is observed.

8.3 Summary

In the first step, the electronic noise performance of the 166-pixel TRISTAN detector module was investigated in the MoS. The noise performance is homogeneous over the whole detector and is comparable for the MoS and the dedicated laboratory test stand at the MPP. However, at low frequencies, which correspond to high peaking times,

a higher noise is observed in the MoS. This is due to longer cables and additional noise sources at the MoS.

This behaviour is also seen in the noise investigation using a ^{55}Fe source. The noise performance of the detector in the MoS and in the laboratory test stand at the MPP is comparable and agrees with the expectation from the electronic noise investigations.

In the last step, the noise performance of the detector was investigated using a ^{83m}Kr source. Here, the noise performance is significantly worse than expected from the electronic noise investigation. This is due to the entrance window effect, which is more pronounced for electrons than for photons. A region on the detector is observed, in which the noise performance is worse compared to the rest of the detector. This is in agreement with the wall electron analyses and further hints towards a thicker entrance window on one part of the detector.

Chapter 9

Conclusion

Sterile neutrinos are a minimal extension of the Standard Model of Particle Physics. If they have a mass in the order of keV, they are promising Dark Matter candidates. Via the mixing with active neutrinos, they would leave an imprint in the spectra of weak decays such as the tritium beta-decay. The KATRIN experiment uses a strong and stable tritium source to investigate the effective electron antineutrino mass in the beta-decay spectrum. After the measurement campaign for the neutrino mass, the KATRIN experiment will be used to search for the characteristic kink-like signature of a sterile neutrino in the beta-decay spectrum. For this task, the current KATRIN detector is not suited and therefore a novel TRISTAN silicon drift detector and read-out system is currently under development. The TRISTAN detector will consist of 9 and later possibly 21 166-pixel TRISTAN detector modules.

In this thesis, a 166-pixel TRISTAN detector module was characterised in a realistic MAC-E filter environment of the KATRIN Monitor Spectrometer for the first time. To this end, the detector has been commissioned first in a dedicated test stand at the Max-Planck Institute for Physics. Two DAQ systems were investigated for the commissioning and characterisation: The CAEN DAQ system, consisting of three synchronized VX2470B cards, and the custom-made Athena DAQ system, which was developed and produced by Politecnico di Milano. Spectra acquired with the Athena DAQ showed unphysical distortions in some pixels. In addition, connection problems occurred. Furthermore, the mean detector energy resolution was found to be better for the CAEN DAQ system. For these reasons, the CAEN DAQ system was chosen for all subsequent measurements.

All relevant detector voltages were varied in systematic sweeps to find an optimal working point in terms of functionality of pixels, energy resolution, count rate stability and calibration stability. A narrow working point was found, where all pixels work reliably. An overall median energy resolution of $\overline{\Delta E_{\mathrm{FWHM}}} = 146\,\mathrm{eV}$ at $5.9\,\mathrm{keV}$ for a peaking time of $t_{\mathrm{peak}} = 2\,\mathrm{\mu s}$ was found. This corresponds to an improvement of $9\,\mathrm{eV}$ compared to the energy resolution of a detector at non-optimized voltages.

For a reliable commissioning inside the KATRIN Monitor Spectrometer, a calibration arm was purchased and a corresponding source holder for an ^{55}Fe source was designed and manufactured. In September 2022, the calibration equipment and the 166-pixel TRISTAN detector module were successfully installed in the KATRIN Monitor Spectrometer. The commissioning with an ^{55}Fe source revealed a median energy resolution of $\overline{\Delta E_{\mathrm{FWHM}}} = 151\,\mathrm{eV}$ at 5.9 keV for a peaking time of $t_{\mathrm{peak}} = 2\,\mu\mathrm{s}$, which is comparable to the detector performance at the test stand at the MPP. This shows that the detector can be operated with almost no performance loss in a more realistic environment.

For the first time, electrons were measured with a 166-pixel TRISTAN detector module in a realistic environment. This thesis focuses on the measurements with wall electrons of different energies. A median energy resolution of $\overline{\Delta E_{\mathrm{FWHM}}} = 285\,\mathrm{eV}$ at 20 keV was found for a peaking time of $t_{\mathrm{peak}} = 2\,\mu\mathrm{s}$. Despite the observation of a half moon shaped area on the detector, in which the energy resolution was worse compared to the rest of the detector module, the module meets the requirement of $\Delta E_{\mathrm{FWHM}} \approx 300\,\mathrm{eV}$ at 20 keV. The difference of the energy resolution inside and outside this region was energy dependent and increased with decreasing incident energy. This effect was also observed in measurements with $^{83\mathrm{m}}$Kr conversion electrons. For low incident energies, the spectra of the pixels inside the region with worse energy resolution were distorted. In addition, the peaks in the electron spectra experienced a shift of the peak energy, which was again energy dependent and increased for decreasing incident energies. These observations point to an additional layer on the surface of the detector being the reason for the degradation of the pixel performance. A later measurement outside the MoS confirmed this hypothesis.

The third focus of this thesis was the noise investigation of the 166-pixel TRISTAN detector module both at the test stand at MPP and in the KATRIN Monitor Spectrometer. The electronic noise behaviour for all pixels was found to be homogeneous. A median electronic noise contribution of $\overline{\Delta E_{\mathrm{FWHM}}} = 62\,\mathrm{eV}$, which corresponds to $\sigma_{\mathrm{el.}} = 7\,\mathrm{ENC}$, was found for a peaking time of $t_{\mathrm{peak}} = 3\,\mu\mathrm{s}$. The detector performed slightly better in the MPP setup at low frequencies, corresponding to high peaking times, than in the KATRIN Monitor Spectrometer. However, the performance in both setups was comparable. For ^{55}Fe photons at $E_{\gamma} = 5.9\,\mathrm{keV}$, an optimum of $\overline{\Delta E_{\mathrm{FWHM}}} = 146\,\mathrm{eV}$ for the KATRIN Monitor Spectrometer was found for a peaking time of $t_{\mathrm{peak}} = 3\,\mu\mathrm{s}$. This is in agreement with the expectation from the electronic noise investigation. In contrast, for electrons, the energy resolution is not limited by the noise performance, but by losses in the insensitive entrance window region. Accordingly, the noise curves have the same shape, but are shifted to higher values. An offset of $47 - 55\,\mathrm{eV}$ is found for the region with better energy resolution and

$62 - 66\,\mathrm{eV}$ for the region with worse energy resolution.

The commissioning and characterisation of the first 166-pixel TRISTAN detector module is a major milestone for the development of the final TRISTAN detector and shows the feasibility of operating a large silicon drift detector array in a complicated magnetic- and electric field environment while maintaining a very good energy resolution. This work lays the foundation for the characterisation of future detector modules and serves as a basis for further investigations of the entrance window of TRISTAN detector modules.

Appendix A

Conversion Electrons in ^{83m}Kr-Decay

Table A.1: Conversion electrons in ^{83m}Kr-decay [59].

	Energy (keV)	Internal conversion coefficient	Intensity per decay
γ 9.4057			
L_1	7.4811	12.1	0.668
L_2	7.6737	1.34	0.0747
L_3	7.7264	1.03	0.0570
M_1	9.1129	2.00	0.108
M_2	9.1835	0.220	0.0119
M_3	9.1911	0.166	0.008 97
M_4	9.3106	0.003 24	0.000 175
M_5	9.3119	0.002 90	0.000 156
N_1	9.3781	0.247	0.011
N_2	9.3910	0.0197	0.000 88
N_3	9.3916	0.0146	0.000 655
γ 32.1516			
K	17.8242	478.0	0.248
L_1	30.2268	31.7	0.0156
L_2	30.4195	492.0	0.243
L_3	30.4722	766.0	0.378
M_1	31.8587	5.19	0.002 49
M_2	31.9293	83.7	0.0402
M_3	31.9369	130.0	0.0624
M_4	32.0564	1.31	0.000 628
M_5	32.0576	1.84	0.000 884
N_1	32.1239	0.643	0.000 255
N_2	32.1367	7.54	0.003 00
N_3	32.1374	11.5	0.004 57

Appendix B

Supplementary Plots for Detector Voltage Optimisation

B.1 JFET Parameters

The JFET current V_{SSS}, which is more intuitively understood via the drain current I_{D} per channel, has no significant effect on the energy resolution, the total count rate, the peak position of the Mn-K$_\alpha$ peak and the spectrum, see figure B.1. An optimal value of $I_{\text{D}} = 200\,\mu\text{A}$ is determined, which is achieved by $V_{\text{SSS}} = -3.9\,\text{V}$.

The drain voltage V_{D} has a significant effect on the detector performance. For too high and too low values, the energy resolution deteriorates and for too high values, spectral distortions appear. The detection efficiency and peak position of the Mn-K$_\alpha$ peak is stable over the investigated range. This can be seen in figure B.2. The drain voltage $V_{\text{D}} = 7.5\,\text{V}$ is used for all subsequent measurements.

B.2 Reset Parameters

For reasonable values of the reset parameters V_{ResH}, V_{ResL} and T_{Reset}, no significant effect is observed on the energy resolution, the count rate as well as the peak position of the Mn-K$_\alpha$ peak and the spectrum, as expected. The individual plots are depicted in figures B.3, B.4, and B.5. Values of $V_{\text{ResH}} = 4\,\text{V}$, $V_{\text{ResL}} = -10\,\text{V}$ and $T_{\text{Reset}} = 1.5\,\mu\text{s}$ are used for all subsequent measurements.
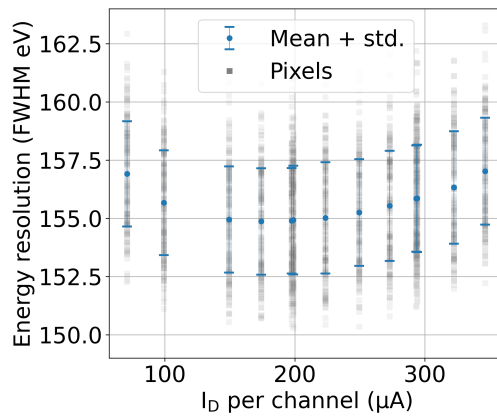
(a) Effect of I_D on the energy resolution.
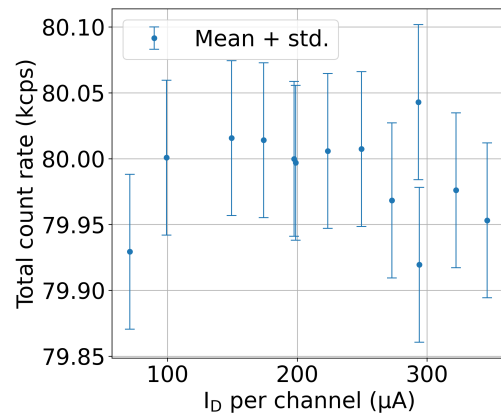
(b) Effect of I_D on the count rate.
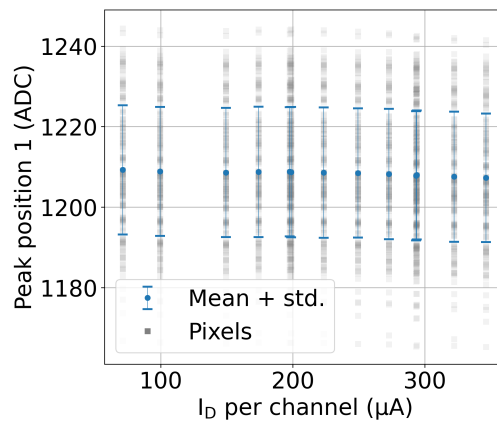
(c) Effect of I_D on the peak position.
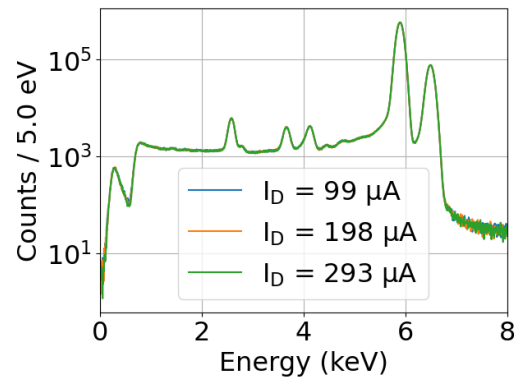
(d) Effect of I_D on the spectrum.

Figure B.1: Impact of I_D on the detector performance. I_D has no significant impact on (a) the energy resolution, (b) the total count rate, (c) the peak position of the first peak and (d) the spectrum. Adapted from [53].
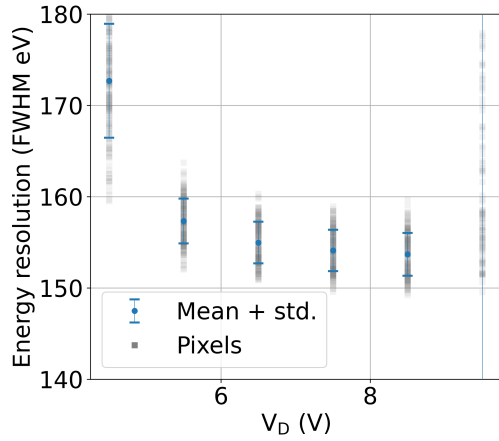
(a) Effect of V_D on the energy resolution.
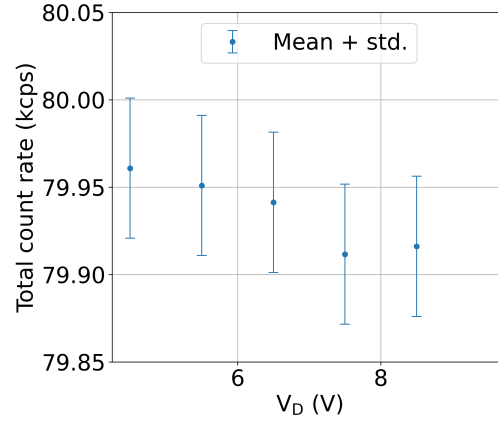
(b) Effect of V_D on the count rate.
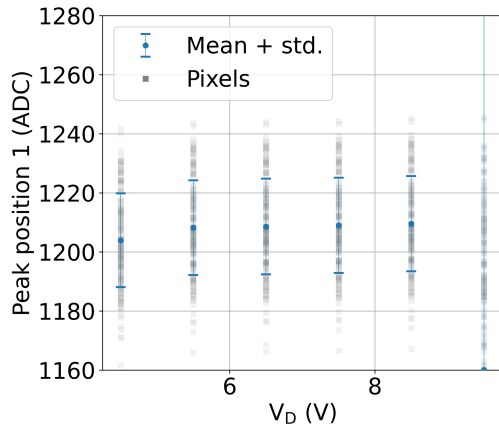
(c) Effect of V_D on the peak position.
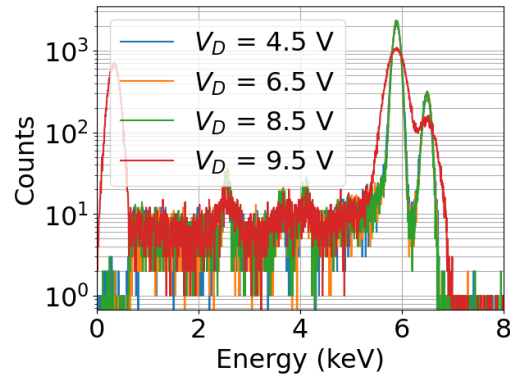
(d) Effect of V_D on the spectrum.

Figure B.2: Impact of V_D on the detector performance. (a) The energy resolution is stable for $6\,\mathrm{V} < V_D < 8.5\,\mathrm{V}$. V_D has no significant impact on (b) the total count rate and (c) the peak position of the Mn-K$_\alpha$ peak. However, for too high values of V_D, (d) the spectrum becomes distorted. Adapted from [53].
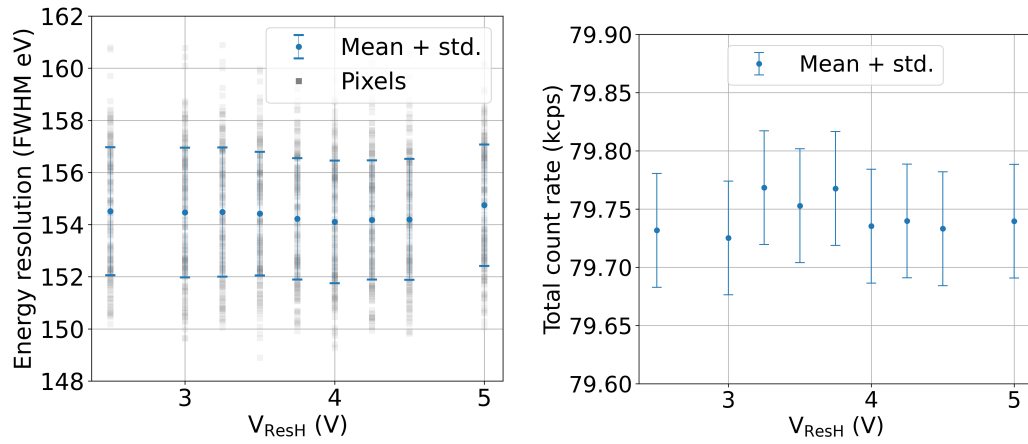
(a) Effect of V_{ResH} on the energy resolution.

(b) Effect of V_{ResH} on the count rate.
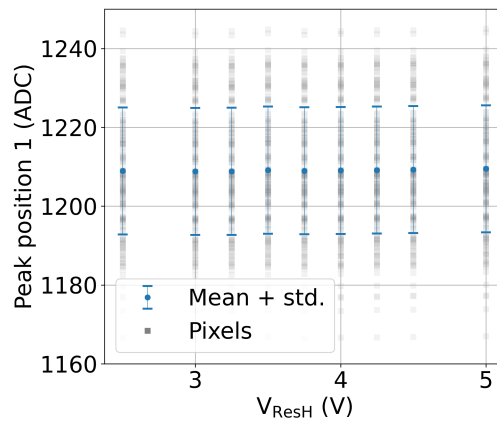
(c) Effect of V_{ResH} on the peak position.

Figure B.3: Impact of V_{ResH} on the detector performance. V_{ResH} has no impact on (a) the energy resolution, (b) the total count rate and (c) the peak position of the Mn-K$_\alpha$ peak. Adapted from [53].
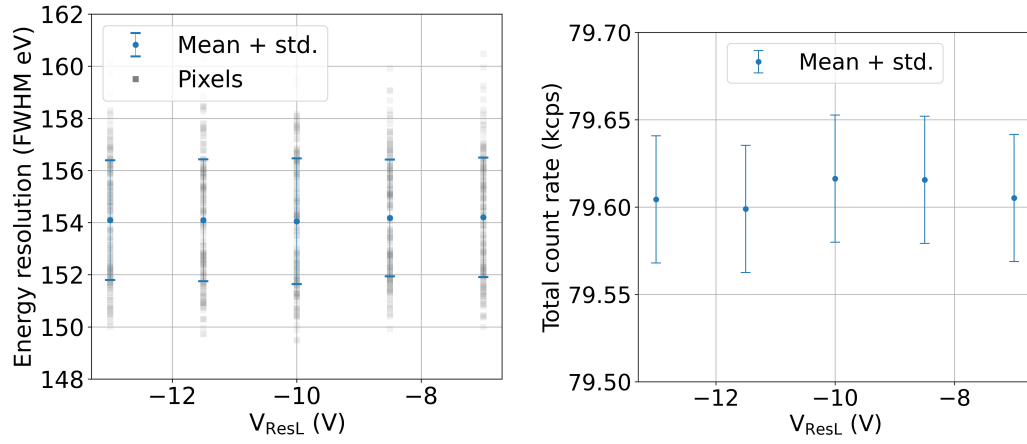
(a) Effect of V_{ResL} on the energy resolution.

(b) Effect of V_{ResL} on the count rate.
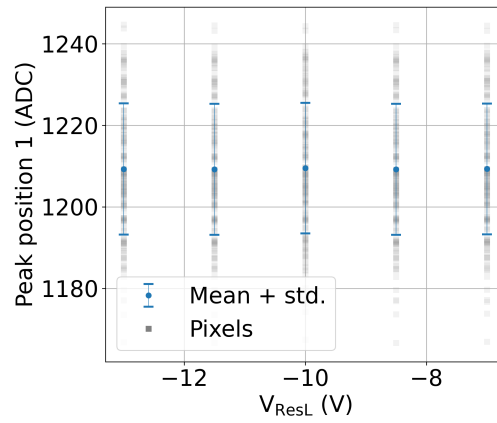
(c) Effect of V_{ResL} on the peak position.

Figure B.4: Impact of V_{ResL} on the detector performance. V_{ResL} has no impact on (a) the energy resolution, (b) the total count rate and (c) the peak position of the Mn-K_α peak. Adapted from [53].

(a) Effect of T_{Reset} on the energy resolution.

(b) Effect of T_{Reset} on the count rate.

(c) Effect of T_{Reset} on the peak position.

(d) Effect of T_{Reset} on the spectrum.

Figure B.5: Impact of T_{Reset} on the detector performance. T_{Reset} has no impact on (a) the energy resolution, (b) the total count rate, (c) the peak position of the Mn-K_{α} peak and (d) on the spectrum. Adapted from [53].

B.3 Back Contact, Ring 1 and Ring X Voltages

The back contact voltage V_{BC}, ring 1 voltage V_{R1} and ring X voltage V_{RX} have a strong impact on the detector performance. V_{BC} is varied in combination with V_{R1}. Additionally, sweeps over V_{R1} and V_{RX} are performed at different V_{IGR}. The impact of those parameters and combinations are depicted in figures B.6, B.7, B.8 and B.9.

Voltage combinations, where one or more pixels are non-functional or heavily distorted, are depicted in grey. For voltage combinations, where all pixels are functional, no significant effect on the energy resolution, the count rate and the peak position of the Mn-K$_\alpha$ peak is observed. However, the working point of the detector becomes narrower for more negative V_{IGR}. For all subsequent measurements, $V_{\text{BC}} = -115\,\text{V}$, $V_{\text{BF}} = -125\,\text{V}$, $V_{\text{R1}} = -10\,\text{V}$ and $V_{\text{RX}} = -120\,\text{V}$ are used.

B.4 Inner Guard Ring Voltages

A non-optimized inner guard ring voltage can lead to charge losses and therefore undesirable spectral effects. There is no significant effect on the energy resolution, the count rate and the peak position of the Mn-K$_\alpha$ peak. However, low-energy shoulders appear on the peaks in the spectrum for too positive V_{IGR}, see figure B.10. For all subsequent measurements, $V_{\text{IGR}} = -20\,\text{V}$ is used.
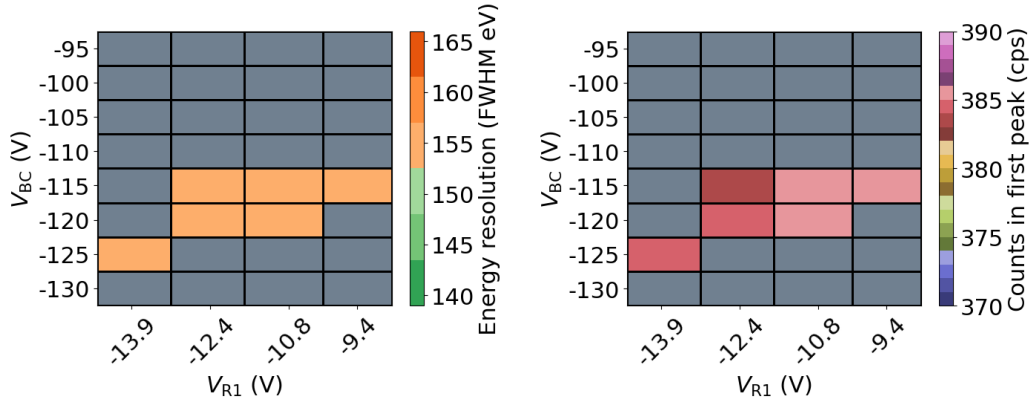
(a) Effect on the energy resolution.

(b) Effect on the count rate.
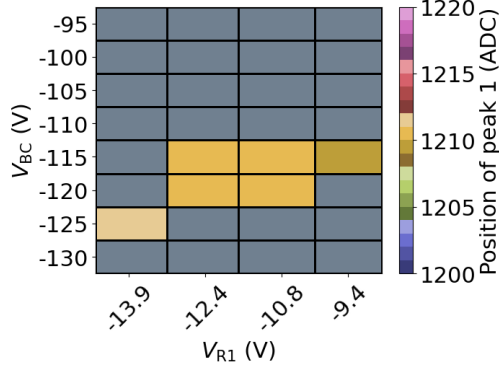
(c) Effect on the peak position.

Figure B.6: Impact of V_{BC} at different V_{R1} on the detector performance. Voltage combinations, where one or more pixels are non-functional or distorted, are depicted in grey. Inside the narrow working point, no significant effect on (a) the energy resolution, (b) the count rate and (c) the peak position of the Mn-K_α peak is observed.

(a) Effect on the energy resolution.

(b) Effect on the count rate.

(c) Effect on peak position
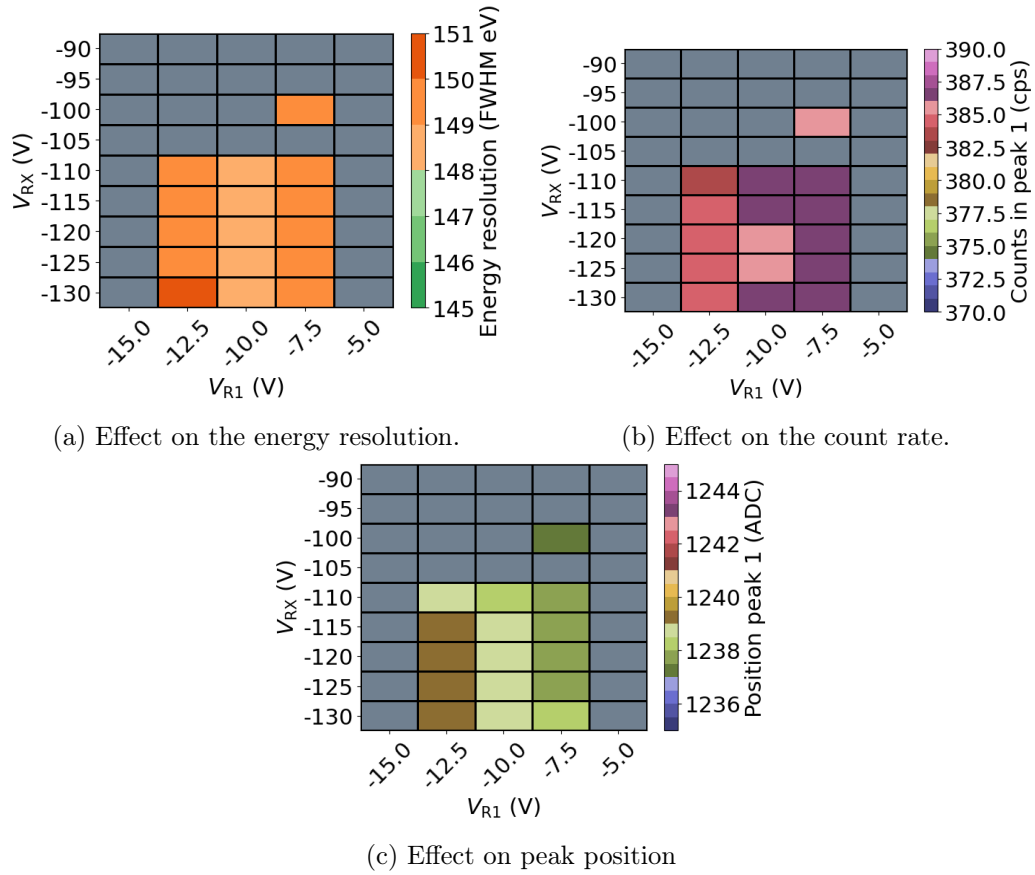
Figure B.7: Impact of V_{RX} at different V_{R1} on the detector performance at $V_{IGR} = -20\,\text{V}$. Voltage combinations, where one or more pixels are non-functional or distorted, are depicted in grey. Inside the narrow working point, no significant effect on (a) the energy resolution, (b) the count rate and (c) the peak position of the Mn-K_α peak is observed.

(a) Effect on the energy resolution.

(b) Effect on the count rate.

(c) Effect on the peak position.
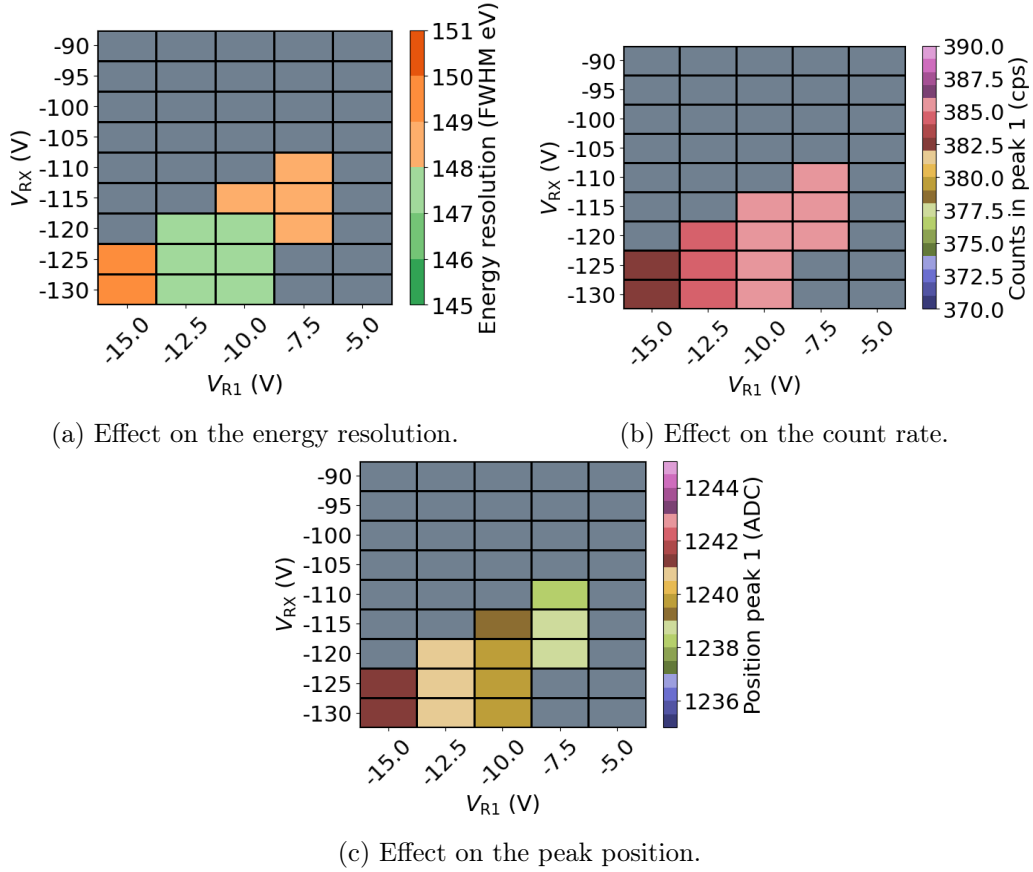
Figure B.8: Impact of V_{RX} at different V_{R1} on the detector performance at $V_{\mathrm{IGR}} = -25\,\mathrm{V}$. Voltage combinations, where one or more pixels are non-functional or distorted, are depicted in grey. Inside the narrow working point, no significant effect on (a) the energy resolution, (b) the count rate and (c) the peak position of the Mn-K$_\alpha$ peak is observed.

(a) Effect on the energy resolution.

(b) Effect on the count rate.

(c) Effect on the peak position.
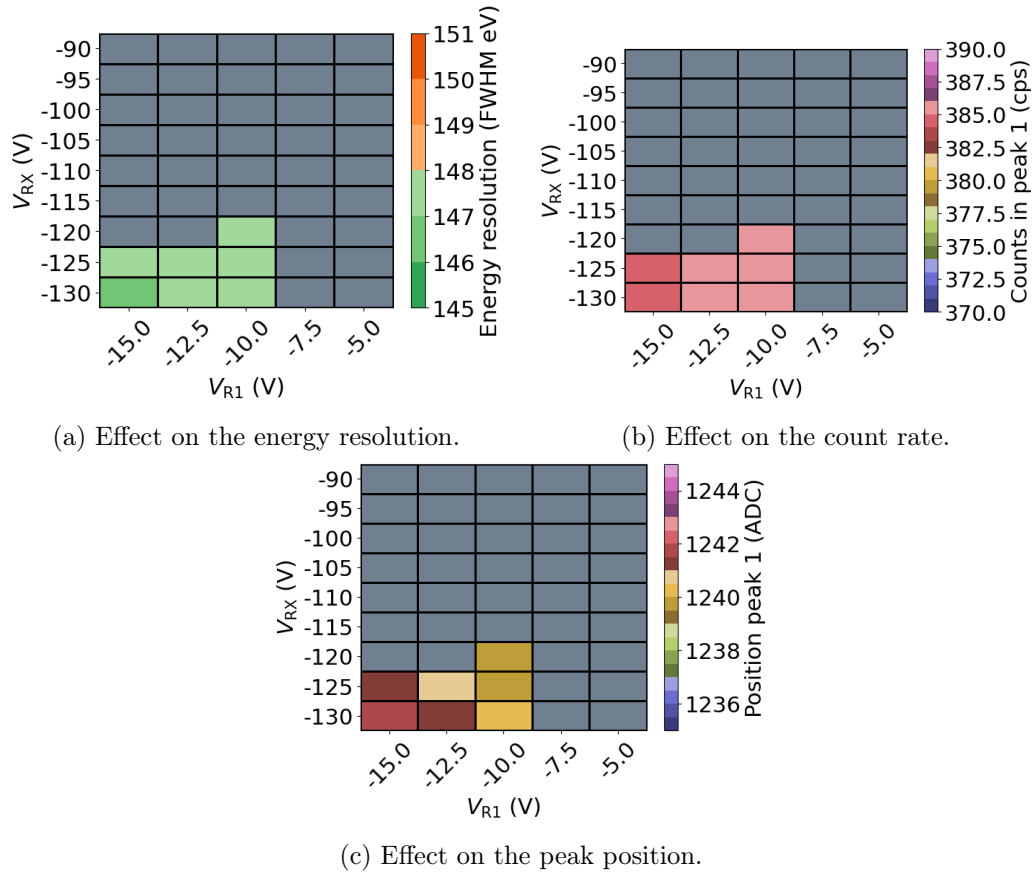
Figure B.9: Impact of V_{RX} at different V_{R1} on the detector performance at $V_{IGR} = -30\,V$. Voltage combinations, where one or more pixels are non-functional or distorted, are depicted in grey. Inside the narrow working point, no significant effect on (a) the energy resolution, (b) the count rate and (c) the peak position of the Mn-K_α peak is observed.

(a) Effect of V_{IGR} on the energy resolution.

(b) Effect of V_{IGR} on the count rate.

(c) Effect of V_{IGR} on the peak position.

(d) Effect of V_{IGR} on the spectrum.
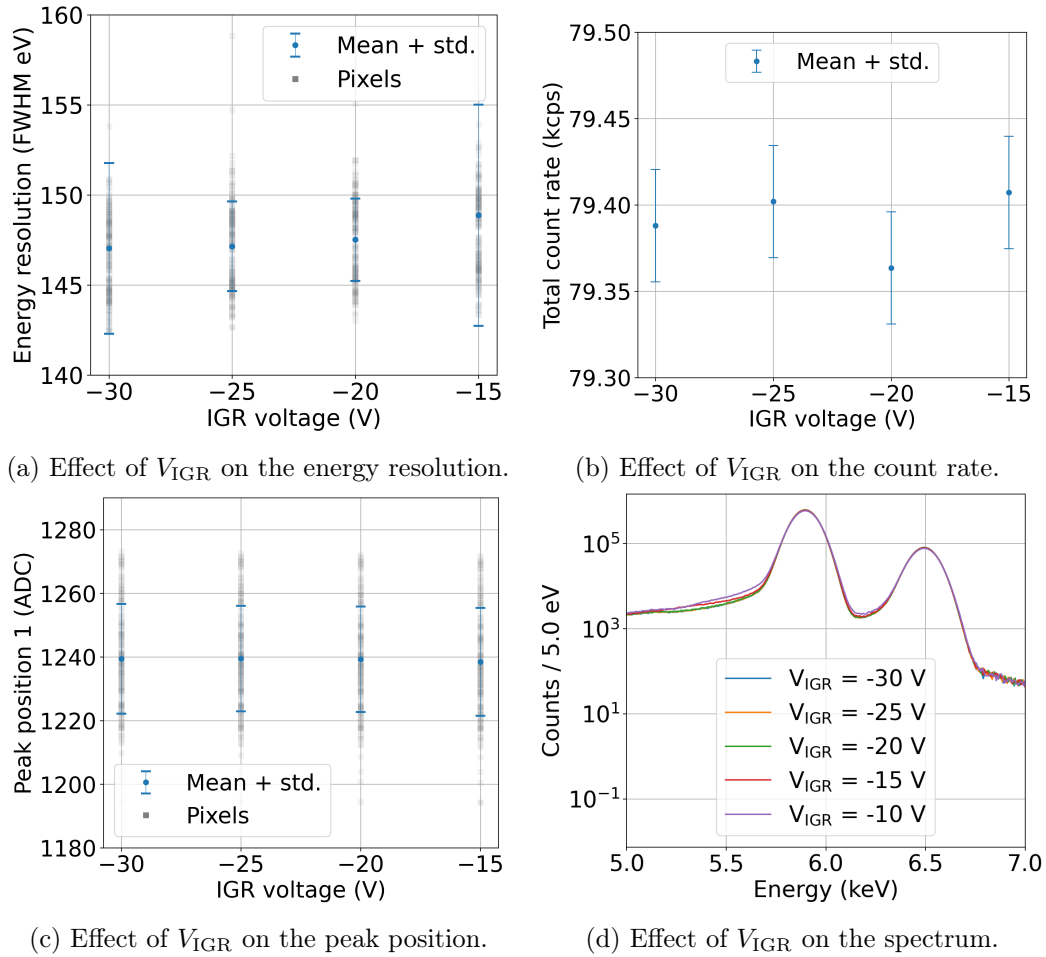
Figure B.10: Impact of V_{IGR} on the detector performance. V_{IGR} has no impact on (a) the energy resolution, (b) the total count rate and (c) the peak position of the Mn-K$_{\alpha}$ peak. (d) For too positive values of V_{IGR}, low-energy shoulders on the peaks appear in the spectrum. Adapted from [53].

Bibliography

[1] W. Pauli. »Letter to Tübinger Conference, December 4, 1930, translated in L.M. Brown«. In: *Phys. Today* 23 (1930).

[2] V. Barger, D. Marfatia and K. Whisnant. *The Physics of Neutrinos*. Princeton: Princeton University Press, 2012.

[3] C. L. Cowan et al. »Detection of the Free Neutrino: a Confirmation«. In: *Science* 124.3212 (1956), pp. 103–104. DOI: `10.1126/science.124.3212.103`. eprint: `https://www.science.org/doi/pdf/10.1126/science.124.3212.103`. URL: `https://www.science.org/doi/abs/10.1126/science.124.3212.103`.

[4] G. Danby et al. »Observation of High-Energy Neutrino Reactions and the Existence of Two Kinds of Neutrinos«. In: *Phys. Rev. Lett.* 9 (July 1962), pp. 36–44. DOI: `10.1103/PhysRevLett.9.36`. URL: `https://link.aps.org/doi/10.1103/PhysRevLett.9.36`.

[5] K. Kodama et al. »Observation of tau neutrino interactions«. In: *Physics Letters B* 504.3 (Apr. 2001), pp. 218–224. DOI: `10.1016/s0370-2693(01)00307-0`. URL: `https://doi.org/10.1016%2Fs0370-2693%2801%2900307-0`.

[6] M. Goldhaber, L. Grodzins and A. W. Sunyar. »Helicity of Neutrinos«. In: *Phys. Rev.* 109 (Feb. 1958), pp. 1015–1017. DOI: `10.1103/PhysRev.109.1015`. URL: `https://link.aps.org/doi/10.1103/PhysRev.109.1015`.

[7] S. N. Gninenko, D. S. Gorbunov and M. E. Shaposhnikov. »Search for GeV-scale sterile neutrinos responsible for active neutrino oscillations and baryon asymmetry of the Universe«. In: *arXiv e-prints* (Jan. 2013). arXiv: `1301.5516 [hep-ph]`.

[8] B. T. Cleveland et al. »Measurement of the Solar Electron Neutrino Flux with the Homestake Chlorine Detector«. In: *The Astrophysical Journal* 496.1 (Mar. 1998), p. 505. DOI: `10.1086/305343`. URL: `https://dx.doi.org/10.1086/305343`.

[9] Y. Fukuda et al. »Evidence for Oscillation of Atmospheric Neutrinos«. In: *Phys. Rev. Lett.* 81 (Aug. 1998), pp. 1562–1567. DOI: `10.1103/PhysRevLett.81.1562`. URL: `https://link.aps.org/doi/10.1103/PhysRevLett.81.1562`.

[10] N. Tolich. »Final results from SNO«. In: *Journal of Physics: Conference Series* 375 (July 2012). DOI: `10.1088/1742-6596/375/1/042049`.

[11] C. Giganti, S. Lavignac, and M. Zito. »Neutrino oscillations: the rise of the PMNS paradigm«. In: *Progress in Particle and Nuclear Physics* 98 (2017), pp. 1–54. DOI: 10.1016/j.ppnp.2017.10.001.

[12] R. Adhikari et al. »A White Paper on keV sterile neutrino Dark Matter«. In: *Journal of Cosmology and Astroparticle Physics* 2017.01 (Jan. 2017), pp. 025–025. DOI: 10.1088/1475-7516/2017/01/025. URL: https://doi.org/10.1088%2F1475-7516%2F2017%2F01%2F025.

[13] A. Loureiro et al. »Upper Bound of Neutrino Masses from Combined Cosmological Observations and Particle Physics Experiments«. In: *Phys. Rev. Lett.* 123 (Aug. 2019), p. 081301. DOI: 10.1103/PhysRevLett.123.081301. URL: https://link.aps.org/doi/10.1103/PhysRevLett.123.081301.

[14] V. Cirigliano et al. *Neutrinoless Double-Beta Decay: A Roadmap for Matching Theory to Experiment.* 2022. DOI: 10.48550/ARXIV.2203.12169. URL: https://arxiv.org/abs/2203.12169.

[15] M. Agostini et al. »Final Results of GERDA on the Search for Neutrinoless Double-$\beta\beta$ Decay«. In: *Physical Review Letters* 125.25 (Dec. 2020). DOI: 10.1103/physrevlett.125.252502. URL: https://doi.org/10.1103%2Fphysrevlett.125.252502.

[16] LEGEND Collaboration et al. *LEGEND-1000 Preconceptual Design Report.* 2021. DOI: 10.48550/ARXIV.2107.11462. URL: https://arxiv.org/abs/2107.11462.

[17] U. Wichoski. »Status of the EXO experiment«. In: *Proceedings of the 23rd Lake Louise Winter Institute: Fundamental Interactions, LLWI 2008* (Sept. 2009). DOI: 10.1142/9789814280945_0058.

[18] A. Giachero et al. *New results from the CUORE experiment.* 2020. DOI: 10.48550/ARXIV.2011.09295. URL: https://arxiv.org/abs/2011.09295.

[19] M. Aker et al. »Direct neutrino-mass measurement with sub-electronvolt sensitivity«. In: *Nature Phys.* 18.2 (2022), pp. 160–166. DOI: 10.1038/s41567-021-01463-1. arXiv: 2105.08533 [hep-ex].

[20] J. Angrik et al. (KATRIN Collaboration). »KATRIN Design Report 2004«. In: (2004). DOI: 10.5445/IR/270060419.

[21] Project 8 Collaboration et al. *The Project 8 Neutrino Mass Experiment.* 2022. DOI: 10.48550/ARXIV.2203.07349. URL: https://arxiv.org/abs/2203.07349.

[22] A. Boyarsky et al. »Sterile neutrino Dark Matter«. In: *Progress in Particle and Nuclear Physics* 104 (2019), pp. 1–45. ISSN: 0146-6410. DOI: https://doi.org/10.1016/j.ppnp.2018.07.004. URL: https://www.sciencedirect.com/science/article/pii/S0146641018300711.

116

[23] J. N. Abdurashitov et al. »Measurement of the response of a gallium metal solar neutrino experiment to neutrinos from a 51Cr source«. In: *Physical Review C* 59.4 (Apr. 1999), pp. 2246–2263. DOI: `10.1103/physrevc.59.2246`. URL: `https://doi.org/10.1103%2Fphysrevc.59.2246`.

[24] F. Kaether et al. »Reanalysis of the Gallex solar neutrino flux and source experiments«. In: *Physics Letters B* 685.1 (Feb. 2010), pp. 47–54. DOI: `10.1016/j.physletb.2010.01.030`. URL: `https://doi.org/10.1016%2Fj.physletb.2010.01.030`.

[25] V. V. Barinov et al. »Search for electron-neutrino transitions to sterile states in the BEST experiment«. In: *Physical Review C* 105.6 (June 2022). DOI: `10.1103/physrevc.105.065502`. URL: `https://doi.org/10.1103%2Fphysrevc.105.065502`.

[26] Joachim Kopp et al. »Sterile neutrino oscillations: the global picture«. In: *Journal of High Energy Physics* 2013.5 (May 2013). DOI: `10.1007/jhep05(2013)050`. URL: `https://doi.org/10.1007%2Fjhep05%282013%29050`.

[27] A. Aguilar et al. »Evidence for neutrino oscillations from the observation of $\overline{\nu}_e$ appearance in a $\overline{\nu}_\mu$ beam«. In: *Phys. Rev. D* 64 (Nov. 2001), p. 112007. DOI: `10.1103/PhysRevD.64.112007`. URL: `https://link.aps.org/doi/10.1103/PhysRevD.64.112007`.

[28] Ch. Kraus et al. »Final results from phase II of the Mainz neutrino mass search in tritium β decay«. In: *Eur. Phys. J. C* 40 (2005), pp. 447–468. DOI: `10.1140/epjc/s2005-02139-7`. arXiv: `hep-ex/0412056`.

[29] V. N. Aseev et al. »Upper limit on the electron antineutrino mass from the Troitsk experiment«. In: *Phys. Rev. D* 84 (Dec. 2011), p. 112003. DOI: `10.1103/PhysRevD.84.112003`. URL: `https://link.aps.org/doi/10.1103/PhysRevD.84.112003`.

[30] T. Brunst. »First generation prototype detectors for the TRISTAN project«. PhD Thesis. Technical University of Munich, 2020. URL: `http://mediatum.ub.tum.de/?id=1540377`.

[31] P. Kruit and F. H. Read. »Magnetic field paralleliser for 2π electron-spectrometer and electron-image magnifier«. In: *Journal of Physics E: Scientific Instruments* 16.4 (Apr. 1983), p. 313. DOI: `10.1088/0022-3735/16/4/016`. URL: `https://dx.doi.org/10.1088/0022-3735/16/4/016`.

[32] N. Wandkowsky. »Study of background and transmission properties of the KATRIN spectrometers«. PhD thesis. 2013. DOI: `10.5445/IR/1000036631`.

[33] J.F. Amsbaugh et al. »Focal-plane detector system for the KATRIN experiment«. In: *Nuclear Instruments and Methods in Physics Research Section A: Accelerators, Spectrometers, Detectors and Associated Equipment* 778 (2015), pp. 40–60. ISSN: 0168-9002. DOI: `https : / / doi . org/ 10 . 1016/ j . nima . 2014 . 12 . 116`. URL: `https : / / www . sciencedirect . com/science/article/pii/S0168900215000236`.

[34] L. Schlüter. »Development of New Methods to Include Systematic Effects in the First Tritium Data Analysis and Sensitivity Studies of the KATRIN Experiment«. Master's Thesis. Technical University of Munich, 2019.

[35] S. Mertens et al. »A novel detector system for KATRIN to search for keV-scale sterile neutrinos«. In: *Journal of Physics G: Nuclear and Particle Physics* 46.6 (May 2019), p. 065203. DOI: `10.1088/1361-6471/ab12fe`. URL: `https://dx.doi.org/10.1088/1361-6471/ab12fe`.

[36] S. Mertens et al. »A novel detector system for KATRIN to search for keV-scale sterile neutrinos«. In: *Journal of Physics G: Nuclear and Particle Physics* 46.6 (May 2019), p. 065203. DOI: `10.1088/1361-6471/ab12fe`. URL: `https://dx.doi.org/10.1088/1361-6471/ab12fe`.

[37] M. Aker et al. *Search for keV-scale Sterile Neutrinos with first KATRIN Data.* 2022. DOI: `10 . 48550/ ARXIV . 2207 . 06337`. URL: `https : // arxiv . org/abs/2207.06337`.

[38] G. Lutz. *Semiconductor Radiation Detectors.* Springer Berlin, Heidelberg, 2007. ISBN: 9783540716785.

[39] F. Hartmann. *Evolution of Silicon Sensor Technology in Particle Physics.* Springer International Publishing AG, 2017. ISBN: 9783319877945.

[40] M. Lebert. »Characterization of the Detector Response to Electrons and Test of a New Entrance Window Technology of Silicon Drift Detectors for the TRISTAN Project«. Master's Thesis. Technical University of Munich, 2019.

[41] D. Siegmann. »Investigation of the Detector Response to Electrons of the TRISTAN Prototype Detectors«. Master's Thesis. Technical University of Munich, 2019.

[42] M. Mazziotta. »Electron–hole pair creation energy and Fano factor temperature dependence in silicon«. In: *Nuclear Instruments and Methods in Physics Research Section A-accelerators Spectrometers Detectors and Associated Equipment* 584 (Jan. 2008), pp. 436–439. DOI: `10.1016/j.nima.2007.10.043`.

[43] E. Gatti and P. Rehak. »Semiconductor drift chamber — An application of a novel charge transport scheme«. In: *Nuclear Instruments and Methods in Physics Research* 225.3 (1984), pp. 608–614. ISSN: 0167-5087. DOI: `https://doi.org/10.1016/0167-5087(84)90113-3`. URL: `https://www.sciencedirect.com/science/article/pii/0167508784901133`.

[44] Thermo Fisher Scientific - Materials & Structural Analysis. *An Introduction to Silicon Drift Detectors*. URL: `https://www.azom.com/article.aspx?ArticleID=11973`. (accessed: 16.02.2023).

[45] P. Trigilio et al. »ETTORE: a 12-Channel Front-End ASIC for SDDs with Integrated JFET«. In: *2018 IEEE Nuclear Science Symposium and Medical Imaging Conference Proceedings (NSS/MIC)*. 2018, pp. 1–4. DOI: `10.1109/NSSMIC.2018.8824675`.

[46] M. Gugiatti. »Development of a large-matrix SDD-based radiation detector for beta-decay spectroscopy in neutrino physics«. PhD Thesis. Politecnico di Milano, 2021.

[47] L. Rossi et al. *Pixel Detectors: From Fundamentals to Applications*. Springer-Verlag Berlin Heidelberg GmbH, 2006. ISBN: 978-3-540-28332-4.

[48] C. Bruch. »Investigation of the noise performance of silicon drift detectors for the TRISTAN project«. Bachelor Thesis. Technical University of Munich, 2020.

[49] E. Pinotti et al. »The pn-CCD on-chip electronics«. In: *Nuclear Instruments and Methods in Physics Research Section A: Accelerators, Spectrometers, Detectors and Associated Equipment* 326.1 (1993), pp. 85–91. ISSN: 0168-9002. DOI: `10.1016/0168-9002(93)90337-H`.

[50] R. Müller. *Halbleiter-Elektronik: Rauschen*. Halbleiter-Elektronik. Springer-Verlag Berlin Heidelberg GmbH, 1979. ISBN: 9783642615016.

[51] H. Spieler. *Semiconductor Detector Systems*. Semiconductor Science and Technology. Clarendon Press Oxford, 2005. ISBN: 9780198527848.

[52] J. Carvill. »3 - Thermodynamics and heat transfer«. In: *Mechanical Engineer's Data Handbook*. Ed. by J. Carvill. Oxford: Butterworth-Heinemann, 1993, pp. 102–145. ISBN: 978-0-08-051135-1. DOI: `https://doi.org/10.1016/B978-0-08-051135-1.50008-X`. URL: `https://www.sciencedirect.com/science/article/pii/B978008051135150008X`.

[53] D. Siegmann. »Characterization of the first TRISTAN 166-pixel detector module«. In preparation. PhD Thesis. Technical University of Munich, 2023.

[54] P. King. »Development of a multi-channel analog pulse processing and data acquisition system for the TRISTAN detector«. PhD Thesis. Politecnico di Milano, 2019.

[55] M. Descher. »High rate systematic effects for keV sterile neutrino searches at KATRIN«. Master's Thesis. Karlsruhe Institute of Technology, 2019.

[56] J. Goullon. »Installation and commissioning of the monitor spectrometer of KATRIN«. Diplom Thesis. Karlsruhe Institute of Technology, 2010.

[57] K. Altenmüller et al. »Muon-induced background in the KATRIN main spectrometer«. In: *Astroparticle Physics* 108 (2019), pp. 40–49. ISSN: 0927-6505. DOI: `https://doi.org/10.1016/j.astropartphys.2019.01.003`. URL: `https://www.sciencedirect.com/science/article/pii/S0927650518302597`.

[58] Laboratoire National Henri Becquerel. *Table de Radionucléides*. 2006. URL: `http://www.nucleide.org/DDEP_WG/Nuclides/Fe-55_tables.pdf`. (accessed: 08.09.2020).

[59] D. Vénos et al. »Properties of 83mKr conversion electrons and their use in the KATRIN experiment«. In: *Journal of Instrumentation* 13.02 (Feb. 2018), T02012. DOI: `10.1088/1748-0221/13/02/T02012`. URL: `https://dx.doi.org/10.1088/1748-0221/13/02/T02012`.

[60] M. Slezák. »Monitoring of the energy scale in the KATRIN neutrino experiment«. PhD Thesis. Charles University in Prague, 2015.

[61] E.A. McCutchan. »Nuclear Data Sheets for A = 83«. In: *Nuclear Data Sheets* 125 (2015), pp. 201–394. ISSN: 0090-3752. DOI: `https://doi.org/10.1016/j.nds.2015.02.002`. URL: `https://www.sciencedirect.com/science/article/pii/S0090375215000034`.

[62] H. Arlinghaus. »Investigation of the muon-induced secondary electron background in the KATRIN Experiment«. Diplom Thesis. Westfälische Wilhelms-Universität Münster, 2009.

[63] C. Forstner. »Characterization of a TRISTAN Silicon Drift Detector Array with a Laser System«. Master's Thesis. Technical University of Munich, 2023.

[64] Jeffrey B. Kortright. *X-RAY EMISSION ENERGIES*. 2000. URL: `https://xdb.lbl.gov/Section1/Table_1-2.pdf`. (accessed: 12.12.2022).

[65] D. Spreng. »Energy Calibration of the TRISTAN Silicon Drift Detectors«. Bachelor Thesis. Technical University of Munich, 2020.

Acknowledgements

I would like to thank everyone who supported me during my master's thesis, especially:

- **Prof. Dr. Susanne Mertens:** Thank you for giving me the opportunity to do my master's thesis in your group and for your great support during my work.

- **Daniel Siegmann:** Thank you for your words of encouragement when I needed them, for countless drives with questionable music but very enjoyable company, for your trust in me and my abilities, for sharing your knowledge about the detectors with me and for the nice working atmosphere.

- **Frank Edzards:** Thank you for your superior proofreading skills, for your never ending knowledge about everything neutrino related and for your general support during my work. You definitely made me a better writer.

- **Danilo Mießner:** Thank you for your patience to answer all my questions concerning the assembly of the detector.

- **Dominic Hinz:** Thank you for your support during my stays in Karlsruhe and for answering all my questions concerning the MoS.

- **Korbinian Urban:** Thank you for patiently answering my questions about noise and for all the great suggestions, that helped me a lot during my analysis.

- **Daniela Spreng:** Thank you for your moral support and for always having time for me when I got stuck.

- **KATRISTAN work group:** Thank you all for the kind conversations during coffee break, nice events and a pleasant work environment.

- **The Schnatterbüro:** Thank you for all physics related and unrelated conversations and for all the fun I had talking and laughing with you.

- **Christian Hiechinger:** Thank you for useful tips and tricks concerning my code, for your superior WLAN connection, which made the download of data so much faster, and for keeping me sane.